Diffusion of deuterium in crystalline β-Ga_2O_3

Vilde Mari Reinertsen

Thesis submitted for the degree of
Master of science in Materials Science and Nanotechnology
60 credits

Department of Chemistry
Faculty of mathematics and natural sciences

UNIVERSITY OF OSLO

Spring 2019

Diffusion of deuterium in crystalline β-Ga_2O_3

Vilde Mari Reinertsen

Diffusion of deuterium in crystalline β-Ga_2O_3

http://www.duo.uio.no/

Printed: Reprosentralen, University of Oslo

Abstract

The objective of this thesis is to investigate the diffusion of hydrogen in the β polymorph of gallium oxide (β-Ga_2O_3). β-Ga_2O_3 is a wide band gap semiconductor that has received considerable attention the last few years due to its high breakdown field of 8 MV/cm and a band gap of $\sim$4.8 eV, and it is therefore considered as a promising material for power electronics. Hydrogen is an important impurity in β-Ga_2O_3, partly because of its abundance. Theoretical calculations shows that it acts as a shallow donor on both interstitial and substitutional sites, and it can also passivate deep acceptors. Hence, knowledge about hydrogen and its diffusion behaviour is scientifically important for material and device development. The structure of β-Ga_2O_3 has low symmetry, and many of its properties are anisotropic. Accordingly, the study of diffusion of hydrogen was performed in two different crystal orientations, i.e. (-201) oriented and (010) oriented β-Ga_2O_3.

This thesis investigates hydrogen diffusion in β-Ga_2O_3 by sequential annealing and secondary ion mass spectroscopy (SIMS) depth profiling. As a substitute for hydrogen, deuterium was used to improve the detection limit in SIMS. Deuterium was found to diffuse at a lower temperature in the (010) orientation, i.e. below 300 °C, than in the (-201) orientation, where no diffusion was observed until heat treatment at 500 °C. Furthermore, a trap limited diffusion model (TLD) was found to describe the experimental diffusion profiles well. However, the activation energies for the diffusivities and dissociation rates extracted from the simulations, indicated that the diffusion is not only governed by the interstitial migration of deuterium and the dissociation from the traps. An additional thermally activated process is proposed to be connected to that the implantation peak is not acting as a semi-infinite source for deuterium as assumed in the model. Density functional theory (DFT) calculations were performed and are supporting the anisotropic diffusion observed experimentally. The migration energy in the (010) orientation, i.e. E_m = 0.18-0.40 (PBEsol-HSE) eV respectively, was substantially lower than, in a proposed migration path for diffusion, in the (-201) orientation where E_m = 1.72 (PBEsol) eV.

Fourier transform-infrared spectroscopy (FT-IR) measurements were performed to investigate the complex containing the trap and deuterium. The results showed that a shifted gallium vacancy in a complex with two deuterium ($V_{Ga}^{O(III)2}H_2$) was present in the samples. Additionally, the results showed that [$V_{Ga}^{O(III)2}H_2$] decreased substantially at heat treatments above 400 °C for samples of both orientations, i.e. (010) and (-201). From the FT-IR results, new unidentified peaks in the O-^{2}H/O-H region was observed at higher temperatures. These may explain the reduction in the $V_{Ga}^{O(III)2}H_2$ peak during heat treatments and shed light on the influence of the implantation peak on deuterium diffusion in β-Ga_2O_3. In conclusion, we have found that deuterium diffuses interstitially in β-Ga_2O_3, but the diffusion is limited by the creation of a complex with a point defect. The diffusion is anisotropic and is hence substantially faster in the (010) orientation than in the (-201) orientation. Even though the simulated diffusion profiles gave a good fit with the experimental profiles, quantitative data has been difficult to extract, especially in the (010) orientation. The combined result from DFT, FT-IR, SIMS and diffusion modelling imply that the point defect acting as a trap for deuterium is an intrinsic defect, and according to our DFT calculations and FT-IR results, the gallium vacancy is a strong candidate for trapping of ^{2}H.

Acknowledgements

First of all, I want to thank God for creating this wonderful world and for giving me the opportunity and abilities to investigate it using physics. Secondly, I want to thank my husband, Lars Kristian. Thank you for all your patience and for all the comfort and encouragement you have given me throughout this process. I also want to thank my two main supervisors assoc. prof. Lasse Vines and Dr. Klaus Magnus Håland Johansen for sharing your deep knowledge with me and revising this thesis. Thank you, Lasse, especially for your enthusiasm for the topic of this thesis. It has really motivated me along the way. And thank you Klaus Magnus for the discussions we had when I reached problems along the way and the insight they gave me. I want to thank my third supervisor Dr. Thomas Neset Sky for teaching me SIMS and for being so patient when I made mistakes in the beginning. Thank you Sigbjørn Grini for taking over for Thomas when he left, for asking me how it is going and for making sure that I performed the SIMS measurements.

Additionally, I have to thank Ymir K. Frodason and Marianne E. Bathen for answering all my questions about DFT and helping me perform DFT calculations. Thank you, Dr. Phillip M. Weiser, for all the "how are you?"s, the FT-IR measurements and expertise and especially for your enthusiasm for hydrogen in β-Ga_2O_3. Thank you, Maya, for your smiles and our talks. Thank you, Kristine, for the proofing you did. Thank you, Torbjørn, Fredrik and all the other master students at LENS, for creating a nice environment to study and write. Thank you to everyone at LENS, for making me feel welcome and included in the research group. In the end, I wish to thank Silje and Kjetil for the lunches we have shared that reassured me so much. And finally a big thank you to my parents, for being so proud of me, and to Frida for being a wonderful little sister.

Contents

Chapter 1

Introduction

We need more energy from renewable energy sources. The earth is going through climate changes because of the amount of climate gases we are emitting to the atmosphere. We also have a continuous rise in population. The demand for energy will escalate with the economic growth in undeveloped countries where the population growth is largest. This need for energy can be met in different ways. We can find new energy sources, but we can also work with improving energy efficiency [1]. One way to do this is to enhance already existing electrical technologies and devices in order to lose less energy. One relevant field in this respect is power electronics (PE), which comprises the application of solid-state electronics to distribute and convert electric energy. The most common material in PE now is Si, but a transition to a wide band gap material (WBG) will decrease energy loss in operation. This is due to the increased intrinsic breakdown voltage of WBGs that consequently increases the possible doping concentration, while keeping a high enough breakdown voltage. The increased doping will reduce the depletion width, and hence, smaller device dimensions are possible. Furthermore, smaller device dimensions cause less series resistance and accordingly less energy loss.

The dominating WBGs in PE until now has been SiC and GaN, but gallium oxide (Ga_2O_3) has shown itself as a promising novel material for PE application. Because of the possibility of growing substrates from melt, β-Ga_2O_3 (the most stable polymorph) seems to have the potential to become a cheap and fast material to grow compared to its competition in both economical cost and energy cost [2]. Furthermore, the potential of a material in PE can be measured by different figures of merit, and gallium oxide has a Baliga's figure of merit (BFOM) four times higher than GaN and ten times higher than SiC. The reason is its high band gap at $\sim$4.8 eV and its high critical field at 8 MV/cm [3]. The wide band gap is essential in power electronics making the devices able to operate at high temperatures.

Several semiconducting oxides have been under research for years now, including ZnO and Cu_2O. It has been discovered that it is difficult to make both n-type and p-type semiconductors of the same oxide. Cu_2O tends to prefer p-type conductivity and ZnO prefers n-type. β-Ga_2O_3 is in the latter category. There are three main reasons for the difficulties of making p-type β-Ga_2O_3. The valence band structure in gallium oxide is flat, the holes have a large effective mass, and hence low mobility, and tend to make localized polarons instead of being free holes [4]. The valence band is made of mainly oxygen orbitals that have a low energy, and consequently it is difficult to find shallow acceptors. Finally, the common impurities in β-Ga_2O_3, e.g. hydrogen and silicon, are donors

that passivate acceptors. Another disadvantage of β-Ga_2O_3 is its relatively low thermal conductivity, which complicates device design and fabrication [5].

Hydrogen is interesting because theoretical calculations shows that it is a shallow donor at both interstitial and substitutional sites [6]. Hydrogen is a common impurity in many materials, including β-Ga_2O_3. Both of these facts indicate that hydrogen can partially explain the n-type background doping as in ZnO [7]. Hydrogen easily forms complexes with other point defects, because of its small size and high chemical reactivity. The complex between vacancies and hydrogen in oxides is especially stable because the hydrogen is stable at the inner surface of the vacancy[8].

Since hydrogen is abundant in the material, knowledge about its behaviour in β-Ga_2O_3 is essential for production of β-Ga_2O_3 devices. Because all device production includes several annealing steps, the diffusion of point defects in the material is highly relevant. That includes the diffusion of hydrogen, which is the topic of this work. As a substitute for hydrogen, deuterium was used in the experiments in this work because of the high detection limit of hydrogen in secondary ion mass spectroscopy (SIMS). This thesis investigates deuterium diffusion in β-Ga_2O_3 by sequential annealing and SIMS depth profiling. We have also used Fourier transform-infrared spectroscopy (FT-IR) to investigate hydrogen in a complex with a gallium vacancy. In addition, density functional theory (DFT) was used to investigate the hydrogen-gallium vacancy complex and also the migration path of the interstitial hydrogen. The combination of these different approaches makes it possible to find out more about the diffusion mechanism of hydrogen and how it behaves in β-Ga_2O_3.

Chapter 2

Theory

This chapter will introduce relevant topics and background information to understand both the techniques and the results of this work. The chapter begins with an introduction to semiconductors and important concepts in semiconductor physics. From there, point defects in crystals are discussed. The main focus of this work, diffusion, is then thoroughly explained and different mechanisms and models are accounted for. At last, the structure and background information of β-Ga_2O_3 is presented.

2.1 Introduction to semiconductors

All solid state materials can be categorized into groups from how ordered they are. Solid-state materials that have no order are categorized as amorph while, on the other hand, materials with a clear repeating order are called single-crystals or (mono)crystalline materials. In between these two are materials which are polycrystalline where there are smaller single-crystal grains packed together in different orientations. Semiconductors used in devices are most often in the crystalline category, as is the material of this work, crystalline β-Ga_2O_3, which will be presented later in the chapter.

2.1.1 Electronic structure

When a crystal is formed, the atomic orbitals or wavefunctions of the atoms' electrons interact with each other and create new orbitals. The nature of atoms and electrons can be described and understood by using the Schrödinger Equation:

$$\hat{H}\Psi = E\Psi, \tag{2.1}$$

where $\hat{H} = \hat{T} + \hat{U}$, $\hat{T}$ is the kinetic energy operator and $\hat{U}$ is the potential energy operator. The potential, V, and the boundary conditions will decide what solutions the Schrödinger Equation (SE) have. Solving the SE with different potentials and boundary conditions are an approach to model how atoms and their electrons are affected by their surroundings. A solution of the SE will often be represented by a linear combination of the equation's eigenfunctions, $\psi_{\mathbf{k}}$, where $\mathbf{k}$ is the wavenumber of the eigenfunction. When the electron is a free electron, $\mathbf{k}$ can be any number, but the inclusion of a potential and boundary conditions will quantify the wavenumbers and only discrete values of $\mathbf{k}$ will be allowed. The solution for a free and isolated electron, with no external potential is:

$$\psi_{\mathbf{k}}(\mathbf{r}) = A \exp(i\mathbf{k}\mathbf{r}), \tag{2.2}$$

where A is a normalization constant, $\mathbf{k}$ is the wavenumber from $\lambda = \frac{2\pi}{|\mathbf{k}|}$ and $\mathbf{r}$ is the position vector. Later, when discussing density functional theory, this simple picture of the eigenfunction is modified to suit an electron in a crystal.

Electrons are fermions and their wavefunction is antisymmetric. The consequence of this, is that only two electrons with opposite spin can occupy the same energy state. Electrons will therefore fill the states in the energy bands of the crystal, beginning with the ones with lowest energy.

2.1.2 Energy Bands

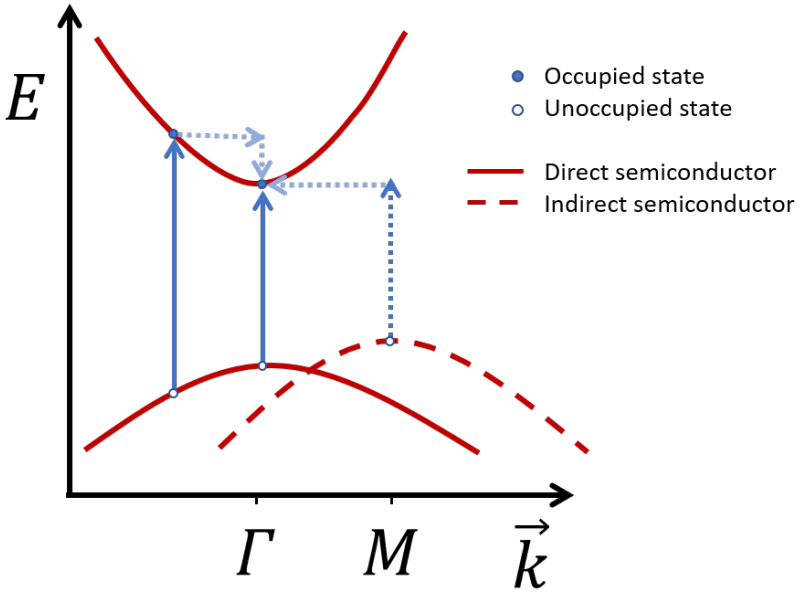

Figure 2.1.1: A simplified band structure of a semiconductor. The energy bands are plotted as lines in this plot of energy versus **k**-points. The lines symbolize the states in this particular structure which have a specific energy and consequently a specific **k**. An electron which is excited from the valence band to the conduction band is shown by the blue arrows. The dotted arrows show how an electron sometimes have to change both its energy and its momentum, when it changes state. The stippled red line shows how the band structure of an indirect semiconductor might look. In that case, the states with minimum energy in the conduction band do not have the same **k** as the maximum in the valence band.

Interacting states make up what is called an energy band. In an energy band, charge carriers are free to move if there are unoccupied states within the band. To move from one band to another, a change in energy and momentum ($\hbar\mathbf{k}$) may be required. This is illustrated in Figure 2.1.1, where the bands are plotted as lines in the energy versus **k** plot. The energy bands in the band structure of a crystal define the states an electron can occupy. The energy bands are determined by which atoms form the crystal, more exactly their orbitals and valence. Between energy bands there can be a range of energies where no states are allowed, and hence, no electron can be found. These states are therefore not solutions of the SE for the specific conditions.

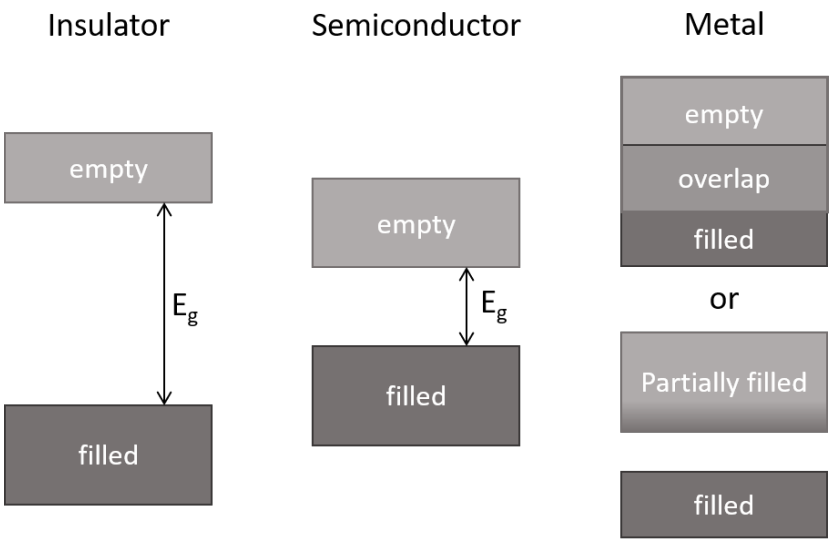

Figure 2.1.2: Illustration of band structures and their occupancy at 0 K. Revised from Ref. (Reference) [9]

Semiconductors differ from metals and isolators because of a difference in band structure and in the occupancy of the energy bands. Figure 2.1.2 shows the band structure of the different types of materials at 0 K. In semiconductors and isolators, the uppermost filled energy band, the valence band, is totally filled with electrons and there is a band gap separating the electrons in the valence band with the unoccupied states in the conduction band. As the figure shows, the size of this band gap, E_g, usually decides if the material is classified as an isolator or a semiconductor. Other material properties can also play a role, e.g. the doping ability of the material. β-Ga_2O_3 is an example of this. It is classified as a semiconductor even with its large band gap of $\sim$4.8 eV. On the other hand, in metals, the valence band is only partially filled, or, as Figure 2.1.2 shows, the valence band overlaps with the conduction band and the electrons are free to move.

In the case of semiconductors, charge carriers may be excited from the valence band to the conduction band, and the minimum amount of energy required is determined by the band gap. Figure 2.1.1 shows how an electron is excited from the valence band to the conduction band in a direct semiconductor and an indirect semiconductor. When the electrons are in the conduction band there are plenty of unoccupied states and the electrons are free to move and thereby conduct current.

An important aspect in semiconductors are the unoccupied states left behind in the valence band from the excited electrons. These unoccupied states make it possible for electrons in the valence band to move as well. The nature of this motion is different than in the conduction band and is simplified to the concept of a quasi-particle called a hole which acts with respect to electric and magnetic fields as a particle with the opposite charge of the electron, i.e. a positive charge [9, Ch. 3].

2.1.3 Doping

The conductivity of a semiconductor can be modified by doping. This means that one adds another element which either adds more electrons (donor) or more holes (acceptor). The donors induce an energy level within the band gap of the semiconductor, and an ideal donor will have an energy level just below the minimum energy in the conduction band, E_C, because then the extra electrons are

easily donated to the conduction band. The acceptor energy level of an ideal acceptor is situated just above the valence band maximum, E_V, because then only a small amount of energy is required to excite the electrons from the valence band into the acceptor state, and thus, leaving behind holes. A semiconductor with more donors and consequently more electrons is called n-type and the opposite is called p-type.

The doping of a semiconductor creates new states in the crystal, often in the band gap. Other point defects can also create states within the band gap. These energy levels exist due to the exception from the periodicity of the crystal. If the concentration of this defect is high enough, the point defects combined create an energy band in the band gap. This happens because the defects are close enough to interact. This issue of defects creating an energy band instead of an energy level arises in the density functional theory calculations.

A system which is in thermal equilibrium will be charge neutral. The charge neutrality of a semiconductor is given by:

$$N_a + n = N_d + p, \tag{2.3}$$

where N_a is the concentration of acceptors, which are negatively charged after accepting an electron. N_d is the concentration of donors, which are positively charged after donating an electron. n is the concentration of electrons and p is the concentration of holes.

2.1.4 The Fermi Level

Electrons obey Fermi-Dirac statistics with the distribution function:

$$f(E) = \frac{1}{1 + \exp\left(\frac{E-\epsilon_F}{k_B T}\right)}, \tag{2.4}$$

for finite temperatures. In Equation 2.4, $f(E)$ is the probability of an electron occupying a state with energy, E. The Fermi level, ϵ_F, is the energy at the inflection point of the distribution function, $f(E)$.

The distribution function is symmetrical around the Fermi level. This is showed in Figure 2.1.3 which includes how doping affects the distribution of charge carriers in the conduction and valence band. The probability of electrons occupying states in the conduction band is increasing for an n-type semiconductor. Hence, there are more electrons in the conduction band than there are holes in the valence band. Analogously, the opposite change in distribution is occuring in a p-type semiconductor. The Fermi level is hence showing what the dominant charge carrier is. It can also be used to calculate the concentration of electrons or holes that are present in a semiconductor. The concentration of electrons can be found by multiplying $f(E)$ with the density of states in the conduction band. Similarly, the concentration of holes are calculated by multiplying $1 - f(E)$ with the density of states in the valence band. The concentration is described by:

$$n = 2\left(\frac{m_e k_B T}{2\pi\hbar}\right)^{3/2} \exp\left(-\frac{E_C - \epsilon_F}{k_B T}\right) \tag{2.5}$$

and

$$p = 2\left(\frac{m_p k_B T}{2\pi\hbar}\right)^{3/2} \exp\left(\frac{E_V - \epsilon_F}{k_B T}\right) \tag{2.6}$$

Here m_e is the effective mass of the electron, m_p is the effective mass of the hole, k_B is the Boltzmann constant, T is the temperature in Kelvin, $\hbar$ is the reduced Planck constant and ϵ_F is the Fermi level. The Fermi level also reveals the occupancy of a state in the band gap, where states below the Fermi level is likely to be occupied by an electron, while states above the Fermi level are not. This is particularly important when considering the charge state of a defect.

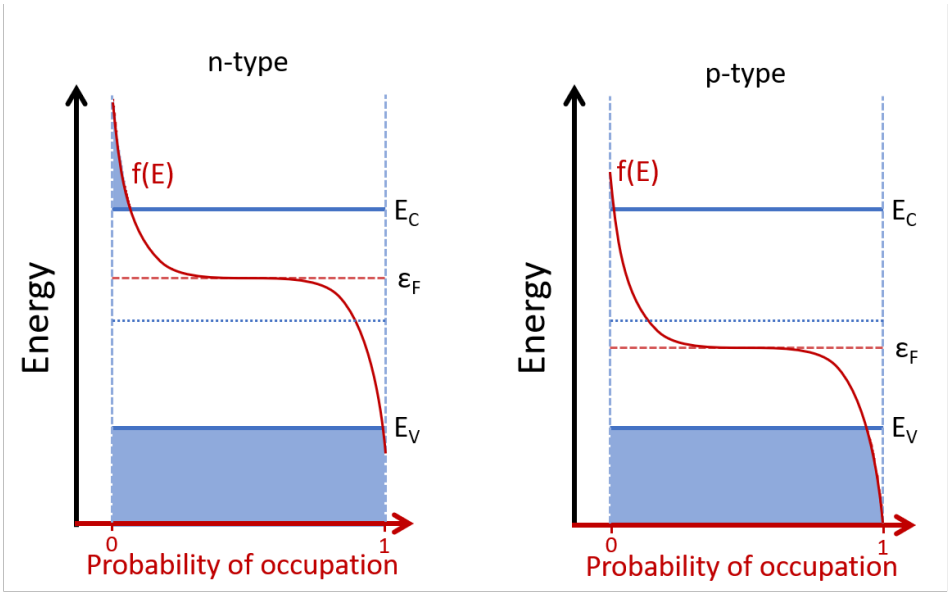

Figure 2.1.3: An illustrative energy diagram of n-type and p-type semiconductors. This is a simplified picture of the band structure, only showing the maximum of the valence band, E_V, and the minimum of the conduction band, E_C. ϵ_F is the Fermi level of the semiconductor. The distribution function is added to illustrate how the probability of electrons occupying states in the conduction band is increasing for an n-type semiconductor and likewise for holes in the valence band for a p-type semiconductor. Revised from Ref. [9].

2.2 Defects

Deviations from the order of crystalline crystals are called defects. The defects in a crystal are categorized by their dimensionality. There are zero, one, two and three dimensional defects exemplified with a vacancy, a dislocation, a grain boundary and a precipitate respectively. In this thesis the higher dimensional defects will not be discussed. The focus is on the zero dimensional ones, that are called point defects. The topic in this thesis is mainly concentrated around the point defect deuterium in β-Ga_2O_3.

2.2.1 Point defects

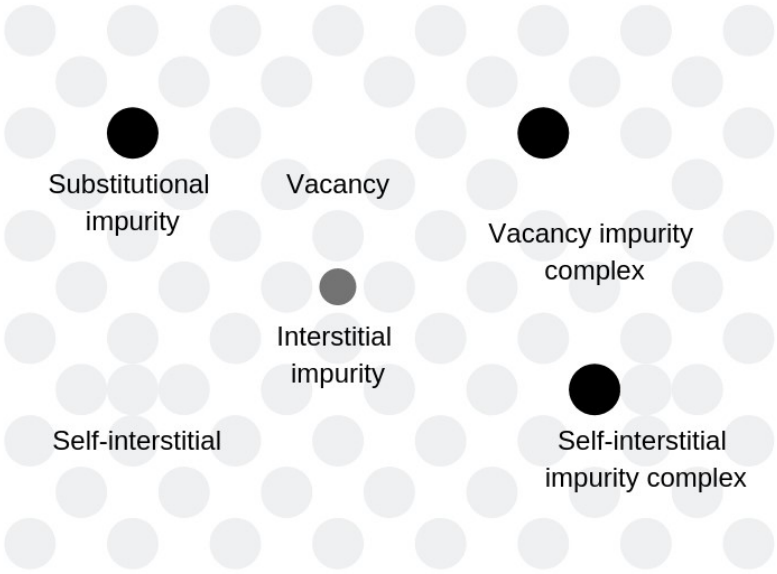

Figure 2.2.1: The different point defects and two simple complexes between them.

Figure 2.2.1 displays different types of point defects. Intrinsic defects, also known as native defects, include the self-interstitial, the vacancy and combinations of these such as a divacancy and an interstitial-vacancy pair. Extrinsic defects involve foreign atoms in the structure and can arise from both intentional and unintentional incorporation in the material. Substitutional impurities replace one of the atoms in the structure and interstitial impurities sit in an interstitial site. Combinations of intrinsic and extrinsic defects, making a defect complex, also occur. All of these defects are not strictly zero dimensional, but are often counted as point defects, since they to a large extent can be treated using the same formalism. There are situations where this assumption no longer holds, for example if the defect is charged and the effect of the defect is extended over several neighbouring atoms.

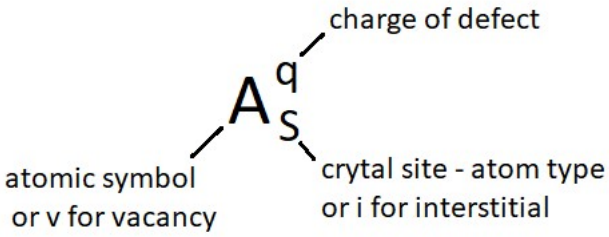

Figure 2.2.2: The defect notation used in this thesis. A represents the atomic symbol of an atom or V for the vacancy, S represents the crystal site, which in this work would be either Ga for the gallium site, O for the oxygen site or i for an interstitial site and, at last, q represents the charge of the defect.

The extrinsic point defects can be dopant atoms, as mentioned above, which either donate or accept an electron and become a charged defect. Other point defects can also become charged, and this is an important feature in semiconductors, since they may affect the effective conductivity of the material. The notation for point defects in this work is shown in Figure 2.2.2 where A represents the atomic symbol of an atom or V for the vacancy, S represents the crystal site, which in this work would be either Ga for the gallium site, O for the oxygen site or i for an interstitial site and, at last, q represents the charge of the defect.

There will always be intrinsic defects in a system at any finite temperature because of the increase in entropy when a defect is introduced. The entropy is a part of Gibbs free energy. The change in Gibbs free energy at constant volume is a change in the Helmholtz free energy and given by

$$\Delta G = \Delta F = \Delta H - T\Delta S. \tag{2.7}$$

Equation 2.7 shows that an increase of the entropy, S, will lower Gibbs free energy, G, and an increase of enthalpy, H, will raise G. When a defect is inserted the entropy increases because of the increase of possible ways to arrange the atoms, hence the disorder increases. However, the defect introduced will increase the enthalpy of the system for every defect, since the defect leaves the surrounding atoms in the structure in a non-optimized state. This balance results in the presence of intrinsic defects at finite temperatures when the system is in thermal equilibrium. The concentration of a defect can be shown to be:

$$\frac{N_j}{N} = [j] = \exp\frac{\Delta S_{\text{vibr}}}{k}\exp\frac{-\Delta H}{kT}. \tag{2.8}$$

N_j is the number of defects, N is the number of sites, $[j]$ is then the concentration of the specific defect, ΔS_{vibr} is the change in vibrational entropy, ΔH is the change in enthalpy, often referred to as the formation energy, and k is the Boltzmann constant. Equation 2.8 can be found using combinatorics to calculate the configurational part of the entropy,

$$\Delta S_{\text{total}} = N_j \Delta S_{\text{vibrational}} + \Delta S_{\text{configurational}}. \tag{2.9}$$

The entropy in Equation 2.8 is therefore only the vibrational part.

2.2.2 Defect reactions

The rest of this section is based Ref.s (References) [10, 11]. As mentioned earlier, point defects can interact with each other and create complexes. This can be described by defect reactions. An example of this is the reaction between an interstitial hydrogen and a metal vacancy in a metal oxide, MO:

$$V_M^{2-} + H_i^{+} \leftrightharpoons (V_M H)^{-}, \tag{2.10}$$

where M represents the metal atom in the oxide MO. Reactions involving defects can also describe formation or annihilation of defects. Defect reactions act as chemical reactions and two common defect reactions in oxides are the formation of two different defect pairs, the Frenkel pair:

$$V_M^{2-} + M_i^{2+} \leftrightharpoons 0 \text{ or } V_O^{2+} + O_i^{2-} \leftrightharpoons 0 \tag{2.11}$$

and the Schottky pair:

$$V_M^{2-} + V_O^{2+} \leftrightharpoons 0, \tag{2.12}$$

These reactions represent thermal formation and recombination of intrinsic defects. The reaction rate, which determines the equilibrium concentration of the products and the reactants, is determined by the equilibrium constant:

$$K = \frac{[A]^a[B]^b}{[C]^c[D]^d} = \exp\left(\frac{-\Delta G^\circ}{kT}\right) \qquad \text{for the reaction} \quad cC + dD \leftrightharpoons aA + bB, \tag{2.13}$$

which gives a connection between the concentration of the different defects and change in Gibbs free energy.

2.2.3 Equilibrium and concentration of defects

Equilibrium is established when the change in Gibbs free energy, ΔG is zero, that is the minimum Gibbs free energy. How fast the reaction reaches equilibrium, is dependent on the diluteness and the mobility of the reacting species. For example, the metal vacancy and the interstitial hydrogen has to collide to be able to react and create a complex. The assumption of local equilibrium is sometimes used in diffusion studies. It can be used if the reaction rate is greater than the time of diffusion, the movement of the species. Then the defect reactions will be assumed to be in equilibrium in certain places in the solid, even though the whole sample is not in equilibrium.

The concentration of a defect is affected by the current conditions. As an example, the concentration of metal vacancies in a material which is dominated by Schottky pairs (see Equation 2.12) will be showed. By combining Equation 2.5 and Equation 2.7, the concentration of metal vacancies is given by:

$$[V_M][V_O] = K \implies [V_M] = K^{1/2} = \exp\left(\frac{-\Delta G}{2kT}\right) = \exp\left(\frac{\Delta S}{2k}\right)\exp\left(\frac{-\Delta H}{2kT}\right) \tag{2.14}$$

if $[V_M^{2-}] = [V_O^{2+}]$, which is correct if the two defects are compensating each other and other charged species can be neglected. The ΔH is the activation enthalpy of the reaction which is the combined formation energy of the metal vacancy and the oxygen vacancy. The concentration of the metal vacancy is hence dependent on the dominating defects in the material. Sometimes it is challenging to reveal the dominating reaction in experiments or processes. With density functional theory, the formation energy of a single defect can be calculated unrelated to the reaction. These formation energies can be used to find the dominating reactions under certain conditions.

The relation between the different charged species is defined through a charge neutrality condition, where the sum of the concentration of all charged particles is zero,

$$\sum_{j=1}^{M} q_j c_j + p - n = 0, \tag{2.15}$$

and likewise that the concentration of the negative charges equals the positive charges. In this case it is

$$2[V_M^{2-}] + N_a + n = 2[V_O^{2+}] + N_d + p. \tag{2.16}$$

Equation 2.16 shows, in contrast to the simplified picture from Equation 2.3, that other species than electrons and holes can compensate the doping of a material, and hence lower the concentration of free charge carriers. If the V_M have a low formation energy, passivation of the defect is necessary to increase the concentration of free charge carriers.

If the sample is doped strongly n-type and V_M^{2-} has a high formation energy, N_a, $[V_O^{2+}]$ and p can be neglected and $n = N_d$. Then electrons are compensating the dopant atoms' charge. This is a requirement in many semiconductor applications. The defect reaction combining the metal vacancy with electrons is:

$$V_M^{2-} + O_O^0 \leftrightharpoons 2e^- + \frac{1}{2}O_2(g), \tag{2.17}$$

which inserted into Equation 2.13 becomes:

$$\frac{[V_M^{2-}][O_O^0]}{p_{O_2} n^2} = K \implies [V_M^{2-}] = N_d^{-2} p_{O_2}^{-1} \exp\frac{\Delta S}{k} \exp\frac{-\Delta H}{kT}. \tag{2.18}$$

Equation 2.18 shows that the concentration of defects are dependent of boundary conditions like ambience. The atmospheric conditions of a system will determine the chemical potential of a species. The chemical potential is the change in Gibbs free energy when an atom is removed or inserted to a system. The chemical potential will be useful when formation energies are calculated by density functional theory calculations. The expression for the chemical potential is

$$\mu_j = \mu_j^\circ + \mu_j^\circ(T) + RT\ln(a_j). \tag{2.19}$$

μ_j° is the standard chemical potential, $\mu_j^\circ(T)$ is its temperature dependency R is the gas constant and a_j is the activity of the atom. For solids the activity is unity at atmospheric pressure. For a gas the activity is the partial pressure.

The concentration of defects, both intrinsic and extrinsic, are limited by their solid solubility. The solid solubility is the upper limit of the defect concentration in the crystal, without creating higher dimensional defects like precipitations or changing in the crystal lattice. This solid solubility is determined by thermodynamic equilibrium and normally increase with temperature. The concentration of defects can be significantly higher than the solid solubility at a certain temperature if the defects are introduced at high temperatures and the solid is cooled down fast. The sample is not in thermal

equilibrium during the cool down, and thus, the defects do not have time to diffuse and form precipitates, get annihilated by recombination or diffuse out of the solid. Therefore, the resulting defect or dopant concentration resembles that of the high temperature, and not the thermal equilibrium at the operating temperature. Other methods to obtain concentrations above the solid solubility is to use ion implantation. Then the solid is bombarded with the extrinsic atom of interest, or an intrinsic atom to form vacancies or self-interstitials through collisions.

2.2.4 The harmonic transition state theory (HTST)

Defects need energy to be created (formation energy), but also to move and this energy is labelled migration energy. There are several ways to model the motion of a defect and one model that is widely used is the potential barrier. Figure 2.2.3 illustrate the change in potential energy when a point defect moves from one site, position M, to another, position M', through a transition site, position S. The change in potential energy from position M to position S is the migration energy, E_m. The rate of occurring jumps from M to M', is represented by a specific frequency, the jump frequency, Γ.

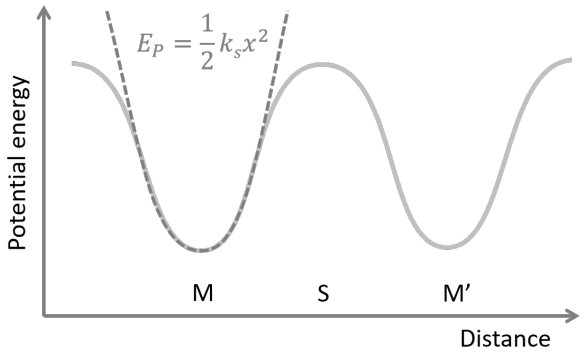

Figure 2.2.3: The potential energy barrier model illustrated by the potential energy path between two equivalent sites, M and M', separated by a saddle point site, S. The harmonic potential approximation is also illustrated, showing a fit around the minimum, where E_P is the potential energy, k_s is the spring constant and x is the distance.

The jump frequency, Γ, of these jumps is given by the attempt frequency, Γ_0, times the Boltzmann probability difference of the two different sites. The attempt frequency comes from the harmonic oscillator approximation, also shown in Figure 2.2.3, of the atom around the minimum of the potential energy curve. $\Gamma_0 = \frac{1}{\sqrt{2\pi}}\omega$ and ω is given by the equation:

$$\omega = \sqrt{\frac{k_s}{\mu}}, \tag{2.20}$$

where k_s is the spring constant and μ is the reduced mass. The attempt frequency, Γ_0, is usually the same magnitude of the characteristic oscillation frequency of the lattice, which is typically around 10^{13} s^{-1} and nearly temperature independent above room temperature [12]. The Boltzmann probability difference is found through the probability of the different sites:

$$\frac{P(S)}{P(M)} = \frac{\frac{Z_S}{Z_S+Z_M}}{\frac{Z_M}{Z_S+Z_M}} = \frac{\exp\left(\frac{-G_S}{kT}\right)}{\exp\left(\frac{-G_M}{kT}\right)} = \exp\left(\frac{-(G_S - G_M)}{kT}\right) = \exp\left(\frac{-\Delta G_m}{kT}\right), \tag{2.21}$$

where Z_s is the partition function of state s. The total partition function is the sum of the different Boltzmann factors for the different states [13]:

$$Z = \sum_s Z_s = \sum_s \exp\left(\frac{-E(s)}{kT}\right). \tag{2.22}$$

The migration energy is given by Gibbs free energy of migration at constant volume, and combined with the attempt frequency, the jump frequency is:

$$\Gamma = \omega_0 \exp\left(\frac{-\Delta G_m}{kT}\right) = \omega_0 \exp\left(\frac{\Delta S_m}{k}\right) \exp\left(\frac{-\Delta H_m}{kT}\right). \tag{2.23}$$

This last equation is the result of the harmonic transition state theory and it can also be used to calculate the dissociation rate of a defect complex.

2.3 Diffusion

Diffusion is unguided motion. A particle diffusing through a lattice is not moving because any force is acting on it. It moves because it has kinetic energy and vibrates. These vibrations have random direction and amplitude. The particle occasionally has a vibration that have the right direction and the right amplitude that the particle makes a jump into another lattice site. The motion is random and the particle may jump back into the former lattice position again. Because the motion is random, any non-uniform distribution of diffusing species will ultimately be uniformly distributed given enough energy and time. This section is based mainly on Ref.s [14] and [15].

2.3.1 Microscopic view on diffusion

Diffusion of a dopant at the microscopic level, is species moving from one position to another. This can occur by different paths and involve other species than the dopant. To make a useful model for diffusion at a macroscopic level, an understanding of the motion at this atomic scale is necessary. The diffusion mechanisms describe the microscopic motion, hence the most common diffusion mechanisms are presented next.

Diffusion mechanisms

In this work we are considering dopant diffusion. The dopant diffusion mechanisms in crystalline structures related here, are limited to the use of the open volumes in the structure or being aided by intrinsic defects. Hence, the mechanisms can be categorized into direct mechanisms, where no intrinsic defects are involved, and indirect mechanisms where intrinsic defects are involved. The most common mechanisms for dopant diffusion are illustrated in Figure 2.3.1 and explained below.

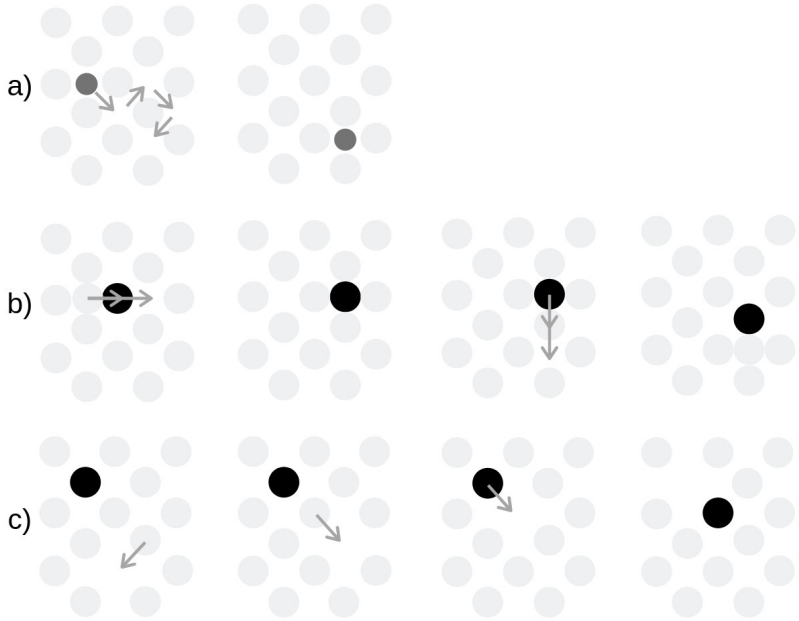

Figure 2.3.1: This figure illustrates the different most common diffusion mechanisms. a) is the interstitial mechanism, b) is the interstitialcy mechanism, c) is the vacancy mechanism

There are several direct mechanism for dopant diffusion. However, the only relevant one for semiconductors and oxides are the interstitial mechanism illustrated in Figure 2.3.1 a), since others involve several atoms moving simultaneously and are unlikely in most cases. The illustration shows the interstitial dopant atom moving in between the lattice sites from one interstitial site to another. It is evident that the diffusing dopant has to be small enough, or the cavities big enough, for this mechanism to be the energetically favourable one, considering that large lattice distortions would be necessary if that was not the case.

The rest of the mechanisms are indirect mechanisms, and the diffusing dopant is then dependent on intrinsic defects to move. When the intrinsic defect involved is the self-interstitial, the mechanism is correspondingly called the interstitialcy mechanism. It is depicted in Figure 2.3.1 b). Here the dopant is situated on a substitutional site until a self-interstitial diffuse to one of its nearest neighbour interstitial sites. The self-interstitial then pushes the dopant into an interstitial site. The two atoms move together in one jump, either in the same direction or with an angle between the two trajectories. Afterwards the dopant is situated at an interstitial site and the self-interstitial is annihilated. The dopant atom then pushes a lattice atom into an interstitial site, creating a new self-interstitial, and it ends up at a substitutional site again. The defect reaction involved is:

$$A_i \leftrightharpoons A_S + S_i \tag{2.24}$$

where A is the dopant atom and S is the lattice atom.

Figure 2.3.1 c) portrays the vacancy mechanism. The dopant atom is situated at a substitutional site and it is dependent on a vacancy diffusing to one of its nearest neighbour sites. When this occur

the dopant atom can jump into the vacancy and thereby exchange sites with it. The interaction of the two point defects is described by the defect reaction:

$$A_S V_S \leftrightharpoons A_S + V_S. \tag{2.25}$$

The mechanisms presented above are rather simple mechanisms, considering that in real materials the picture is often more complex. Some examples of this are; A dopant atom may diffuse with a mechanism combining the interstitial mechanism with either one of the latter two. These mechanisms are called the kick-out and the dissociative or the Frank-Turnbull mechanism. A combination of b) and c) are also possible, if both mobile vacancies and mobile self-interstitials are present in the material simultaneously. Models of mechanisms involving complexes of dopants and intrinsic defects moving together are discussed later when diffusion models are presented. First a more microscopical view of diffusion will be considered.

2.3.2 Fick's laws and diffusivity

As mentioned in the introduction, the random motion of diffusion will uniformly distribute a non-uniform distribution of diffusing species. Hence there will be a net flux of particles, J, in the opposite direction of the concentration gradient of that particle. That is what Fick's first law says:

$$J = -D\frac{\partial c}{\partial x}. \tag{2.26}$$

This is an equation that is valid in steady state and when the concentration does not change in time, i.e. it is time independent. Combining the Equation 2.26 with the continuity equation:

$$\frac{\partial J}{\partial x} = -\frac{\partial c}{\partial t} \tag{2.27}$$

results in Fick's second law of diffusion,

$$\frac{\partial c}{\partial t} = \frac{\partial}{\partial x}\left(D\frac{\partial c}{\partial x}\right), \tag{2.28}$$

which is time dependent. The probability constant inside the brackets,

$$D = D_0 \exp\left(\frac{-E_a}{kT}\right), \tag{2.29}$$

is called the diffusivity or the diffusion constant. D_0 is a pre-factor and E_a is the activation energy. The diffusivity is a measure of the rate of diffusion.

Solutions of Fick's second law (Equation 2.28), also known as the diffusion equation, with different boundary conditions will result in concentration profiles that can, e.g., be compared with experimental concentration profiles. From these profiles the diffusivity can be extracted. This gives some quantitative information about the diffusion, but the mechanism is still unknown. The diffusion equation is an important equation that will be elaborated on, but first the diffusivity is discussed.

A simplified model for diffusion

To illustrate how Equation 2.29 emerges, the one-dimensional picture of diffusing species is formulated. Diffusion from one plane of atoms in a lattice, plane 1, to another, plane 2, is considered. The lattice spacing is λ and the net flux of atoms jumping from plane 1 to plane 2, J, is then given by:

$$J = j_{12} - j_{21} = n_1\Gamma_{12} - n_2\Gamma_{21}, \tag{2.30}$$

where n_a is the number of diffusing atoms in plane a per unit area and Γ_{ab} is the jump frequency from plane a to plane b. N is the average number of atoms per unit area. Thus, the number of diffusing atoms in plane 1 and 2 are given by $n_1 = N - \frac{1}{2}\lambda\frac{dN}{dx}$ and $n_2 = N + \frac{1}{2}\lambda\frac{dN}{dx}$ respectively. If the jump frequency in each direction is the same, and $\Gamma_s = \Gamma_{12} + \Gamma_{21}$, the flux is hence:

$$J = -\frac{1}{2}\lambda\Gamma_s\frac{dn}{dx}.$$

The relation between the concentration of atoms, c, and the number of atoms per unit area, i.e. $\frac{N}{\lambda} = c$, is used to express the flux with concentration instead of number of atoms per unit area like this:

$$J = -\lambda^2\Gamma_s\frac{dc}{dx}.$$

This is Fick's first law with $D = \lambda^2\Gamma_s$:

$$J = -D\frac{dc}{dx}.$$

An expression for the diffusion coefficient in one dimension is hence

$$D = \lambda^2\Gamma_s. \tag{2.31}$$

If the activation energy, E_a, is assumed to be simply the migration enthalpy, ΔH_m, Γ_s is the same jump frequency, Γ, as in Equation 2.23 from the potential barrier model. The case where these assumptions do not hold, will be discussed later.

By inserting Equation 2.23 into Equation 2.31 and setting $D_0 = \lambda^2\Gamma_0\exp\left(\frac{\Delta S}{k}\right)$ the expression in Equation 2.31 is related to the expression in Equation 2.29:

$$D = \lambda^2\Gamma_0\exp\left(\frac{\Delta S}{k}\right)\exp\left(\frac{-\Delta H_m}{kT}\right) = D_0\exp\left(\frac{-E_a}{kT}\right). \tag{2.32}$$

The diffusivity of a dopant in a crystal, is most often investigated in one direction, into the sample. The equations from the one-dimensional picture is hence a useful result.

Arrhenius behaviour

If D_0 and E_a are independent of the temperature, the diffusivity will show an Arrhenius behaviour. The natural logarithm of the diffusivity is thus linearly proportional to the inverse of the temperature:

$$\ln D = \ln D_0 - \frac{E_a}{k}\frac{1}{T}. \tag{2.33}$$

To find E_a, an isochronal measurement series can be conducted. Then the sample is heat treated at a range of temperatures for the same amount of time. The diffusivity is extracted at each temperature and by plotting $\ln D(T)$ versus $1/T$, E_a can be extracted using a linear regression. Alternatively, an isothermal measurement series can be conducted. An isothermal process is a process at constant temperature. The amount of time is changed for each heat treatment and the diffusivity is expected to be the same, because no parameter in Equation 2.33 is changed.

Higher complexity

From Equation 2.32 $E_a = \Delta H_m$ and $D_0 = \lambda^2 \Gamma_0 \exp\left(\frac{\Delta S}{k}\right)$. This is not always the case, and some examples will follow. If the mechanism of diffusion is an indirect mechanism, the diffusion involve more than one thermally activated process. Thus, the activation energy may be combination of different activated processes; The migration energy and the formation energy of the intrinsic defect involved may also be included in the activation energy, depending on the conditions. Since a defect reaction is involved in indirect diffusion mechanism, the binding energy, E_b, of the complex and the dissociation energy, E_d, can also be included in the activation energy.

Some phenomenological models of diffusion can only extract the activation energy of the diffusion, and consequently do not give any information about the thermally activated processes it represents. Hence, no fundamental information about the physics involved in the mechanism is revealed. Other models manage to separate the different parts of the activation energy and extract more information, by doing some simplifications. This will be discussed further when the different models are presented.

The jump distance, λ, may not be directly in the probed direction, i.e. normal to the surface plane of the crystal investigated, since diffusion is random motion. Then λ^2 is replaced with βa^2, a projection of the jump distance along the probed direction. If the crystal is simple cubic, the jumps are assumed to be made to the nearest neighbour and a is the lattice constant. This is not the case if the crystal has a structure with lower symmetry.

If the loss of the assumption that a jump is completely independent on the preceding jump, a correlation factor, f, which is a constant between 0 and 1, is added in D_0. The correlation between succeeding jumps are complicated for dopant diffusion, indirect mechanisms and complex crystal structures. It is difficult to calculate analytically, but Monte Carlo simulations might give a numerical value. A thorough description is outside the scope of this thesis, but it is discussed in more detail in Ref. [14].

After all of these additions in complexity the diffusivity is:

$$D = \beta a^2 f \Gamma_0 \exp\left(\frac{\Delta S_{tot}}{k_B}\right) \exp\left(-\frac{E_a}{k_B T}\right) = D_0 \exp\left(-\frac{E_a}{k_B T}\right), \tag{2.34}$$

where ΔS_{tot} represents the combined entropy change from all the thermally activated processes included in the E_a. The entropy will also change with the mechanism similarly to the enthalpy or activation energy, and may, for example, include both a formation entropy and a migration entropy.

The mechanism of a dopant atom may change with temperature and the Arrhenius plot then have two, or more, linear regions with different slopes and hence different activation energies. Each linear region will then represent the dominance of one of the mechanisms. The same situation can occur if the structure is polycrystalline and contains grains and grain boundaries. Then the linear region at low temperatures, in the Arrhenius plot, represents the dominance of grain boundary diffusion and the linear region, will represent the dominance of in-grain diffusion at high temperatures.

The isotope effect of diffusion

In this work, deuterium is used in the experimental part, while hydrogen is studied in the theoretical part. Hence, it is assumed that the properties extracted for deuterium in β-Ga_2O_3 are applicable to hydrogen as well. Nonetheless, the isotope effect between the two should be explored. One consequence of the difference in mass between hydrogen and deuterium arrive in the attempt frequency, Γ_0, which is included in both D_0 and ν_0 and contain ω (Equation 2.20). When the mass of deuterium replace the mass of hydrogen, the reduced mass and hence Γ_0 will scale with a factor of $\frac{1}{\sqrt{2}}$. This is referred to as the classical effect. The prefactors for deuterium diffusion and dissociation rate is hence smaller than that of hydrogen.

Another consequence of the mass difference between hydrogen and deuterium is in the zero-point energy, which is larger for hydrogen than for deuterium, which have the effect that the activation energy of a jump is 0.04-0.06 eV smaller for hydrogen than for deuterium [16]. In addition, hydrogen will exhibit a lower sticking probability than deuterium [16]. These effects of the isotopic differences may counteract each other and the effect of the difference in activation energy is within the typical accuracy of activation energies. The prefactors for diffusion also have larger margin of error than the classical effect. In the end, the difference between the two isotopes are often neglected in diffusion studies, although the classical effect is used to identify hydrogen peaks in the absorbency spectrum from Fourier transform-infrared spectroscopy.

2.3.3 Mathematical formulation of diffusion

Point defects are very small and it is difficult to find out how a point defect moves through a lattice. Nevertheless, there are different ways of modelling diffusion to extract the mechanism. Molecular Dynamics models atoms as point charges and uses Newton's laws of motion and different potentials to simulate their interaction with each other. It utilizes Monte Carlo simulations to find the lowest potential energy of the system. Monte Carlo can also be used alone with random numbers deciding for example which neighbouring atom a vacancy will exchange with, using probabilities and random jumps. Another method to model diffusion is through density functional theory (DFT) which uses quantum mechanics and electron charge densities to calculate the energy of a structure. These energy calculations can be used to compare different native point defects and find which will be more abundant. That again, might indicate which one that are involved in the diffusion mechanism. DFT can also be used to calculate migration energies of different diffusion paths for a point defect.

These methods are microscopic methods that can tell us a lot about the defects, but it is difficult to

compare the data directly with experimental data. This is where continuum theory (CT) is different. It employs partial differential equations, that is, variations of the diffusion equation (Equation 2.28). The solution of the equations can be directly compared with experimental diffusion profiles to extract the diffusivity and the activation energy. The shape of the profile might, in some cases, give information about the mechanism behind the profile. But in other cases, two mechanism, for instance the vacancy mechanism and the interstitialcy mechanism, have the same mathematical formulation and render the same diffusion profile shapes.

An even more useful solution is a combination of CT and other methods and experiments. Because some mechanisms have the same mathematical formulation, and one cannot use CT alone to find the diffusion mechanism. Bracht, for example, used isotope heterostructures to model the movement of self-diffusion together with the movement of the dopants [17]. In this work a combination of the microscopic view with DFT and a more macroscopic view through CT, is used to extract information about the diffusion mechanism.

Analytic and numerical solutions

Variations of the diffusion equation is used in CT, but first the solutions of the unchanged diffusion equation are presented. The diffusion equation (Equation 2.28) has two common analytic solutions which arise from different boundary conditions. The first one is called the complementary error function or semi-infinite source model:

$$c(x,t) = c_s \mathrm{erfc}\left(\frac{x}{2\sqrt{Dt}}\right). \tag{2.35}$$

The boundary conditions that give rise to this solution of the diffusion equation is a constant concentration at the surface, $c(0,t) = c_s$, while the concentration in infinity is zero, $c(\infty,t) = 0$ and that the concentration in the beginning is zero, $c(x,0) = 0$.

Another common analytical solution to the diffusion equation is the Gaussian curve:

$$c(x,t) = \frac{Q_T}{\sqrt{\pi Dt}} \exp\left(\frac{-(x-x_0)^2}{4Dt}\right). \tag{2.36}$$

This solution arises when the number of diffusing species inside the sample does not change, i.e. $\int_{-\infty}^{\infty} c(x,t)dx = Q_T$, where Q_T is the dose. The dose is the number of diffusing species per area. This solution also assumes that the concentration is zero everywhere except at the surface at $t = 0$, i.e., $c(x,0) = 0z \neq 0, c(0,0) = \delta(x)$ and that the concentration approaches zero far away from the surface, $c(\infty,t) = 0$.

These analytical solutions can be a suitable starting condition when simulating diffusion. A different approach is to solve the diffusion equation numerically. Then, one can use experimental profiles as initial conditions and compare the behaviour of the experimental data after annealing with the solution from the numerical simulation. This is carried out by changing the diffusivity until the simulated curve and the experimental data overlap within a defined error margin. With more complicated diffusion models, as the next section will explain, there are more parameters to fit than the diffusivity.

Modulations of the diffusion equation

The diffusion equation alone, can often describe the diffusion of a vacancy and diffusion through the interstitial mechanism, but dopant diffusion is often more complicated. Therefore, modulations of the diffusion equation have been developed, and a few of the variations will be discussed here. One of them is Fair's model [18]. Fair's model is a model for diffusion through the vacancy mechanism, but it includes the contribution of vacancies in different charge states. It utilize Fick's laws for diffusion, but the diffusion constant is modelled as a sum of different diffusivities. Each diffusivity represents a different charge state of the vacancy, weighted by its probability to exist at different doping levels:

$$D_{tot} = h\left[D^0 + \left(\frac{n}{n_i}\right)D^- + \left(\frac{p}{n_i}\right)D^+ + \left(\frac{n}{n_i}\right)^2 D^{2-} + \dots\right], \tag{2.37}$$

where $D^q = D_0^q \exp\left(-\frac{E_a^q}{kT}\right)$ with $q = 0, -, +, 2-, 2+, \dots$. n is the electron concentration, n_i is the electron concentration under intrinsic conditions and h is a factor between 1 and 2 that enhances the diffusion of charged species in an electric field, originating from the spacial difference in the Fermi-level. With in-diffusion of a dopant, the diffusing specie introduce extra charge carriers in the vicinity of the dopants. This can make a spacial difference in the Fermi-level, if the material has a low dopant concentration.

Another modulation that can be used for implanted profiles, is the solid solubility model [19]. Implanted profiles will be discussed further later. In this model, the concentration of diffusing species is limited by the solid solubility. One assumes that some of the implanted species are in precipitates, larger complexes or trapped in higher dimensional defects and cannot move. The concentration is then given by:

$$c_{SS} = \frac{c \cdot SS}{c + SS}, \tag{2.38}$$

where SS is a solubility constant. c_{SS} is, in this model, the concentration used in the diffusion equation to simulate the diffusion.

Combining chemical reactions with Fick's laws

Indirect mechanisms of dopant diffusion can be explained by a defect reaction. For instance, the defect reaction involved in the interstitialcy mechanism,

$$A_S S_i^v + (v + 1 - u)e^- \leftrightharpoons A_S^- + S_i^u. \tag{2.39}$$

which here also includes various charge states and the dopant, A, is assumed to be an acceptor. v is the charge state of the complex and u the charge state of the self-interstitial. There are two different equations representing the reaction involved in the interstitialcy mechanism. The first describes the complete annihilation of the interstitial like described before. The second desribes the formation of a dopant atom-self-interstitial pair that can diffuse together as in Equation 2.39.

Combining the involved chemical reactions with Fick's laws has been put in a mathematical framework by Bracht [17, 20]. It includes the different charge states of point defects and also drift of the species caused by an electric field given by the change in charge carrier concentration. An example of this approach is shown for the interstitialcy mechanism. If all species in Equation 2.39 are able to diffuse, the diffusion is modelled by the three connected differential equations:

$$\frac{\partial[A_S^-]}{\partial t} = \frac{\partial}{\partial x}\left(D_{A_S^-}\frac{\partial[A_S^-]}{\partial x} + \frac{[A_S^-]D_{A_S^-}}{p(x)}\frac{\partial p(x)}{\partial x}\right) - F \tag{2.40}$$

$$\frac{\partial[A_S S_i^v]}{\partial t} = \frac{\partial}{\partial x}\left(D_{A_S S_i^v}\frac{\partial[A_S S_i^v]}{\partial x} + \frac{[A_S S_i^v]D_{A_S S_i^v}}{p(x)}\frac{\partial p(x)}{\partial x}\right) + F \tag{2.41}$$

$$\frac{\partial[S_i^u]}{\partial t} = \frac{\partial}{\partial x}\left(D_{S_i^u}\frac{\partial[S_i^u]}{\partial x} + \frac{[S_i^u]D_{S_i^u}}{p(x)}\frac{\partial p(x)}{\partial x}\right) - F, \tag{2.42}$$

where the first term in all equations are the diffusion part from Fick's second law, the second term is due to drift. F is a reaction term arriving from Equation 2.39:

$$F = k_+[A_S S_i^v]C_o p^{(v+1-u)} - k_-[A_S^-][S_i^u]n_i^{(v+1-u)} \tag{2.43}$$

where k_+ is the forward reaction rate and k_- is the backward reaction rate of the reaction shown in Equation 2.39, C_o is the number density of substitutional lattice sites.

Similar differential equations can be written for the other mechanisms and diffusion of a donor. It is also possible to combine several mechanisms in this way, making this model very useful if a dopant diffuses through several mechanisms simultaneously. The amount of differential equations makes it a complicated model. If the dopant diffusion is simpler, some approximations can be made to decrease the number of partial differential equations.

A reaction diffusion model which assumes that the dopant cannot move without an intrinsic defect, thus it moves only in a complex with the intrinsic defect, is described below. The concentration of the self-interstitial involved in the mechanism are assumed to be determined from the charged species involved in the diffusion, as shown for the vacancy in Section 2.2. The full model is explained for Al diffusion in ZnO in Ref. [21].

After these simplifications the model is left with only one partial differential equation. Illustrated here with a self-interstitial involved:

$$\frac{\partial[A_S S_i]}{\partial t} = D_{A_S S_i}\frac{\partial^2[A_S S_i]}{\partial x^2} - R, \tag{2.44}$$

where the reaction term is

$$R = \frac{\partial[A_S]}{\partial t} = \nu[A_S S_i] - \kappa[S_i][A_S]. \tag{2.45}$$

ν is the dissociation rate and κ is a capture constant. ν is described by the equation $\nu = \nu_0 \exp\left(\frac{-E_d}{k_B T}\right)$ where ν_0 is assumed to be the vibrational frequency of the lattice and E_d is the dissociation energy of the complex. In this model the complex moves together, so an increased capture increases the diffusion. The dopant atom remains in its substitutional site until a defect, here the self-interstitial, arrives next to it. The capturing is therefore determined by the diffusivity of the vacancy through $\kappa = 4\pi r D_{S_i}$, and the concentration of the isolated species, $[A_S]$ and $[S_i]$. By describing the backwards and forward reaction rates in more detail than the constants, k_+ and k_-, in Bracht's description above, the model can separate the dissociation energy from the activation energy. Thus, gaining more information about the physics behind the diffusion.

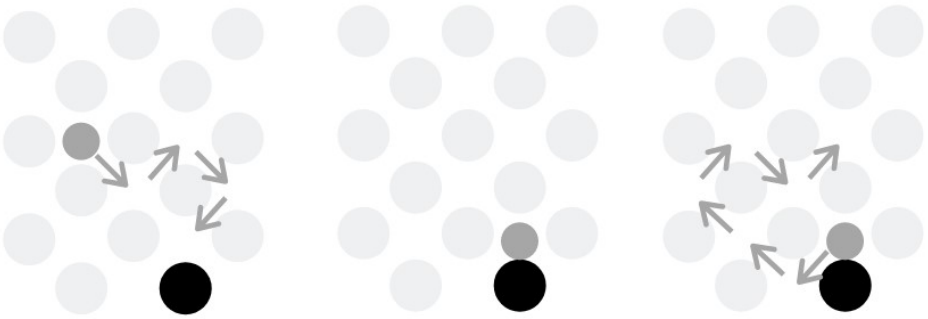

Figure 2.3.2: An illustration of trap limited diffusion.

A similar model, in the mathematical sense, is the trap limited diffusion model. The mechanism of the trap limited diffusion is illustrated in Figure 2.3.2. It depicts how the dopant atom moves interstitially by the interstitial mechanism, but is trapped by a point defect in the crystal. The dopant atom therefore has to dissociate from this trap to be able to diffuse further on by the interstitial mechanism. The potential energy of the interstitial atom is illustrated in Figure 2.3.3. It shows the potential energy path from the trap into an interstitial position. The different activation energies, the binding energy, E_b, the dissociation energy, E_d, and the migration energy, E_m, involved are marked and their relation is hence:

$$E_d = E_b + E_m. \tag{2.46}$$

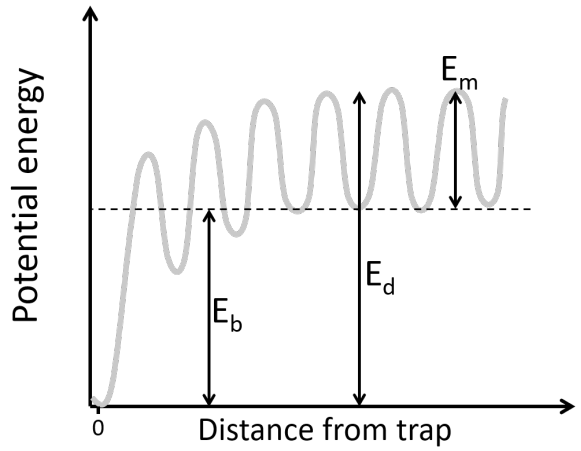

Figure 2.3.3: The potential energy of the hydrogen close to the trap, showing the binding energy, E_b, the dissociation energy, E_d and the migration energy, E_m.

The differential equation describing the diffusion depicted in Figure 2.3.2 is:

$$\frac{\partial[A_i]}{\partial t} = D_{A_i}\frac{\partial^2[A_i]}{\partial x^2} - R, \tag{2.47}$$

where the reaction term is

$$R = \frac{\partial[tr_S A_i]}{\partial t} = \kappa[tr_S][A_i] - \nu[tr_S A_i]. \tag{2.48}$$

Here $[tr_S A_i]$ is the concentration of filled traps, the complex between the trap and the dopant atom, and $[tr_S]$ is the concentration of empty traps. The defect reaction describing the capturing and dissociation is hence:

$$tr_S A_i \leftrightharpoons A_i + tr_S. \tag{2.49}$$

In the trap limited model the diffusing species move between the trapping events and therefore dissociation increases diffusion. In this model the trapping is limited by the diffusion of the dopant atom through $\kappa = 4\pi r D_{A_i}$ and the concentration of empty traps, $[tr_S]$, and free dopant atoms, $[A_i]$. This modulation of the diffusion equation is the main model that is used to simulate the diffusion in this work, and a detailed description of it is presented later in this thesis.

2.4 Crystalline β-Ga_2O_3 and previous work

This section will present relevant information about β-Ga_2O_3 and its properties. It will show the crystal structure of β-Ga_2O_3 and also give an impression of the two orientations of crystals investigated. In addition to this, the gallium vacancy that is investigated in a complex with hydrogen is also described. The growth method of the samples is explained and eventually some previous data about hydrogen in β-Ga_2O_3 is submitted.

The key properties of β-Ga_2O_3 is the material's high breakdown field of 8 MV/cm and its wide band gap of ~4.8 eV. β-Ga_2O_3's structure has low symmetry, and many of its properties are anisotropic.

This includes anisotropic thermal conductivity [22] and anisotropic optical properties [23]. This suggests that the diffusivity also will be anisotropic.

2.4.1 Structure, orientation and sites

Gallium oxide can have several polymorphs, the most stable one at atmospheric conditions is the β-phase. The structure of β-Ga_2O_3 is monoclinic and described by the space group C2/m. Figure 2.4.1 shows the unit cell of β-Ga_2O_3. The unit cell can be repeated in all directions to make the crystal. a, b, c and β are marked in the figure and represent the lattice parameters of the crystal. In the monoclinic crystal structure the lattice parameters a, b and c do not have the same length and all angles are 90 °except β.

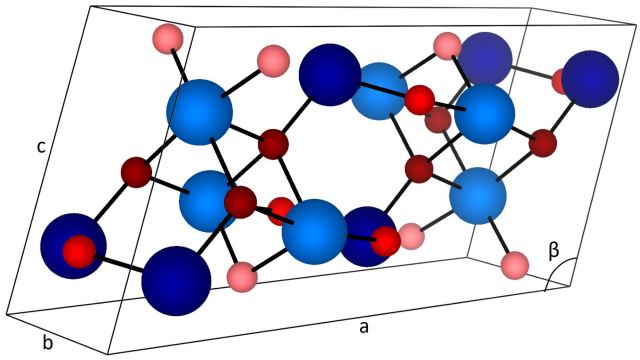

Figure 2.4.1: The monoclinic unit cell of β-Ga_2O_3. a, b, c and β are marked in the figure and represent the lattice parameters of the crystal.

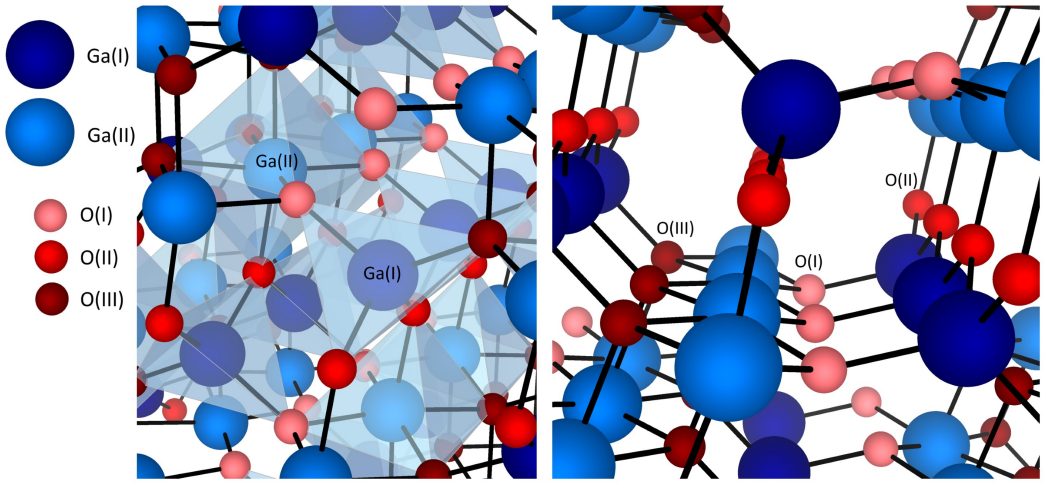

Figure 2.4.2: The different site in the β-Ga_2O_3 structure: Two inequivalent gallium sites and the three inequivalent oxygen sites. The Ga(I) has a tetrahedral coordination and Ga(II) has an octahedral coordination, while O(III) has a tetrahedral coordination and O(I) and O(II) have a trigonal planar coordination.

Figure 2.4.2 shows the two inequivalent gallium sites and the three inequivalent oxygen sites. The Ga(I) has a tetrahedral coordination and Ga(II) has an octahedral coordination, while O(III) has

a tetrahedral coordination and O(I) and O(II) have a trigonal planar coordination. The latter two oxygen sites are different from each other due to their different gallium neighbours. The labelling scheme used here was introduced by Geller [24].

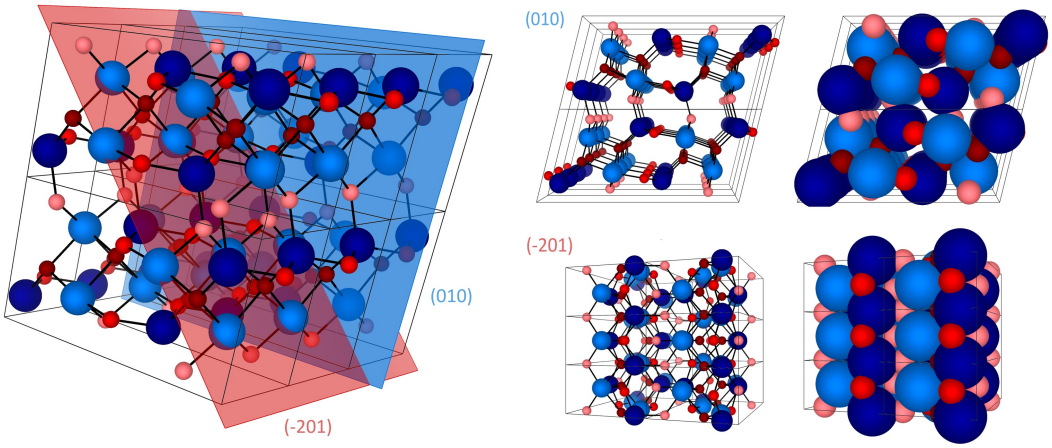

Figure 2.4.3: Illustration of the two crystal orientations investigated in this work. To the left: The surface plane of the two crystal orientations investigated experimentally in this work, the (010) and the (-210), shown in a supercell of β-Ga_2O_3. To the right: The supercell is angled to give a view of the structure in the two different orientations, with the surface plane being the plane of the paper. The diffusion direction in these orientations are therefore into the plane of the paper. Here shown with stick-and-ball and space-filling balls, to give an idea of the structure and a more realistic view of the cavities, respectively.

Figure 2.4.3 shows the surface plane of the two crystal orientations investigated experimentally in this work, the (010) and the (-210), shown in a supercell of β-Ga_2O_3. To the right the supercell is angled to give a view of the structure in the two different orientations, with the surface plane being the plane of the paper. The diffusion direction in these orientations are therefore into the plane of the paper, and in this work diffusion in the (010) orientation will refer to diffusion normal to the 010 plane, the same holds for diffusion in the (-201) orientation. The angled supercells reveal that (010) orientation is evidently more open than the (-201) orientation.

Ab initio calculations on the defect structure of β-Ga_2O_3 has shown that in n-type β-Ga_2O_3 the gallium vacancies have low formation energies in oxygen rich conditions. Oxygen interstitials have slightly higher formation energies than the gallium vacancies. However, in oxygen poor conditions the oxygen vacancy has the lowest formation energy. The gallium interstitial has the highest formation energy for both conditions in n-type β-Ga_2O_3. For Fermi levels above 4 eV, the dominating intrinsic defects are the gallium vacancies, the oxygen vacancies and the oxygen interstitial [25].

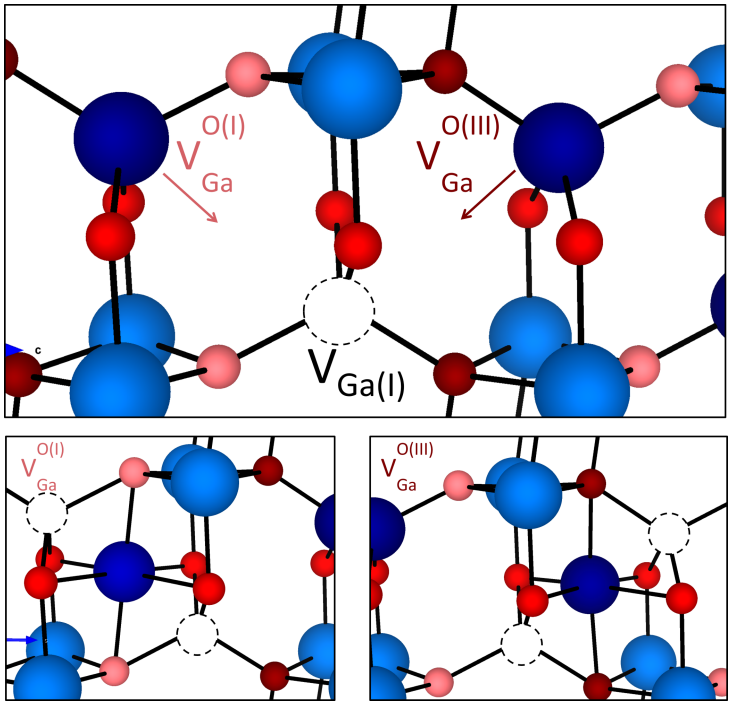

Figure 2.4.4: An illustration of how the two different shifted vacancies, $V_{Ga}^{O(I)}$ and $V_{Ga}^{O(III)}$, are created from $V_{Ga(I)}$. The missing atoms are marked by white discs with a dotted outline.

The two different gallium sites result in two different gallium vacancies as well, these are denoted $V_{Ga(I)}$ and $V_{Ga(II)}$. However, from density functional theory it is found that $V_{Ga(I)}$ is metastable. Figure 2.4.4 reveals how the neighbouring gallium atom moves towards $V_{Ga(I)}$ and create a more stable shifted vacancy. There are two alternative configurations for this shifted vacancy, depending on which of the two neighbouring Ga moves towards $V_{Ga(I)}$. These are named $V_{Ga}^{O(I)}$ and $V_{Ga}^{O(III)}$, the labels come from what oxygen type the shifted Ga atom is bonded to. They are both bonded to four O(II), but the last two are either two O(I) or two O(III). Other density functional theory calculations on the migration of the vacancies in β-Ga_2O_3 has determined that the V_{Ga}s have a lower migration energy than the V_Os. In the same research, V_{Ga} was found to be mobile around 500 K $\simeq$ 230 °C [26].

2.4.2 Crystal growth and doping

An advantage with β-Ga_2O_3 is its growth related properties. The material can be grown from melt by the following techniques; Czochralski [27], Float Zone [28] and Edge-defined Film-fed Growth (EFG) [2]. The samples used in this work was grown with the EFG method. In this technique, a high-purity Ga_2O_3 powder is melted inductively in an Ir crucible in a gas mixture of O_2 and N_2. The crucible has a die, a shaping tool, as illustrated in Figure 2.4.5. As/After the powder melts, it flows into the die. A seed crystal is placed in contact with the melt inside the die and the crystalline material is pulled out. For β-Ga_2O_3 growth, the growth direction is [010] and the co-called principle plane is (-201) [2]. The different samples in this work are thereby made by cutting the crystal in different directions.

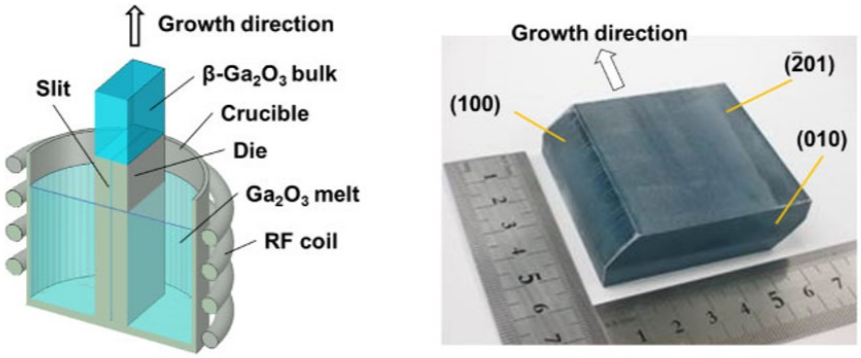

Figure 2.4.5: A drawing of the EFG process (left) and the β-Ga_2O_3 crystal (right) grown from the method taken from Kuramata et al.'s paper on High-quality β-Ga_2O_3 single crystals growth by edge-defined film-fed growth [2].

The intentional n-type doping is introduced by mixing either SnO_2 powder or SiO_2 powder with the Ga_2O_3 powder, because Si and Sn are the most common n-type dopants in β-Ga_2O_3. An unintentional dopant however is Si from the Ga_2O_3 source, which can be compensated by the deep acceptors Fe and Mg. And an other common substitutional impurity in the samples is Ir from the crucible. The β-Ga_2O_3 crystals are always unintentionally doped n-type, which is attributed mainly to Si mentioned already and the other substitutional impurities Ge, Sn, F and Cl which have been found, from density functional theory, to act as shallow donors in β-Ga_2O_3 [6]. Hydrogen was, in addition, shown to be a shallow donor both as an interstitial ($H_i = (OH)_O$) and substituting the oxygen (H_O) and hence could be contributing to the unintentional doping [29]. Contrary to n-type doping, p-type doping is difficult to do in β-Ga_2O_3 due to for example self-trapped holes and a low E_V making it difficult to find shallow acceptors.

2.4.3 Hydrogen in β-Ga_2O_3

Diffusion of hydrogen in β-Ga_2O_3 has not been thoroughly investigated before. Although some thermal stability experiments were performed, and some values for the diffusivity were extracted from these experiments [30]. This includes an activation energy for diffusion of deuterium at 0.30 ± 0.08 eV for (-201) oriented β-Ga_2O_3 using the FLOOPS simulator [30].

Hydrogen in β-Ga_2O_3 have been investigated with an emphasis on the configuration with the help of Fourier transform infrared spectroscopy [31]. In those experiments, two hydrogen in a complex with one of the shifted gallium vacancies, $V_{Ga}^{O(III)}H_2$, was found to be the dominant O-H-center in β-Ga_2O_3. Some ab initio calculations has also been carried out on hydrogenated gallium vacancies [29]. These calculations were only performed on the different gallium vacancies with one hydrogen. From the research the presence of hydrogen in β-Ga_2O_3 was found to have several advantages by contribution to the charge carrier concentration both by acting as a donor and passivating the deep acceptor, the gallium vacancy. The migration energy of the interstitial hydrogen was also mentioned in this research, and stated as $E_m = 0.34$ eV.

Chapter 3

Method

This chapter covers the different methods employed to investigate deuterium diffusion in β-Ga_2O_3. It includes both the experimental methods, density functional theory and an introduction to the diffusion modelling applied to the experimental diffusion profiles. Density functional theory is presented here considering it was used as a complementary technique to the diffusion modelling.

3.1 Experimental methods

Several experimental instruments were used in the experiments for this thesis. The different experimental instruments will be described below with a main emphasis on Secondary Ion Mass Spectrometry (SIMS).

3.1.1 Ion implantation

This section is based on Ref. [32, Ch. 5]. Ion implantation is a technique to implant elements into a material. It is used to implant foreign atoms into a sample, for example, to dope a semiconductor. It can also be used to create intrinsic defects or amorphize part of the sample. Figure 3.1.1 shows the schematics of the ion implantation instrument. It portrays the ion beam's path from the source to the target; The source, either inform of a gas or a solid, is ionized and includes different isotopes of the element of interest. Next, the ions are extracted using an electric field and collected into an ion beam. The desired ion isotope is separated from the other ions and isotopes, utilizing a magnetic field and slits, this occurs in the magnetic particle filter, see Figure 3.1.1. This process will be described in further detail in the section about SIMS below. The ions are thereafter accelerated by an electrical field towards the target. Finally, different deflectors are employed to steer the beam and towards the surface of the target material.

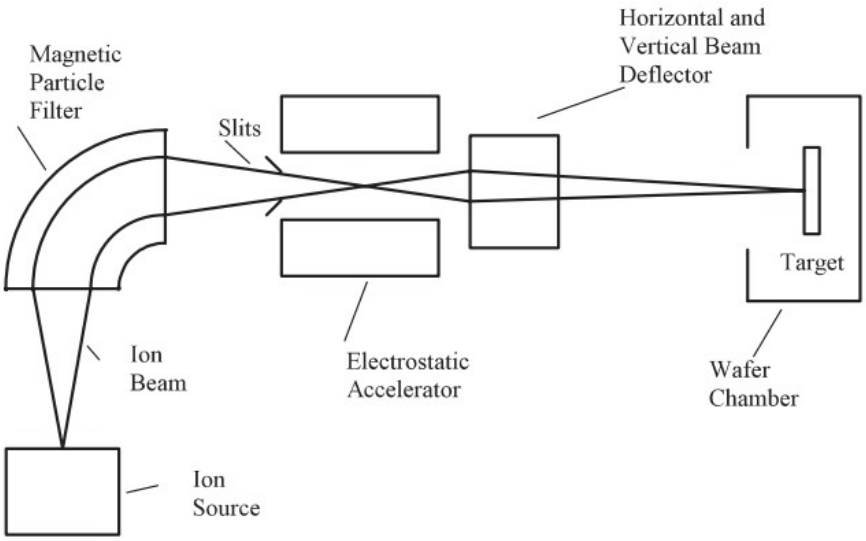

Figure 3.1.1: An illustration of the ion implantation set-up. Reprinted from Ref. [33]

The ions are implanted into the sample and collide with the nuclei and the electrons in the material. The interactions between the implanted ion and the nuclei decrease the energy and deflect the path of the implanted ion. Likewise, the electrons will also interact with the implanted ion and energy will be transferred. The energy of the incoming ion and the stopping power of the material determine the projected range, R_P, of the implanted ions, which is the distance along the implantation axis. Modelling of the two types of stopping is elaborated in Ref. [32, Ch. 5], and it will not be discussed in detail here. The dose of implanted ions is determined by the ion current and the implantation time, and the depth is determined by the energy of the ions, given by the applied voltage. In this work, the Stopping and Range of Ions in Matter (SRIM) software [34] was used to determine the voltage to be applied to the implanted ion in order to obtian a desired projected range. The software was also used to simulate the implantation profiles. Figure 3.1.2 a) displays a simulated implantation profile and how an implantation with two different energies (voltage applied to the terminals of the accelerator) results in two different implantation depths. Figure 3.1.2 b) demonstrate the paths of the simulated ions, which also show how the ions are deflected by collisions with the nuclei in the sample. The simulation assumes an amorphous material and shows deuterium implanted, but with the density of β-Ga_2O_3.

An effect that may arise when implanting into crystalline samples at specific angles, i. e. along one of the crystal planes, is called channeling. Channeling is the effect caused by implanting into open channels in the structure. In the open channel the angle and the energy of the implanted atom result in a reduced energy transfer between the ion and the host material, and hece the ion will end up deeper into the material compared to that predicted by SRIM.

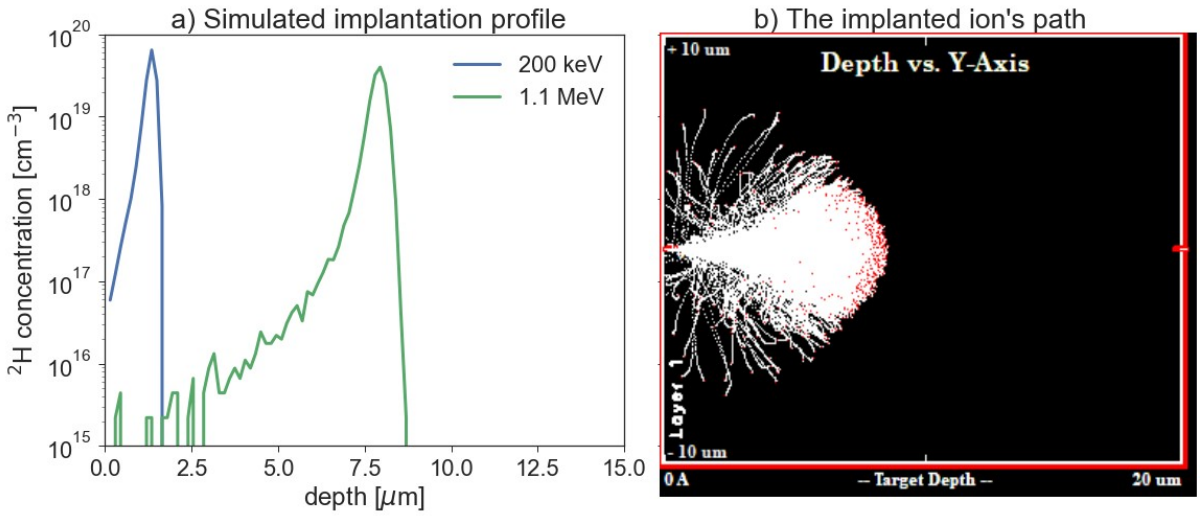

Figure 3.1.2: a) The simulation of the implantation profile of deuterium implanted into amorph gallium oxide and b) the simulated implantation paths. Both plots were simulated using Ref. [34].

3.1.2 Secondary Ion Mass Spectrometry (SIMS)

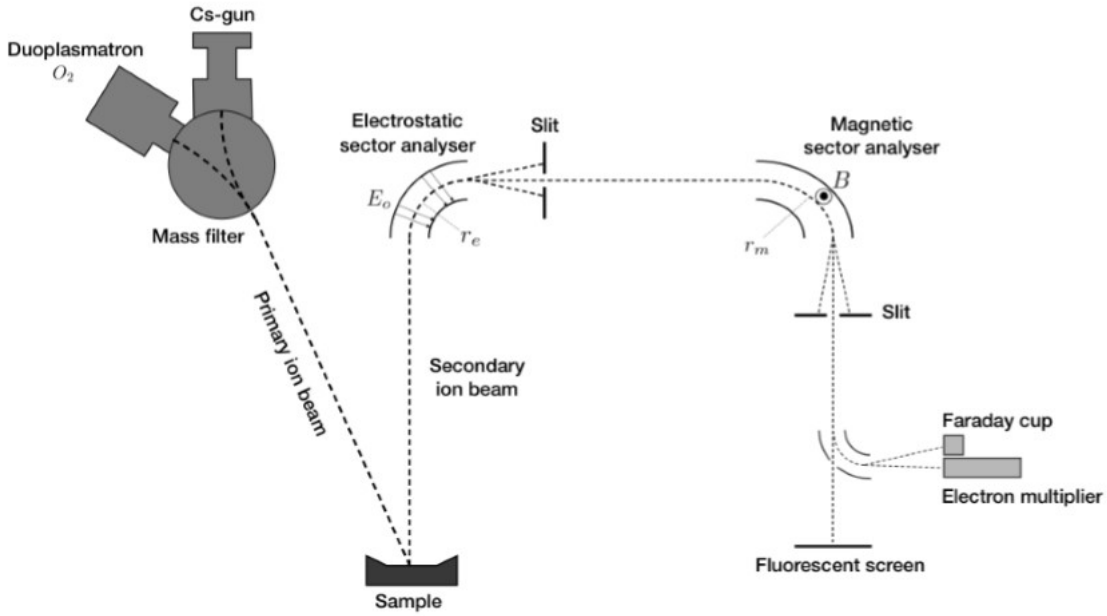

Figure 3.1.3: A simplified illustration of the Cameca IMS-7f SIMS instrumental set-up, the specific instrument used in this work. The path of the primary ions towards the sample are shown, as well as the path of the secondary ions through the analysers and eventually to the detectors. Reprinted from Ref. [35]

Secondary Ion Mass Spectrometry (SIMS) is a technique used to measure the concentration of impurities in materials. As Figure 3.1.3 illustrate, a primary ion beam sputter the surface of the sample. The sputtering process results in the release of atoms from the sample's surface. A fraction

of these atoms are ionized in the process. These secondary ions are collected by accelerating them down a secondary beam line consisting of both an electrostatic sector analyser and a magnetic sector analyser, before it reaches one of the three different detectors. All the steps of the SIMS measurement process will be discussed further in this section.

The instrument used to perform measurements in this work was a magnetic sector dynamic SIMS (Cameca IMS-7f). The instrument can be operated in several modes, where the main mode used in this work were depth profiling. In depth profiling, a part of the sample surface is rastered with the primary ion beam. The ions of interest are collected, separated by their mass per charge ratio using a magnetic field, and counted in the detector. This rastering continues in the same area of the sample and create a crater in the sample surface. Thus, the signal representing the number of ions of interest is recorded as a function of the time.

Another relevant operating mode is to obtain a mass spectrum. In the mass spectrum mode, the material is investigated for a range of different elements. The sample is rastered in the same manner, but instead of filtering out the ions of interest, the magnet is scanned so that each mass per charge ratio reach the detector at a specific time. The result is a spectrum of intensity of the signal as a function of mass per charge ratio.

The various steps involved in the SIMS measurement will be explained in detail below. This review will explain how the intensity of the signal (counts per second) at a specific time, can be converted into concentration at a specific depth to acquire depth profiles. This section is based on Ref. [36].

Primary Beam and Ion Source

The ion sources available in the Cameca IMS-7f give primary ions of cesium or oxygen. The source used in the measurements is chosen with respect to the electron affinity and ionization potential of the impurity to be measured. Since cesium is electropositive it is the best choice for the depth profiles of deuterium since $^2H^+$ is easier to create than $^2H^-$. One the other hand, the oxygen source is a better choice for the most common impurities in β-Ga_2O_3, considering their electron affinity. The primary optic set-up has four lenses and additional deflectors to align the primary beam.

Sputtering

The primary ion beam sputters the sample surface. Sputtering is a removal of atoms from the surface of a sample by bombardment of ions from an ion beam. This removal of atoms is best modelled by the linear cascade model. The linear cascade model consists of inelastic collisions that are counted as separate from each other and therefore considered as a linear sequence of collisions [37]. The model has revealed insight into the sputter yield, Y, which is defined as the number of a specific atom or ion emitted per primary ion. Figure 3.1.4 illustrate how a surface atom is emitted after a cascade of collisions starting with the implanted ion.

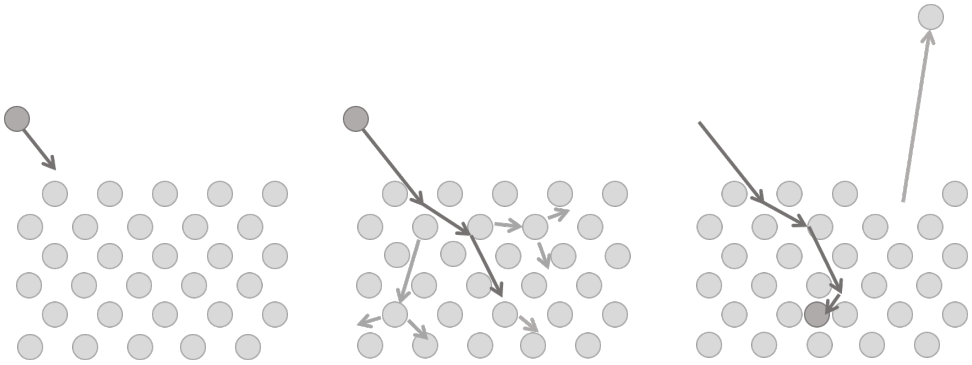

Figure 3.1.4: This figure illustrate the collision cascade model of sputtering, showing how a surface atom is emitted from the surface as a result of a series of collisions from the implanted ion.

An important parameter of sputtering is the sputter rate, SR, the number of atoms emitted from the surface per time. The sputter rate is assumed constant in a homogeneous solid when steady state sputtering conditions are reached. This condition is reached when the flux of implanted ions is in equilibrium with the removal of atoms. The timespan from the beginning of sputtering until steady state is reached is called the transient effect and this effect explains the variation in intensity in the beginning of the measurement. The transient effect's time scale is usually small compared to the time scale of the whole measurement and the effect is consequently neglected when the sputter rate is calculated from the crater depth.

The sputter rate in steady state is dependent on the surface binding energy, the energy required to break the bonds between an atom at the surface and the solid, and it is therefore strongly dependent on the chemistry and composition of the surface. That means that the sputter rate is different for every substrate. The chemistry of the surface can be changed by the presence of impurities and dopants, if the concentration is high enough, and the sputter rate might change.

The sputtering process change the composition of the substrate through for example recoil implanting. Recoil implantation is atoms in the solid being implanted to another position in the solid through collisions. Another example is cascade mixing, as illustrated in Figure 3.1.4, where the collisions in the solid might permanently displace atoms and change the structure. This might have bigger consequences in multicompositional substrates, like oxides, where the ratio between the metallic component and the oxide might change and alter the chemistry of the substrate.

Ionization

During the sputtering process a fraction of the sputtered atoms gets ionized. The secondary ion yield is the number of a specific atom that is ionized per emitted atom of the same type. The secondary ion yield can be considered as an ionization probability, γ. It is normally small, around one percent, with some exceptions when the emitted atom has a high electron affinity (relevant when using the Cs primary beam), or ionization potential (when the O_2 source is employed). The ionization of an emitted atom is complex and suitible models for the process are still not reported. The ionization is, as sputtering, dependent on the chemistry and structure of the surface. This means that the changes in the structure due to sputtering, as discussed above, also affect the secondary ion yield.

The are different models that explains different ways ionization of an emitted ion can occur. These

include the Local Thermal Equilibrium model, the Bond Breaking model, the Electron Tunnelling model, the Kinetic Emission model, the Band Structure model, the Work–function model, the Molecular model, the Surface Polarization model, the Perturbation model and the Surface Excitation model. The amount of different models illustrate in itself the complexity of the ionization. However, none of these models capture the process quantitatively and suitable for the conversion of SIMS intensity to concentration. The effect of the substrate, also called the matrix, on the secondary ion yield is called the matrix effect.

Secondary beam and Detectors

A fraction of the atoms that are sputtered from the surface are ionized. These ions then have to be transported to the detector. The ratio between the number of secondary ions that hit the detector and the secondary ions that are ionized close to the surface, is called the instrument's transmission function, T, and is determined by the instruments set-up. It is normally around 50 %. The emitted species from the sputtering are mostly single atoms or ions, but there may also be molecules. The goal of the secondary optics in SIMS is to separate the wanted analysed species from the other emitted species.

The first separation is done by an electrostatic sector analyser (ESA) which separates the high energy ions from the lower energy charged molecules and larger ions.The ESA end in a slit, the entrance slit, that only let through the ions with the desired energy. The secondary ions and molecules have a kinetic energy which decides their velocity, v_e. Their velocity makes them follow a path with the radius, r_e, because

$$F = qE \implies \frac{mv_e^2}{r_e} = qE, \tag{3.1}$$

which is the electrical field part of the Lorentz force. Since the electrical field is perpendicular to the trajectory and the force is a centrifugal force. The second separation is done by mass sector analyser (MSA) which again is utilizing the Lorentz force this time to separate the ions by their mass per charge ratio. The MSA also end in a slit, the exit slit, that only let through the masses that follow a path with radius, r_m, because

$$F = qv_mB \implies \frac{mv_m^2}{r_m} = qv_mB, \tag{3.2}$$

which is the magnetic field part of the Lorentz force if the magnetic field is perpendicular on the direction of the moving charge particle and the force acting on the particle then is a centrifugal force.

Figure 3.1.3 illustrate the secondary optics of the Cameca IMS-7f. It also shows the different detectors, the fluorescent screen used for alignment, the Faraday cup used for high intensity signals and the electron multiplier (EM) used for the low intensity signals that are of interest. The detection limit of SIMS is determined by the EM, which can count millions of ions per second. With the assumption that the ion's velocity does not change from the ESA to the MSA, Equation 3.1 and Equation 3.2 can be combined by putting $v_e = v_m$. The ions which satisfy

$$\frac{m}{q} = \frac{(r_m B)^2}{r_e E_0} \tag{3.3}$$

will then reach the detector. Both the electrical and the magnetic field can be changed to get the desired ion to the detector. The filtering of the ions can pick out the requested ion among a billion other ions.

Creating a depth profile

Combining the different factors presented above, one can convert the signal detected by the detector to concentration. The relationship between the intensity of the signal from the species, i, and the concentration of the species, $[i]$, can be expressed as

$$I_i = I_P Y \gamma_i T [i], \tag{3.4}$$

where Y, γ and T are the factors explained in the previous sections and I_P is the primary beam intensity. As discussed above the secondary ion yield is difficult to obtain and cannot be evaluated analytically. Therefore, a more practical relation between the intensity and the concentration are used replacing the constants with the sensitivity factor, $SF = (I_P Y \gamma_i T)^{-1}$. SF is extracted from experiment and the relationship is hence

$$[i] = \mathrm{SF} \left(\frac{I_i}{I_m} \right). \tag{3.5}$$

SF may not be constan when appying different measurement conditions, and the matrix intensity, I_m, is used to normalize the signal from each measurement. This might be included into the SF making it the RSF, the relative sensitivity factor. The RSF is found by integrating over the intensity, counts per second, versus time, second, for a reference sample with a known dose and then using the ratio between the integral and the dose to find the SF:

$$\mathrm{SF} = \frac{\delta}{\sum I_i(t) \frac{d}{C}} I_m. \tag{3.6}$$

Here δ is the known dose, C is the number of analytical cycles, t is the sputtering time, d is the crater depth and $I_i(t)$ counts per second at the time t.

The reference sample with a known dose used in the diffusion profile measurements in this work was the first measurement after the deuterium implantation. The matrix signal from this measurement was used as a reference to get the RSF. The matrix signal of a measurement was scaled to match the matrix signal of the reference, and the impurity signal was scaled in the same fashion.

A different solution was used for some samples, because of a varying matrix signal. At first ^{18}O was used as a matrix signal, but because of the abundance of oxygen in the atmosphere, it varied too much to be used as a reference signal. The next matrix signal problem was EM decay, a common problem with SIMS, which might have decreased the signal during the measurements. An advantage with these samples is that the implantation peak position is known at the relevant temperatures. The

peak was consequently used to take into accout any variation in the sputter rate and sensitivity in the measurement by moving the profile so that the peak was at the same height.

The conversion from measurement time to depth is done through the sputter rate, SR. The crater depth is measured after the SIMS measurement using a Dektak 8 stylus profiler and the SR is calculated from the sputtered time of the measurement. This is how the depth profiles are made.

Charge build-up

If the material is an insulator, or as in the case of β-Ga_2O_3 a semiconductor with a high band gap, a low conductivity of the sample may result in a charge build-up due to the positive charge from the primary ion beam. This may be particularly important for the as-implanted samples since the ion implantation increases the concentration of defects.

The most widely used method is to include an electron beam, which purpose is to add negatively charged electrons that can neutralize the positive charge built up by the primary beam. This means that the electron beam has to hit the sample in the same place as the primary ion beam. If the electron beam do not fix the problem, one can also deposit a layer of a metal on the surface of the sample, to increase the conductivity of the surface.

3.1.3 Fourier Transform-Infrared (FT-IR) spectroscopy

Infrared (IR) spectroscopy is a type of technique that is used to investigate the vibrational and electronic properties of a material. For example, how the quantized vibrational modes or phonons of a crystalline material absorb IR light. The highest frequency phonon modes will be modified by the insertion of a defect into the material. For a light element impurity, e.g. a hydrogen atom, the vibrational mode is localized primarily at the impurity and has a resonance frequency much higher than the frequencies of the lattice phonons, but still in the IR range. The ability to detect these localized vibrational modes (LVMs) makes IR spectroscopy an excellent technique to investigate hydrogen-relatived defects. The investigations are performed by exciting the vibrational modes with radiation. The wavelength of the absorbed radiation will function as an identification of the defect. This is how IR spectroscopy can be used to study defects in a crystal.

In this work, deuterium-related defects in β-Ga_2O_3 single crystals were investigated using Fourier Transform-Infrared (FT-IR) spectroscopy. Fourier transform spectroscometers use a Michelson interferometer to modulate the amplitude of light from a broad-spectrum light source. The prinsicle behind this technique is shown in Figure 3.1.5 for a monochromatic source. Light from the source is sent through a beam splitter, which reflects and transmits equal portions of the light to the fixed mirror M1 and moving mirror M2, respectively. The two beams recombine at the beam splitter, and the combined beam is sent to an infrared detector. When the optical path length difference, x, between the two beams is zero, the beams interfere constructively to yield a maximum signal on the dector. When x is equal to half the wave length of the source, $\lambda/2$, the beams interfere destructively and yield a zero signal on the detector. The modulated amplitude of light versus the optical pathlength difference between M1 and M2 is called an interferogram. The key to the FT technique is that the Fourier Transform of the interferogram yields a single channel spectrum which shows the amplitude and frequency of each contribution from the source.

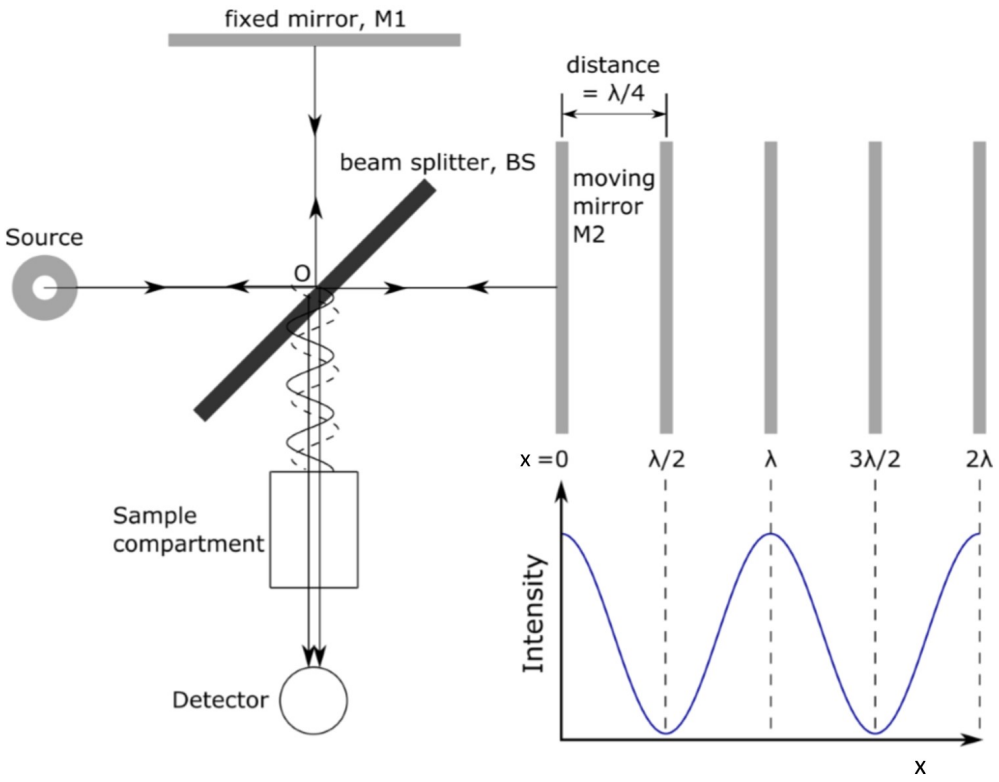

Figure 3.1.5: A simplified FTIR instrument set-up with a monochromatic source where a beam is sent through a beam splitter, and then towards a fixed mirror M1 in one direction and a moving mirror M2 in the other. The translation of M2 results in alternating constructive and deconstructive interference when the beams recombine. The signal is measured at the detector, and the x dependence is shown in the plot. Revised from Ref. [38].

The single channel spectrum signal is influenced by all the different elements in Figure 3.1.5, e. g., the source, the mirrors, the beam splitter, and the detector. The spectrum of the sample only is obtained by calculating the transmittance, T, spectrum, which is the ratio of the single channel spectrum with a sample in the beam path, $I(d)$, to the single channel spectrum obtained without a sample, I_0,

$$T = \frac{I(d)}{I_0} = \exp(-\alpha d), \tag{3.7}$$

In Equation 3.7, α is the linear absorption coefficient (absorption per unit length of the sample) and d is the length of the beam through the sample (which is equal to the sample thickness at normal incidence).

The vibrational lines due to deuterium defects bonded to oxygen atoms fall in the transparent spectral region of the host crystal, i. e., in the spectral region where the intensity of the light is altered by reflection losses only. If the reflectance of the sample is neglected the absorbance of the sample can be calculated using,

$$A = -\log(T) = -\log(\exp(-\alpha d)) = \alpha d \log(e). \tag{3.8}$$

The LVM of a defect in the material is observed typically as a peak in the absorbance spectrum. The wavenumber at which the peak is centered corresponds to the excitation of the vibrational mode from the ground state to the first excited state for that particular defect. According to the Beer-Lambert law, the absorbtion due to some species is linearly related to that species concentration. Although IR spectroscopy on its own cannot provide absolute quantification of a defect, the relative changes in the concentration of a defect can be investigated after, e. g., an annealing experiment at high temperature.

3.2 Density functional theory (DFT)

In this work density functional theory (DFT) is used to calculate the formation energy and migration energy of point defects in β-Ga_2O_3. Density functional theory is an ab initio method that uses only quantum physics and the Schrödinger Equation (SE) to do calculations on atomic systems. It is a powerful tool since calculations can be made to compare with experiments, without using empirical data.

This section contains information about Kohn-Sham DFT and different aspects of the DFT calculations such as convergence, functional choice and corrections. The section is mostly based on Ref.s [39] and [40].

3.2.1 Kohn-Sham Density Functional Theory

Density Functional Theory is founded on the two Hohenberg-Kohn theorems [41]. The first theorem states that all properties of a material can be found if n_0, the ground state electron density, is known. The minimum total electronic energy is the ground state energy, E_0, and the accompanying density is the ground state density, n_0. The second theorem states that this density can be found by minimizing the energy functional, $E[n]$, with respect to the density. This minimization is performed following a variational method [39][p.21].

Kohn-Sham DFT [42] approximates a solution of the many-body Schrödinger equation,

$$\hat{H}^{en}\Psi_\kappa^{en}(\{\mathbf{r},\mathbf{R}\}) = E_\kappa^{en}\Psi_\kappa^{en}(\{\mathbf{r},\mathbf{R}\}), \tag{3.9}$$

in order to find the ground state density of the system. The density is given by

$$n(\mathbf{r}) = \sum_j |\psi_j^{KS}(\mathbf{r})|^2. \tag{3.10}$$

$\psi(\mathbf{r})_j^{KS}$ is the Kohn-Sham wavefunction which is used in the Kohn-Sham SE, where the many-body SE is separated into single-electron equations:

$$\left(-\frac{\hbar^2\nabla^2}{2m_e} + V_{\text{eff}}(\mathbf{r})\right)\psi_\mathbf{k}^{KS}(\mathbf{r}) = \epsilon_\mathbf{k}\psi_\mathbf{k}^{KS}(\mathbf{r}), \tag{3.11}$$

with an effective potential, V_{eff}. The effective potential represents all interactions an electron has with the nuclei and other electrons in the system.

The total Kohn-Sham wavefunction is a linear combination of the eigenfunctions, $\psi_{\mathbf{k}}^{KS}$, which can be written as a Slater determinant, and hence, satisfies Pauli's exclusion principle by being antisymmetric upon electron exchange. The eigenfunctions are not periodic, but the electron density, $n(\mathbf{r})$, is periodic because of the periodicity of the crystal. The periodicity of the density is included in the eigenfunctions with a Bloch wave, $u_{\mathbf{k}}(\mathbf{r})$. The Bloch wave has the periodicity $u_{\mathbf{k}}(\mathbf{r}) = u_{\mathbf{k}}(\mathbf{r} + \mathbf{R})$ where $\mathbf{R}$ is linear combinations of the lattice vectors in real space, $\mathbf{R} = n_1\mathbf{a}_1 + n_2\mathbf{a}_2 + n_3\mathbf{a}_3$. The eigen function also have a plane wave part and the combined eigenfunction is:

$$\psi_{\mathbf{k}}^{KS}(\mathbf{r}) = A\exp(i\mathbf{k}\mathbf{r})u_{\mathbf{k}}(\mathbf{r}), \tag{3.12}$$

where A is a normalization factor and $\mathbf{k}$ is the wavenumber. An artificial periodicity is also given to the wavefunctions, to make calculations easier and to capture the finite size of a real crystal. The wavefunction's periodicity is given by $\psi_{\mathbf{k}}(\mathbf{r}) = \psi_{\mathbf{k}}(\mathbf{r} + \mathbf{L})$, where $\mathbf{L}$ is assumed to be big enough so it does not affect the energy of the system.

Because plane waves are the wavefunction of free electrons, they are not appropriate approximations to localized wavefunctions. The electrons situated close to the core are localized, hence are difficult to describe with plane waves. Instead a pseudo-potential is used to represent the core electrons, and the plane waves are used to model the valence electrons. In this work the projector augmented wave (PAW) method was used [43, 44]. The PAW method combines pseudo-potentials with the Linear Augmented Plane-Wave (LAPW) method.

Coming back to the calculation of the energy of the system, all the energy contributions of both the electron and nuclei from the many-body SE is given in the energy functional of the many-body system:

$$E^{en} = \underbrace{T_e}_{\substack{\text{kinetic energy}\\ \text{from electrons}}} + \underbrace{T_n}_{\substack{\text{kinetic energy}\\ \text{from nuclei}}} + \underbrace{U_{ee}}_{\substack{\text{energy from}\\ \text{electron-electron}\\ \text{interaction}}} + \underbrace{U_{nn}}_{\substack{\text{energy from}\\ \text{nuclei-nuclei}\\ \text{interaction}}} + \underbrace{U_{en}}_{\substack{\text{energy from}\\ \text{electron-nuclei}\\ \text{interaction}}}, \tag{3.13}$$

The Kohn-Sham approximation include the Born-Oppenheimer Approximation (BOA) which separate the many-body SE into an electronic SE and a nuclear SE [45]. The Born-Oppenheimer Approximation assume the nuclei to be fixed point charges because the mass of the nuclei are much larger than the electron mass, and the electron are assumed to move instantaneously when the nuclei moves. The electronic SE resulting from the BOA is simpler then the many-body SE. The kinetic energy of the nuclei is neglected and the interaction between the electron and the nuclei is included as an external time-independent potential, V_{en}. The energy functional, as a function of density, is hence simplified to

$$E[n] = T[n] + U_{ee}[n] + U_{en}[n], \tag{3.14}$$

where $U_{en}[n]$ is described as

$$U_{en}[n] = \int V_{en}(\mathbf{r})n(\mathbf{r})d\mathbf{r}. \tag{3.15}$$

To approximate the kinetic energy of the electrons, $T[n]$, a functional from the Hartree approximation is used, which assume that the electrons are independent:

$$T_s[n] = \sum_j \int \psi_j^{KS*} \frac{-\hbar^2\nabla^2}{2m} \psi_j^{KS} d\mathbf{r}. \tag{3.16}$$

Electrons in a crystal are not independent, therefore the kinetic energy from $T_s[n]$ is not totally correct. Another functional from the Hartree approximation is used to approximate the energy from electron-nuclei interactions, $U[n]$:

$$U_s[n] = \frac{1}{2} \int \int q^2 \frac{n(\mathbf{r})n(\mathbf{r}')}{|\mathbf{r} - \mathbf{r}'|} d\mathbf{r}\mathbf{r}' \tag{3.17}$$

The equation is only including the electrostatic energy from the repulsion between the electrons. Equation 3.17 allow the electron to interact with itself, and that is not physical. The error resulting from this assumption is called the self-interaction error. Due to this error, density functional theory have shortcomings when it models semiconductors and especially oxides. The self-interaction error might lead to both a smaller band gap and overly de-localized electrons.

The energy functional becomes the Kohn-Sham energy functional,

$$E[n(\psi)] = T_s[n] + U_s[n] + U_{en}[n] + E_{xc}[n], \tag{3.18}$$

if $T_s[n]$ and $U_s[n]$ is included and the difference between the approximations and the real functionals are put in another functional, the exchange-correlation functional,

$$E_{xc}[n] = (T[n] - T_s[n]) + (U[n] - U_{en}[n]). \tag{3.19}$$

The exchange energy is the quantum mechanical effect which give a repulsion between two identical particles, and the correlation energy is how much the movement of the other electrons are affecting the electron in question. This left-over energy functional is unknown, but by the help of the approximations the energy represented by the unknown functional is small. Including and approximating E_{xc} is the strength of the Kohn-Sham equations and the feature that make DFT calculations useful in material science.

3.2.2 The exchange-correlation functional

If the exact formulation for the exchange-correlation functional in DFT was found, the method would be an exact method, but the formulation of $E_{xc}[n]$ is not yet known. The simplest model for $E_{xc}[n]$ is based on the local density approximation (LDA), most often in combination with a homogeneous electron gas. The model use the local density, $n(\mathbf{r})$, at a point $\mathbf{r}$. The energy of the homogeneous electron gas with that density, $n(\mathbf{r})$, is calculated and the exchange energy and the correlation energy

of electrons in the gas is extracted. Hence, the energy from the gas, can be used as an approximation of the exchange-correlation energy in the point **r**. The generalized gradient approximation (GGA) use the gradient of the local density, $\nabla n(\mathbf{r})$, to approximate the exchange and correlation energy instead of simply $n(\mathbf{r})$. In this work we have used two different GGA functionals the Perdew–Burke-Ernzerhof (PBE) [46] and Perdew–Burke-Ernzerhof revised for solids (PBEsol) [47].

These simplest E_{xc} do not counteract the self-interaction error, but the hybrid functional that was used in this work, the Heyd-Sciseria-Ernzerhof (HSE) functional [48], counteract the self-interaction error by including a potential, in form of an energy functional, from the Hartree-Fock (HF) method. The HSE functional intermix exact HF exchange with correlation from other functionals, e.g., LDA or GGA like this:

$$E_{xc}[n] = aE_x^{\text{HF,SR}}(\omega) + (1+a)E_x^{\text{PBE,SR}}(\omega) + E_x^{\text{PBE,LR}} + E_c^{\text{PBE}}. \tag{3.20}$$

x and c denote exchange and correlation respectively, while SR means short range and LR means long range. The standard values for the mixing parameter a and the screening parameter ω are $a = 0.25$ and $\omega = 0.2$ and this is called HSE06. The screening parameter can be empirically adjusted for a certain semiconductor to get the same band gap as experiments. This empirical part of the HSE functionals make it questionable to refer to DFT calculations using the functionals as "ab initio". In addition, the inclusion of HF makes the calculation numerically slower than the simpler functionals. Hence, the importance of low computational cost and accuracy in energy must be compared when choosing which functional to use.

3.2.3 DFT calculations and convergence

The explanation of the DFT calculation process involves a circle argumentation, considering that V_{eff} is a function of the electron density. $n(\mathbf{r})$ is found by solving the Kohn-Sham SE to get the wave functions (Equation 3.10). But to solve the Kohn-Sham SE, V_{eff} has to be known. The solution is to use an iterative method. As Figure 3.2.1 illustrates the program's input is the position of the atoms. For crystalline materials, this input is a proposed unit cell. The program uses atomic potentials provided for each atom involved to calculate the first guess for $n(\mathbf{r})$.

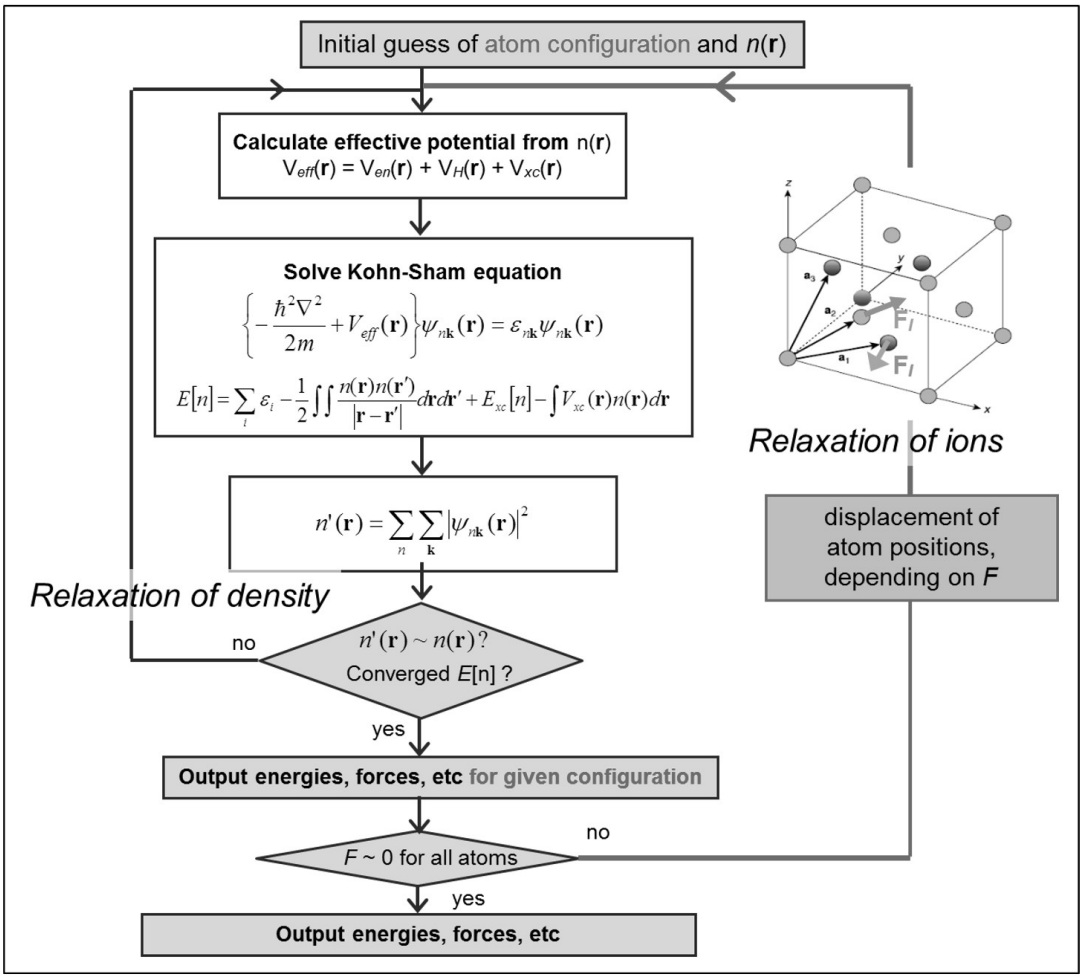

Figure 3.2.1: Flow chart of the self-consistent field calculation. Reprinted from Ref. [39]

The first guess for $n(\mathbf{r})$ is used to calculate a new electron density and this process is repeated, by varying the density, until the minimum energy is obtained, i.e the energy is converged. The energy is converged when the two last iterations give the same energy or, in numerical calculations, when a convergence condition, i.e. a minimum difference between these energies, are obtained. This numerical convergence condition is set as an input parameter. It is normally much smaller than the convergence condition for the total energy calculated in the end, and hence does not limit the accuracy of the total energy.

After the energy is converged, the forces between all the atoms in the unit cell are calculated. When the forces acting on the atoms are close to zero, depending on the set convergence criteria, the atoms are in their minimum energy position. Until then, the atoms are accordingly moved a small step in the direction of the force, and a new electron density is calculated. This continues until the atoms, volume of the unit cell and the electronic structure is relaxed, i.e. in the minimum energy state.

The DFT calculations, included in the process described in Figure 3.2.1, involve many integrals. In numerical calculations of infinite integrals, the integral limit cannot go to infinity. Therefore, the limit that is sufficient to get a converged result must be identified. This is done by performing convergence tests. The tests done in this work will be shown later in this section.

Integrals are used to calculate the total energy of all the occupied states in the system. The infinite number of states of a quantum system have increasing energies, but in DFT calculations the goal is to find the ground state of the system. Hence, the higher energy states are not relevant to the total energy because they are not occupied in the ground state. The highest energy state included in the calculations, the limit of the integral, is labelled by the cut-off **G**-vector. The kinetic energy of the $\mathbf{G}_{\text{cut-off}}$ is the energy cut-off, $E_{\text{cut-off}}$ and they are connected by $E_{\text{cut-off}} = \frac{\hbar^2}{2m} G^2_{\text{cut-off}}$. The height of this $E_{\text{cut-off}}$ is tested in the convergence tests, but also the **k**-point density. Because the integrals included in DFT are easier to perform numerically in reciprocal space, that is what is done in DFT. The reciprocal Kohn-Sham SE is

$$\sum_{\mathbf{G}'} \left(\frac{\hbar^2 (\mathbf{kG})^2}{2m_e} \delta_{\mathbf{GG}'} + V^{\text{eff}}_{\mathbf{G}-\mathbf{G}'} \right) u_{n\mathbf{k}+\mathbf{G}'} = \epsilon_{n\mathbf{k}} u_{n\mathbf{k}+\mathbf{G}}. \tag{3.21}$$

It involves a sum over linear combinations of the reciprocal lattice vectors, $\mathbf{G} = m_1\mathbf{b}_1 + m_2\mathbf{b}_2 + m_3\mathbf{b}_3$.

When an integral is solved numerically, it cannot be solved using an infinite number of points. The number of points in the sum representing the integral, are chosen to obtain converged results. With DFT calculations in practice, this is gone by choosing the **k**-point density in the first Brillouin zone. The first Brillouin zone represents the whole crystal in real space, because of the periodicity. The size of the **k**-point density is hence also investigated by convergence tests.

3.2.4 Calculating defect energies

When a point defect is inserted into the structure, the concentration will be much higher than in real crystals, if it is put into the unit cell and the unit cell is repeated periodically. Therefore a supercell is created by repeating the unit cell a couple of times in the lattice directions (see Figure 2.4.3). The size of the supercell can be increased to lower the concentration of the point defect, but this also increases the computational cost.

With affordable supercell sizes, the point defects interact with each other. This especially occur if the defects are charged. The concentration of defects is still a lot higher than the concentration in our experimental samples. There are different consequences of these interactions, one being that the energy of the defects create an energy band instead of an energy state when their wave functions overlap. This makes it difficult to calculate the formation energy in the dilute limit because it depends on the k-points the energy is calculated at. A solution to this is to calculate the energy at special k-points that have low symmetry. This is explained further in Ref. [49].

The formation energies of defects is calculated through

$$\Delta_f G_i = E_i^{\text{tot}} - E_{\text{bulk}}^{\text{tot}} - \sum_1^j \Delta n_j \mu_j + q\mu_e, \tag{3.22}$$

where E_i^{tot} is the total energy of the bulk without any defects, $E_{\text{bulk}}^{\text{tot}}$ is the total energy of the bulk with the defect under question, $\sum_1^j \Delta n_j \mu_j$ is the sum the chemical potential (see Equation 2.19) times the number of atoms that are inserted or removed of that type, j, and $q\epsilon_F$ is the charge of the defect times the Fermi level.

From Equation 3.22 one can construct diagrams showing how the formation energies of different defects changes with the Fermi level. The diagram reveals which charge states of the investigated specie have the lowest formation energy and will therefore be the most abundant specie. An example of the formation energy diagram is illustrated in Figure 3.2.2. The transition from one dominant charge state to another is named $\epsilon(q_i, q_j)$ and is marked in Figure 3.2.2.

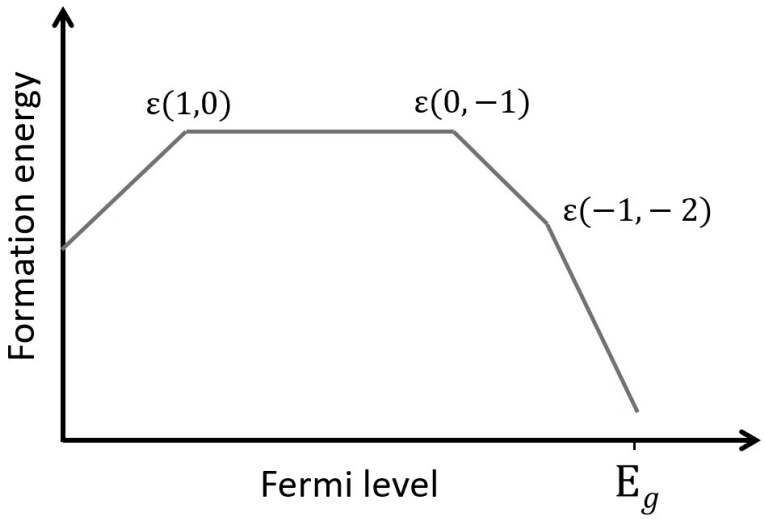

Figure 3.2.2: An example of the dependence of the formation energy with the Fermi level. It also shows which charge states that have the lowest formation energy at different Fermi levels and where the transition from one charge state to the other happens.

The formation energy of defects are dependent on both the atmospheric conditions and the Fermi level (see Equation 3.22). To calculate the formation energy of a defect, the energy of a defect-free supercell is compared with the energy of the supercell with the defect. In this work we have looked at three types of defects; the gallium vacancy, the hydrogen interstitial and complexes between the two preceding defects. The atmospheric conditions of the systems have two limiting conditions; oxygen rich and oxygen poor (gallium rich). A real system is normally in between these two, but it is difficult to know exactly what the atmospheric conditions of the experiments are. Therefore, the two limiting conditions, are used to see the variance in formation energies with atmospheric conditions. The chemical potential for the different species are hence in between the two limiting conditions and presented in Table 3.1.

Table 3.1: The chemical potential of the three different species involved, for the two limiting atmospheric conditions oxygen rich and oxygen poor/gallium rich.

μ_i	O-rich:	Ga-rich:
μ_O	$\frac{1}{2}E_{tot}(O_2)$	$\frac{1}{2}E_{tot}(O_2) + \frac{1}{3}\Delta H_f Ga_2O_3$
μ_{Ga}	$E_{tot}(Ga) + \frac{1}{2}\Delta H_f^{Ga_2O_3}$	$E_{tot}(Ga)$
μ_H	$\frac{1}{2}E_{tot}(H_2) + \frac{1}{2}\Delta H_f^{H_2O}$	$\frac{1}{2}E_{tot}(H_2)$

From Equation 3.22 the formation energy of the defects in this work can be calculated. Two examples are given here. The formation energy of the fully ionized gallium vacancy is then

$$E^f[V_{Ga}^{-3}] = E_{tot}[V_{Ga}^{-3}] - E_{tot}[Ga_2O_3] + \mu_{Ga} - 3\epsilon_F, \tag{3.23}$$

and the formation energy of the complex between the gallium vacancy and an interstitial hydrogen is

$$E^f[(V_{Ga}H)^{-2}] = E_{tot}[(V_{Ga}H)^{-2}] - E_{tot}[Ga_2O_3] + \mu_{Ga} + \frac{1}{2}\mu_{H_2} - 2\epsilon_F. \tag{3.24}$$

The point defects mentioned above are all charged defects. Even though the defect is inserted into a supercell, the electrostatic potential of the defects decay slowly. The defects in the periodically repeated supercells will, for instance, be affected by the electrostatic potential of the neighbouring defects. The interactions between point defects in supercells are more thoroughly elaborated in Ref. [8]. The interactions between point defects was attempted to be corrected in this work, to emulate the situation where the defect concentration is dilute. $E_{tot}[i]$ is therefore

$$E_{tot}[i] = E_{\text{from calculation}}[i] + E_{FVN}[i] \tag{3.25}$$

for the supercells with a charged defect. $E_{FNV}[i]$ is a correction energy when using the Freysoldt, Neugebauer, and Van de Walle (FNV) method [50, 51].

3.2.5 Nudged Elastic Band (NEB) method

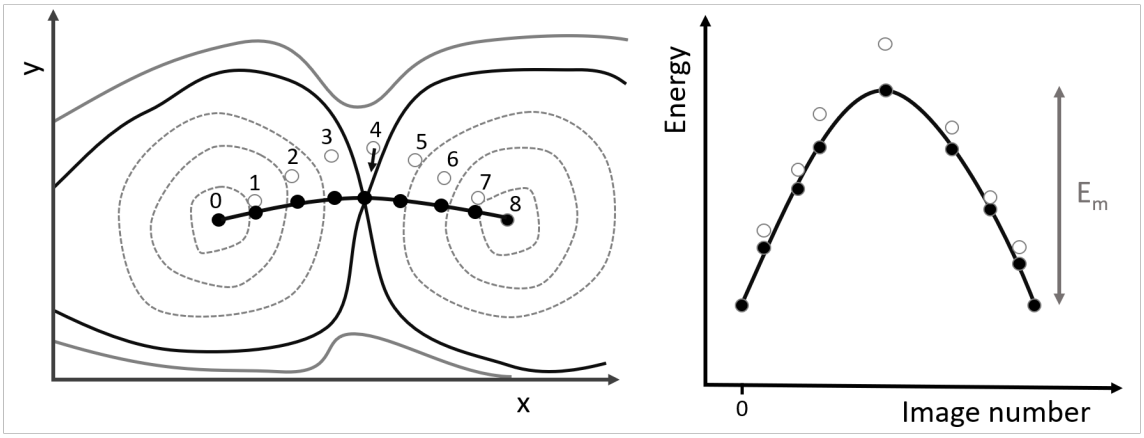

Figure 3.2.3: To the left: A potential energy map around two energy minima in the structure. The transition state is the crossing point between the two black lines. The gray line has higher energy than the black line and the dotted lines have lower energy. The white dots represent the proposed path from one minima to the other. The black dots show the converged images laying on the MEP. The arrow illustrate the force acting on the fourth image that is orthogonal to the path. This force will lead the images toward the MEP. To the right: The energy of the proposed images (white dots) and the converged images (black dots) are plotted with the energy of the MEP (line). Revised from Ref. [40]

DFT was also used to calculate the migration energy of deuterium in β-Ga_2O_3 and evaluate the minimum energy path (MEP) in the two orientations investigated in this work. This was done with the Nudged Elastic Band (NEB) method [52, 53]. This method is used to find the minimum energy path between two local minima in the structure. It is executed by proposing a minimum energy path between two sites. Figure 3.2.3 shows a potential energy map around two energy minima in the structure. The white dots represent the proposed path from one energy minima to the other. Each dot represents an "image". The image represents a semi-seperate DFT calculation which calculates the energy and forces of the structure with the migrating species in that position. The images are spread out in a path between the positions of the minima, with a fixed image in each minimum. Each of these images goes through a relaxation with DFT, but there are fictitious springs in between the images hindering them all from ending up in local minimum.

The force acting on all the images from the gradient in potential energy can be separated into a force perpendicular to the proposed MEP, and a force orthogonal to the MEP. If all the images lay on the MEP, their orthogonal forces are zero. The NEB method therefore move the images in the direction of their orthogonal force during the relaxation. The perpendicular force is determined by the spring constant of the fictitious spring and the gradient of the potential energy. This force is used to keep the images on evenly separated, but should not push the images away from the MEP.

In combination with the NEB method we used the climbing image method [54] in this work. This was used together with NEB to make sure that the transition state, the maximum energy on the MEP, is captured by an image when all images are converged.

For each image between the two minima an ionic relaxation is required, and this has a high computational cost. Therefore all NEB calculations were performed using the PBEsol functional, and not at the HSE level. The HSE functional was used afterwards to calculate the energy of the PBEsol relaxed structure of the minimum and the transition states, to extract migration energies both at the HSE and PBEsol levels.

3.2.6 Computational details

In this work, the computer program Vienna Ab initio Simulation Package (VASP) was used to perform DFT calculations. The defect energy calculations were performed using a supercell consisting of $1 \times 3 \times 2$ unit cells resulting in 120 atoms. The unit cell used to make the supercell for the defecet calculations was volume, ion and electronically relaxed with HSE screened hybrid exchange-correlation functional with a fixed screening parameter of 0.2 $Å^{-1}$ and a Hartree-Fock mixing parameter of 0.35. The lattice parameters were converged to $\pm 10^{-2}$ Å which required $E_{cut-off} = 600$ eV and a k-point density of 2 $Å^3$ selected by Monkhorst-Pack grids [55]. This was more than enough to converge the electronic structure, as the convergence tests presented later show.

The same $E_{cut-off}$ and k-point density were used to relax the unit cell which made up the supercell for the NEB calculations except that the PBEsol functional was employed. Ideally, a convergence test of the necessary supercell size should have been performed as well, but this was not done and the supercell size was also the same, to simplify the execution. The number of images used was either seven or nine for each calculation, and will be specified in the result together with the resulting migration energy. The convergence criteria used in the relaxation was that the maximum force on any atom in the structure is lower than 0.04 eV/Å. For some calculations, this was not possible to

satisfy for all the images, but it was satisfied for the image representing the transition state, if not specifically specified in the results. The calculations used standard parameters for the spring constant and engaged the climbing image method.

The defect formation energy calculations used HSE functionals and the migration calculations with the NEB method used PBEsol functionals. These calculations result in relative energies. All relative energies were converged to $\pm 10^{-2}$ eV per formula unit (f.u.) which required $E_{cut-off} = 400$ eV and a special k-point, k $= 0.25 \times 0.25 \times 0.25$. These parameters were also used in a one-shot self-consistent field (SCF) calculation of the defect-free supercell, since the total energy of this supercell was used to find the defect formation energies. Furthermore, all total energies involved in the chemical potential were converged to $\pm 10^{-2}$ eV per f.u. as well. The convergence tests resulting in the required parameters listed here are presented in the next section.

Convergence tests

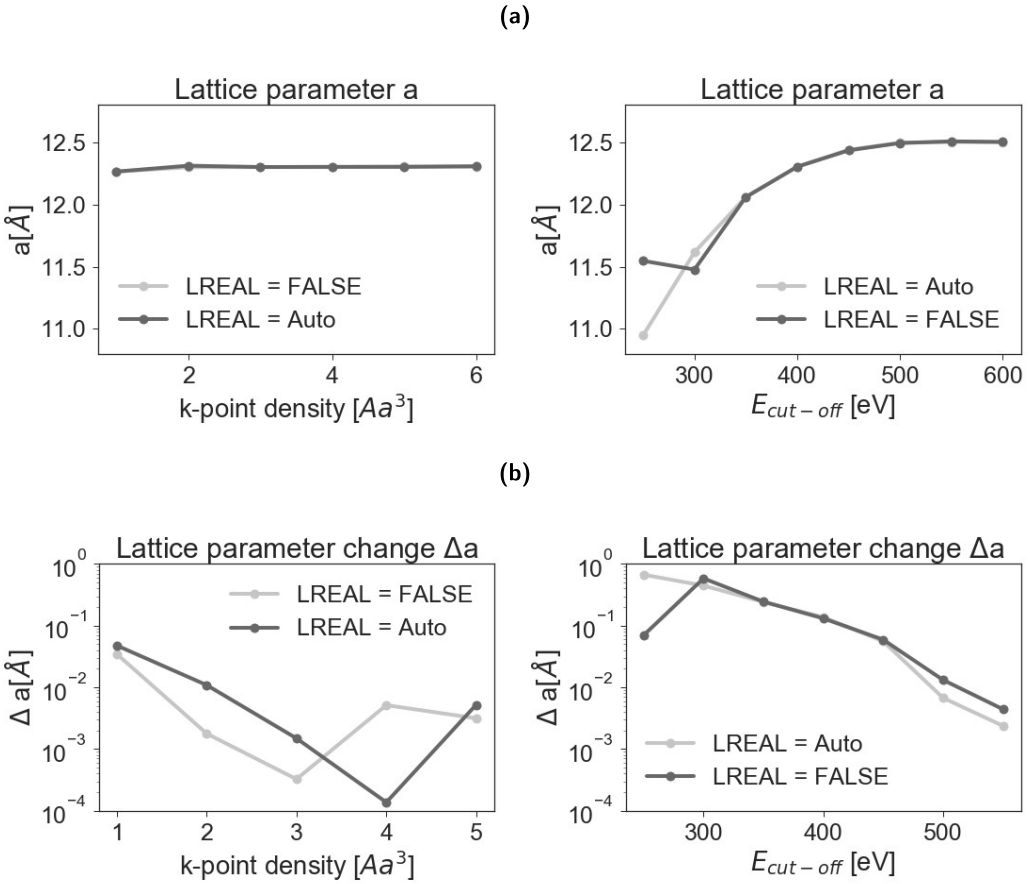

Figure 3.2.4: (a) Convergence tests for the lattice parameter a. (b)Chance in a with either k-point density or $E_{cut-off}$. The same was done with the other lattice parameters, b,c, and β (see Appendix E). All calculations were done with both LREAL=Auto and LREAL=FALSE.

A converged result is defined by the requested accuracy of the result. The accuracy can be chosen based on the computational cost of calculations and the accuracy of the experimental data the results are compared to. The convergence of total energies from DFT calculations are slower than relative

energies, e.g. the difference between a structure with and without a defect. The total energies are not as interesting as the relative energies however, since they do not represent a real physical value. This is a consequence of the use of Kohn-Sham wavefunctions.

The k-point density and energy cut-off were investigated using the PBE exchange-correlation functional. A unit cell was relaxed with different values of k-point density and energy cut-off and the convergence of lattice parameters were investigated. Figure 3.2.4 shows the convergence of lattice parameter a. The unit cell volume and ions were relaxed using the k-point density or the energy cut-off shown in the plot. For the energy cut-off series a k-point density of 4 Å^3 was used and for the k-point density series an energy cut-off at 400 eV was used. Figure 3.2.4b shows the change in length of a from either k_{dens} to $k_{\text{dens}} + 1$ or the $E_{\text{cut-off}}$ to $E_{\text{cut-off}} + 50$. The same was done with the other lattice parameters, b,c, and β (see Appendix E).

The conclusions drawn from the convergence tests of the lattice parameters has already been presented. The lattice parameters can be seen in Table 3.2, which also compare them with other DFT calculations and experimental values. Both the lattice parameters for the HSE relaxed unit cell and the PBEsol relaxed unit cell is included. The lattice parameters of the PBEsol relaxed unit cell are not as similar to the experimental parameters as the HSE relaxed unit cell, which in turn match very well.

Table 3.2: A list of the lattice parameters, a, b, c, β, the band gap, E_g, and the enthalpy of formation, ΔH_f, from this work's DFT calculations compared with with Varley et al's [29] and experimental values [24]. Varley et al used both 35 % HF and 25 % HF (HSE06), and found the lattice parameters to be the same for both [29]. The lattice parameters of the PBEsol relaxed unit cell used in the NEB calculations are also included.

	This work		[29]	Experiment
	HSE (35% HF)	PBEsol	HSE06	Experiment
a [Å]	12.24	12.34	12.05	12.23
b [Å]	3.04	3.07	3.05	3.04
c [Å]	5.80	5.87	5.84	5.80
β [°]	103.76	103.76	103.9	103.7
E_g [eV]	4.97	-	4.87	4.9
ΔH_f [eV]	-10.33	-	-10.40	-11.29

Table 3.2 also shows the band gap and the enthalpy of formation of β-Ga_2O_3. The convergence of these values was investigated as well. Figure 3.2.5 shows the result of the convergence tests of the total energy. Figure 3.2.5b shows how the total energy change from either k_{dens} to $k_{\text{dens}} + 1$ or the $E_{\text{cut-off}}$ to $E_{\text{cut-off}} + 50$. The same was done with the band gap, the force and the pressure. The conclusion was that a k-point density at 2 Å^3 and an energy cut-off at 400 eV is sufficient to converge relative energies, as presented above. The Monkhorst-Pack mesh with a k-point density of 2 Å^3 was replaced with the special k-point because of a faster convergence and the other advantages that a special k-point has.

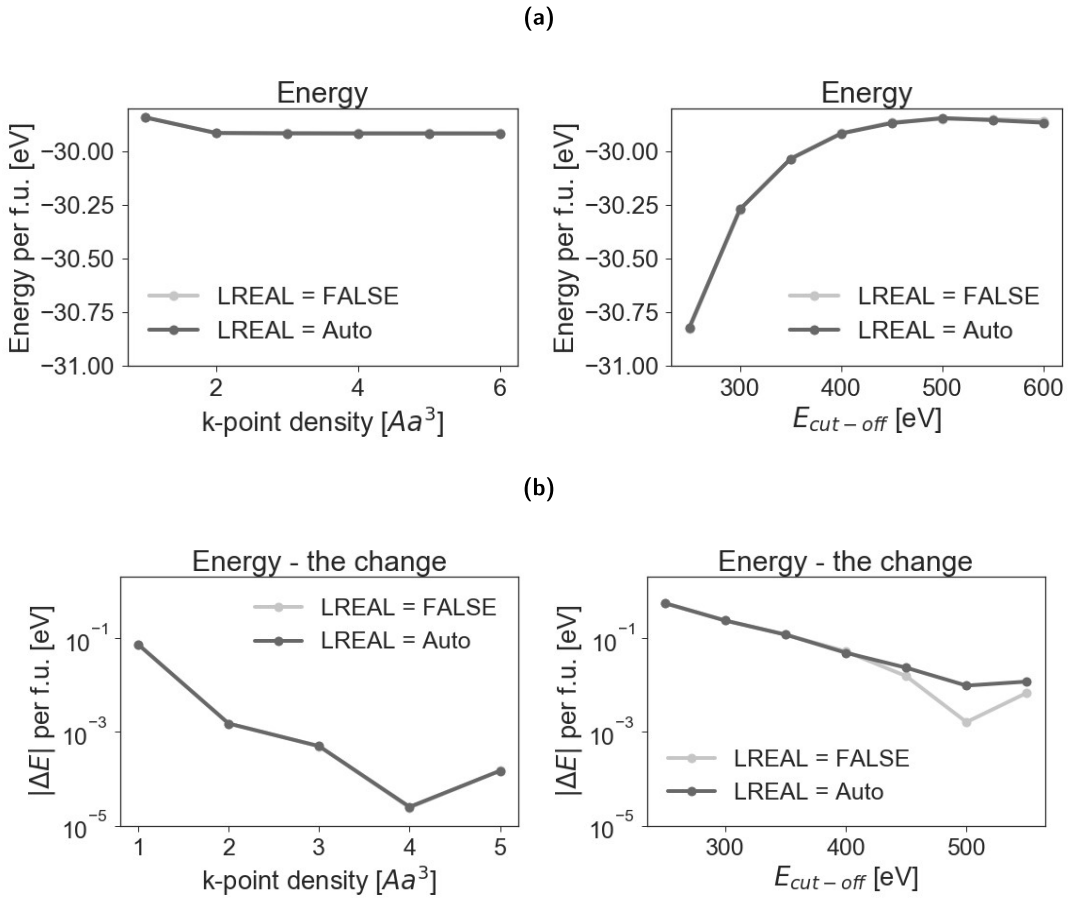

Figure 3.2.5: (a) shows the result of the convergence tests of the total energy. (b) shows how the total energy change from either k_{dens} to $k_{\text{dens}}+1$ or the $E_{\text{cut-off}}$ to $E_{\text{cut-off}}+50$. The same was done with the band gap, the pressure and the force.

Chemical potential

The chemical potential of a species is involved in the formation energy of a defect, as shown in Equation 3.22. The chemical potential of the three different species involved in this work's investigated defects were calculated for the two limiting atmospheric conditions oxygen rich and oxygen poor/gallium rich and are listed in Table 3.3.

Table 3.3: The chemical potential of the three different species involved were calculated for the two limiting atmospheric conditions oxygen rich and oxygen poor/gallium rich and are listed here.

μ_i	O-rich:		Ga-rich:	
μ_O	$\frac{1}{2}E_{tot}(O_2) =$	-7.84 eV	$\frac{1}{2}E_{tot}(O_2) + \frac{1}{3}\Delta H_f Ga_2O_3 =$	-11.28 eV
μ_{Ga}	$E_{tot}(Ga) + \frac{1}{2}\Delta H_f^{Ga_2O_3} =$	-8.78 eV	$E_{tot}(Ga) =$	-3.62 eV
μ_H	$\frac{1}{2}E_{tot}(H_2) + \frac{1}{2}\Delta H_f^{H_2O} =$	-5.48 eV	$\frac{1}{2}E_{tot}(H_2) =$	-4.13 eV

The total energies required to calculate the chemical potential were calculated and are listed in Table

3.4. The energies are given in total energy per f.u. The enthalpy of formation, ΔH_f, of H_2O and β-Ga_2O_3 were calculated by comparing the energy of the combined species with the isolated species.

Table 3.4: The total energy per f.u., calculated with DFT, of the different species involved. The enthalpy of formation of H_2O and β-Ga_2O_3 were calculated by comparing the energy of the combined species with the isolated species.

i:	E^i_{tot} [eV]:	ΔH^i_f [eV]:
Ga_2O_3:	-41.07	-10.33
O_2:	-15.67	
H_2:	-8.26	
Ga:	-3.62	
H_2O:	-18.79	-2.70

3.3 Diffusion modelling

In this work, experimental diffusion profiles were compared with profiles from diffusion models with the aid of programs written in python and the partial differential equation solver flexPDE [56]. The three models used in this work is the semi-infinite source model, a diffusion length test and the trap limited diffusion model. In order to compare experimental profiles with profiles from the semi-infinite source model self-written python programs were used. They were also used to find the diffusivity through the diffusion length. In the first case, D and c_S were changed until there was an overlap between the experimental profile and the simulated profile. For the latter case, the diffusion length was extracted from the profiles and the diffusivity was derived from that.

The trap limited diffusion model however, does not use a solution of the diffusion equation, but a modulation of the equation itself. Consequently the differential equation have to be solved numerically. The flexPDE program solves the equation:

$$\frac{\partial[^2\mathrm{H}]}{\partial t} = D_{^2\mathrm{H}}\frac{\partial^2}{\partial x^2}[^2\mathrm{H}]_{SS} - \frac{\partial[tr_f]}{\partial t}, \tag{3.26}$$

where

$$\frac{\partial[tr_f]}{\partial t} = \kappa[^2\mathrm{H}]_{SS}[tr_e] - \nu[tr_f]. \tag{3.27}$$

The syntax has been changed from the presentation in the theory so $[tr_S H_i] = [tr_f]$, the concentration of filled traps, and $[tr_S] = [tr_e]$, the concentration of empty traps, because of the trap is unknown. The relation between these two concentrations is:

$$[tr_{tot}] = [tr_e] + [tr_f], \tag{3.28}$$

where $[tr_{tot}]$ is the total trap concentration, which is constant in time and depth. In addition, the SS model is included because the deuterium is implanted into the sample. $[^2\mathrm{H}]_{SS}$ is hence given by:

$$[^2\mathrm{H}]_{SS} = \frac{[^2\mathrm{H}] \cdot SS}{[^2\mathrm{H}] + SS}. \tag{3.29}$$

Figure 3.3.1 shows how the different variables behave during a simulation of the diffusion profile. The initial conditions of the calculations is that $[^2\mathrm{H}_{\text{not in trap}}]$ is the previous experimental curve, $[tr_f] = 1 \cdot 10^{13}$ cm^{-3} in the very first calculation step and afterwards given by Equation 3.27 and the initial condition of $[tr_e]$ is determined by Equation 3.28. Furthermore, the specified boundary conditions of the calculations are that $[^2\mathrm{H}_{tot}] = c_0$, which is the concentration at $x = 1$ μm and that $[^2\mathrm{H}_{tot}] = 1 \cdot 10^{15}$ cm^{-3} far away from the surface. The other parameters have the default boundary condition of flexPDE, that the flux at the boundaries is zero.

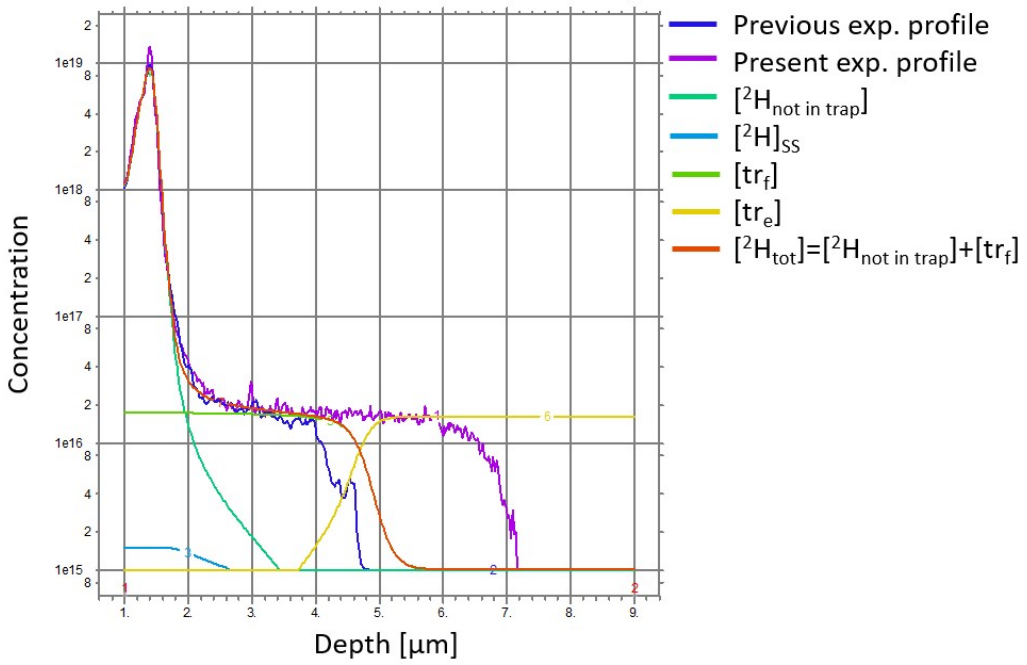

Figure 3.3.1: An example of the diffusion profile simulations performed with flexPDE [56]. All variables are shown together and marked by color.

Figure 3.3.1 depict the simulation in the start of the time range, where the shoulder of $[^2\mathrm{H}_{tot}]$ is moving towards the experimental profile's depth. The filling of the empty traps is observed by the cross over between the red and the yellow line. Also, the fraction of deuterium being released from the implantation peak is shown in the example.

The diffusion modelling process is demonstrated through the flowchart in Figure 3.3.2. The flowchart shows how some of the parameters are fixed and some are fitting parameters. As the last check in the flowchart implies, the credibility of the fitting parameters D and ν lays in if their prefactors, i.e. that D_0 and ν_0 result in physically meaningful values. This is an important point since these parameters are the output from the modelling.

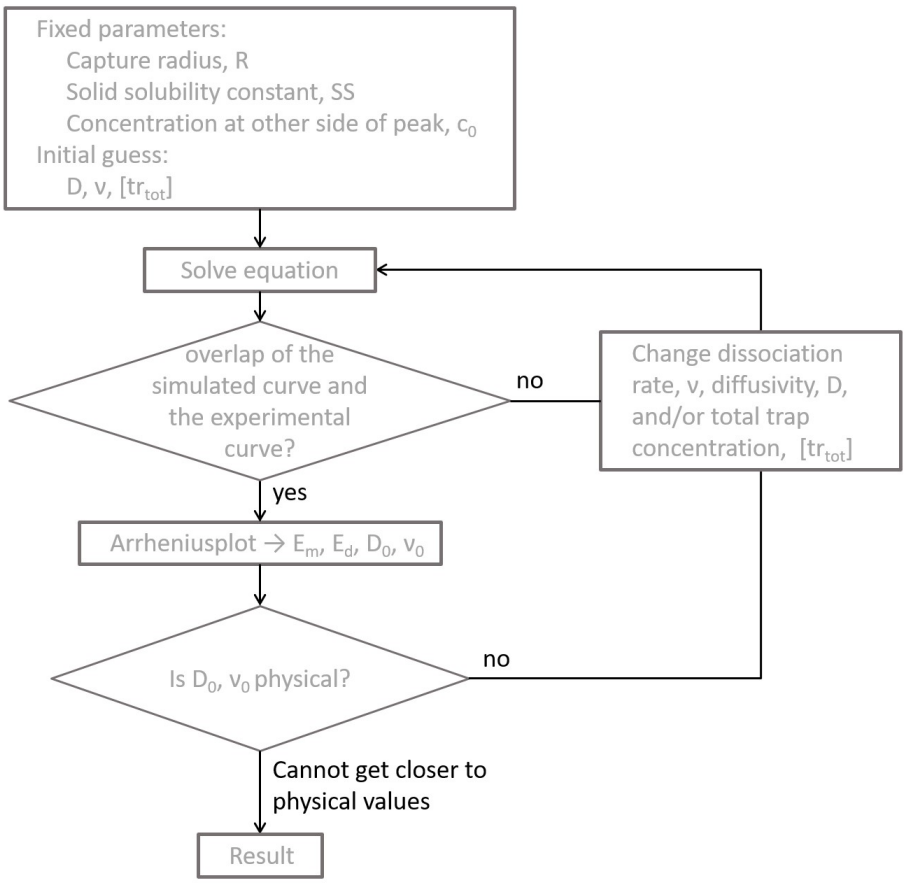

Figure 3.3.2: Flowchart illustrating the process of simulating diffusion through the TLD model.

3.3.1 The parameters of the TLD model

This TLD model involve many parameters, both fixed and fitting parameters. This section will explain the choice of the value for the fixed parameters and present what has been referred to as physical prefactors.

Solid solubility

The solubility model (Equation 3.29) can be used when the experimental data shows a peak in the concentration, the implantation peak, where the implanted species are not moving. The model simulates that only a fraction of the atoms in the peak are free to move. The solid solubility constant, SS was set to $1.5 \cdot 10^{15}$ cm^{-3} for the simulations of the (-201) orientation and had to be increased to $1.5 \cdot 10^{16}$ cm^{-3} for the (010) orientation. The first value was chosen because it is around the limit of detection for the SIMS, but the necessary increase indicate that the constant have an additional numerical function. It serves to keep the curve for the non-trapped deuterium derivable because if it is too low, the curve is too abrupt for flexPDE to calculate the derivative numerically. This solubility limitation of the diffusion could have been modelled in many different ways, and one could make a revaluation of the model.

Trapping rate and the capture radius

The trapping rate is given by

$$\kappa = 4\pi R D_{2\mathrm{H}}, \tag{3.30}$$

and comes from an analysis of bimolecular reaction rates in solids [57]. The case of long range forces are used because interstitial deuterium is assumed to be positively charged. Long range coloumbic interactions are hence an effect of the charged diffusing specie. The trapping rate, κ, involves an important parameter, the effective capture radius, R. This parameter influences the probability of a diffusing specie being trapped. The capture radius used in these calculations is set to be the approximate inter atomic distance in the structure so $R = 5$Å. This should be an appropriate choice because usually most of the interactions between point defects in a structure occur between nearest neighbours. However, if the deuterium and the trap have opposite charge, the effective capture radius could be larger due to attractive coloumbic interactions. Even if that is the case, the approximate interatomic distance is a starting point and can be revaluated if needed.

Total number of traps

In the ideal case, one already knows the point defect acting as a trap when using the trap limited diffusion model. Unfortunately, this is not the case in the present situation and this implies that in addition to the two main fitting parameters the dissociation rate, ν, and the diffusivity, D, we also have to treat the total number of traps, $[tr_{tot}]$, as a fitting parameter. This parameter would be easy to fit if the concentration of the trap is constant laterally on the sample, as for deuterium diffusion in ZnO [19]. In such a situation, a value for $[tr_{tot}]$ that fits for all the diffusion profiles could be identified and $[tr_{tot}]$ could be held fixed for all the simulations. This is not the case in the simulations in this work, which will be revealed later.

Dissociation rate and its physical prefactor

The dissociation rate is given by $\nu = \Gamma_0 \exp\left(\frac{\Delta S_{vibr}}{k_B}\right) \exp\left(-\frac{E_a}{k_B T}\right) = \nu_0 \exp\left(-\frac{E_d}{k_B T}\right)$. Γ_0 is the attempt frequency of the dopant dissociating from the trap, and it is assumed to be the same as the prefactor of the jump frequency (Equation 2.23). The dissociation rate can, like the diffusivity, be plotted in an Arrhenius plot and give a strait line. The activation energy found from the slope of the plot is thus the dissociation energy, E_d. The prefactor of the dissociation rate, ν_0, is assumed to be around the phonon frequency of the lattice, $\omega_0 = \Gamma_D \simeq 10^{13}$, since the change in entropy is assumed to be close to zero making $\exp\left(\frac{S}{k}\right) \approx 1$. The prefactor is therefore physical if it is close to 10^{13} s^{-1} and there is no change in the vibrational entropy.

A physical prefactor for the diffusivity

The prefactor for the diffusivity is given by $D_0 = \beta a^2 f \omega_0 \exp\left(\frac{S}{k}\right)$. A physical value for D_0 is evaluated by making some assumptions. The change in entropy assumed to be small so $\exp\left(\frac{S}{k}\right) \approx 1$ and the correlation factor, f, is assumed to be close to unity. Furthermore, the jump distance, $\lambda = \sqrt{\beta} a$, at least in (010) oriented β-Ga_2O_3, is approximately 3 Å and the attempt frequency, ω_0, is assumed to be around the phonon frequency of the lattice which is 10^{13} s^{-1}. A physical prefactor is then

$$D_0 \approx \left(3 \cdot 10^{-8}\right)^2 \mathrm{cm}^2 \cdot 1 \cdot 10^{13} \mathrm{s}^{-1} \cdot 1 = 9 \cdot 10^{-3} \mathrm{cm}^2 \mathrm{s}^{-1} \approx 10^{-2} \mathrm{cm}^2 \mathrm{s}^{-1}.$$

The prefactor could deviate from these assumptions and still be physical. There could for example be a small change in the vibrational entropy if the path of the deuterium is complex, and the distance can also be larger in the (-201) oriented β-Ga_2O_3. The prefactor's dependence of these two parameters are shown in Figure 3.3.3, to illustrate especially that a very small ΔS_{vibr} can make a big change in D_0.

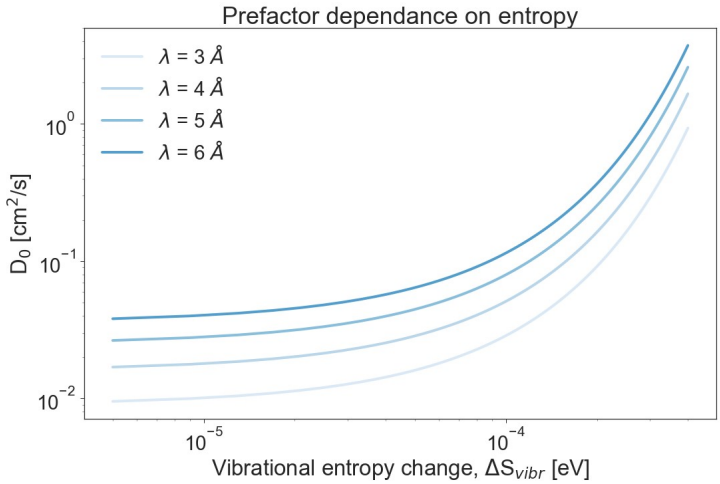

Figure 3.3.3: The prefactor's dependence of a change in entropy is shown to illustrate that only a small change is necessary to get a prefactor around 10^0 cm^2/s. The prefactor also increase with the jump length, λ. Here the rest of the assumption from the former discussion of the prefactor is upheld.

3.3.2 Combination of two approaches to determine diffusion mechanism

From a successful diffusion modelling with the TLD model, the migration energy and the dissociation energy are derived. Fortunately, the same energies can be calculated with density functional theory. This give the opportunity to compare the theoretical values with the experimental values, or more precisely the values gained from experimental data through mathematical diffusion models. If the values are compatible, a verification of both approaches is obtained and the results are more reliable. This comparison will be carried out after the result from the diffusion modelling and the density functional theory is presented.

Chapter 4

Results and Discussion

In this chapter the results from the experimental investigations, diffuison modelling will be presented and discussed. The procedure of the investigation of deuterium diffusion in β-Ga_2O_3 is presented first. Next, the SIMS profiles measured after deuterium implantation and subsequent heat treatment series is shown. Thereafter, different models for diffusion are compared with the experimental data, resulting in activation energies for the diffusion. In addition, the results of the FT-IR measurements are presented. Following that, the results from the DFT calculations including formation energies of point defects in β-Ga_2O_3, migration energies of and migration paths for hydrogen in β-Ga_2O_3 are presented. At last, the results from the different approaches are discussed together to reveal a better insight into hydrogen/deuterium diffusion in β-Ga_2O_3.

4.1 Procedure

Sn-doped edge-defined film fed grown samples of β-Ga_2O_3, from Tamura Corporation, cut into the two orientations (010) and (-201) were first implanted with deuterium using two different implantation energies resulting in implantation peaks with $R_P \sim 1.5\mu$m and $R_P \sim 8\mu$m. After implantation the samples were annealed in ambient conditions at the lowest temperature possible to repair the damage from the ion implantation so that they became sufficiently conductive to be measured with Secondary Ion Mass Spectrometry (SIMS). This temperature turned out to be 300 °C for the doped samples.

After this, the samples were measured in SIMS to produce the closest we could get to a reference, "as implanted", concentration versus depth profile. Next, the samples were heat treated in ambient conditions in an annealing series. Suitible temperature steps and time spans for the annealing series were chosen to get well-defined diffusion profiles to compare with simulations and as many points as possible in the resulting Arrhenius plots. In between the heat treatments, the samples were measured with SIMS. This produced a series of diffusion profiles that could be simulated with flexPDE and python using different diffusion models with a main emphasis on the trap limited diffusion model. However, when the undoped samples of β-Ga_2O_3 were measured charge build-up disrupted the SIMS measurements and accurate depth profiles were not obtained for the majority of the temperature steps.

The samples used in this work have different doping and different orientations. They have also been implanted in different ways with varying doses and implantation energies. Table 4.1 list the different

samples with specifications of orientation, doping and implantation.

Table 4.1: The different samples with specifications of orientation, doping and projected range of implantation. * indicate that the same sample was implanted again. After the second implant the sample name get the additional _2.

Sample name	Orientation	Doping	R_P of implantation	Dose [cm^2]
A1	-201	Unintentionally doped	1.5 μm	$4 \cdot 10^{15}$
B1	-201	Sn-doped	1.5 μm	$5 \cdot 10^{14}$
C1	-201	Sn-doped	1.5 μm	$5 \cdot 10^{14}$
D1	-201	Unintentionally doped	1.5 μm	$4 \cdot 10^{15}$
E1	-201	Sn-doped	8.0 μm	$2 \cdot 10^{15}$
A2	010	Unintentionally doped	1.5 μm	$4 \cdot 10^{15}$
B2	010	Sn-doped	1.5 μm	$5 \cdot 10^{14}$
C2	010	Sn-doped	1.5 μm	$5 \cdot 10^{14}$
D2	010	Unintentoinally doped	1.5 μm	$4 \cdot 10^{15}$
B2_2*	010	Sn-doped	8.0 μm	$2 \cdot 10^{15}$
C2_2*	010	Sn-doped	8.0 μm	$2 \cdot 10^{15}$

Figure 4.1.1 a) reveals how the energy of the implanted ions affect the depth of the implanted profile simulated using SRIM [34]. Additionally, Figure 4.1.1 b) shows the damage made by the implantation through the created vacancies. The SRIM software simulates collisions in the sample, but only a fraction of these collisions results in a vacancy being created. Figure 4.1.1 b) shows two different values of the fraction.

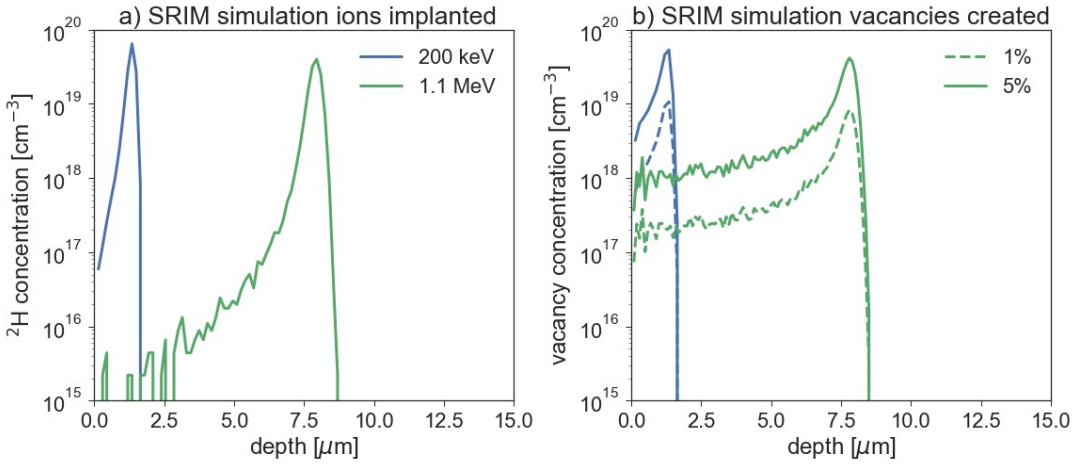

Figure 4.1.1: Simulations of ion implantation made by Ref. [34]. a) shallow implant of deuterium with implantation energy = 200 keV and a deep implant of deuterium with implantation energy = 1.1 MeV. b) the damage made by the two different implantations showing how the implantation induces vacancies between the surface and the implantation peak. In addition, two different probabilities of vacancy survival after a collision is illustrated.

Unintentionally doped samples with a lower free carrier absorption compared to the doped samples were measured with Fourier Transform-Infrared spectrometry (FT-IR). This was done to potentially reveal the configuration of hydrogen/deuterium in β-Ga_2O_3 in order to reveal the origin of the trap for hydrogen. Simultaneously, density functional theory (DFT) calculations were calculated on hydrogen in β-Ga_2O_3, the gallium vacancies and complexes between the two. The energies were compared with the experimental result.

4.2 Experimental diffusion profiles

The experimental diffusion profiles presented here are depth profiles from SIMS measurements. All SIMS measurements were performed with a primary ion current beam at 100 nA, composed of 15 keV Cs^+ and a raster size of $150\ \mu m \times 150\ \mu m$. The field aperture was set to 750 μm and the contrast aperture was set to 150 μm. The depth profiles are shown below and the (010)-oriented samples are shown first.

4.2.1 Deuterium diffusion in (010) β-Ga_2O_3

β-Ga_2O_3 has open channels as shown in Figure 2.4.3. The deuterium is a small atom and is proposed to move interstitially. Hence, a fast diffusion is expected in these (010) oriented samples.

Diffusion in doped (010) β-Ga_2O_3

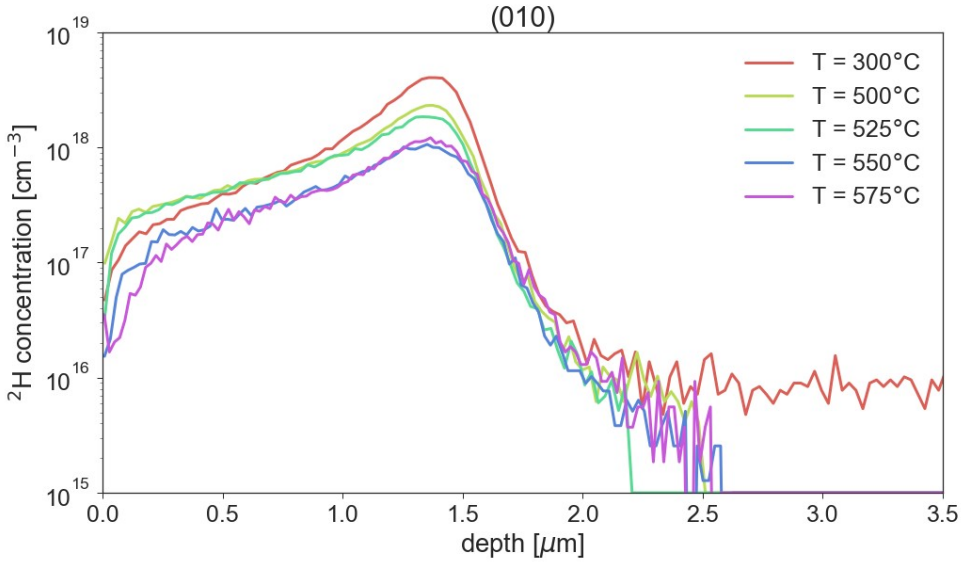

Figure 4.2.1: The experimental data from SIMS measurements of sample B2 after annealing in 20 min (minutes) in temperature steps of 25 degrees from 500 °C to 575 °C. There is also a profile annealed at 300 °C in 30 minutes representing the as-implanted profile.

Figure 4.2.5 shows the experimental profiles from SIMS measurements of Sn-doped (010) β-Ga_2O_3. The sample was annealed at 300 °C for 30 min (minutes). The profile at 300 °C deviates from the simulated shallow as-implanted profile (Figure 4.1.1a) both on the left side and on the right side of

the peak. The deviation on the right side could indicate some channeling during implantation. On the left side however, the profile indicates that there has already been some diffusion from the peak to the surface during the 300 °C anneal. The initial annealing was follwed by heat treatment from 500 °C to 575 °C for 20 min with a temperature step of 25 degrees. The change in the profiles with temperature do not show a broadening of the peak, as one would expect if the diffusion was purely interstitial. The peak height is only decreasing with temperature, and hence indicating that the diffusion of deuterium is occurring below the detection limit of SIMS measurements. This diffusion seems to be fast, since the peak is starting to decrease already at 500 °C.

Interestingly, the re-distribution of the ^{2}H during the 300 °C anneal seems to differ in the shallow and the deep side of the implantation peak. As the simulation in Figure 4.1.1 b) reveals, the ion implantation is generating intrinsic defects on the side towards the surface. This indicates an interplay between intrinsic defects and ^{2}H. By implanting an additional deeper profile, it is possible to deliberately induce intrinsic defects in order to study the effect on the rearrangement of the deuterium.

The deep implantations were done into two already shallow implanted (010) oriented samples. One sample was first implanted with deuterium to approximately 1.5 μm and thereafter deeper to approximately 8 μm in a second implant. Figure 4.2.2 shows the depth profiles after an anneal at 300 °C for 30 min and heat treatments in 20 min at 314 °C, 335°C and 355°C. The depth profile at 300 °C in Figure 4.2.1 is included in the figure to illustrate the pronounced difference before and after the introduction of intrinsic defects on the right side of the peak. The presence of intrinsic defects make it possible to observe the diffusion of deuterium above the detection limit of SIMS. The opposite also holds, i.e. the presence of deuterium make it possible to trace intrinsic defects with SIMS.

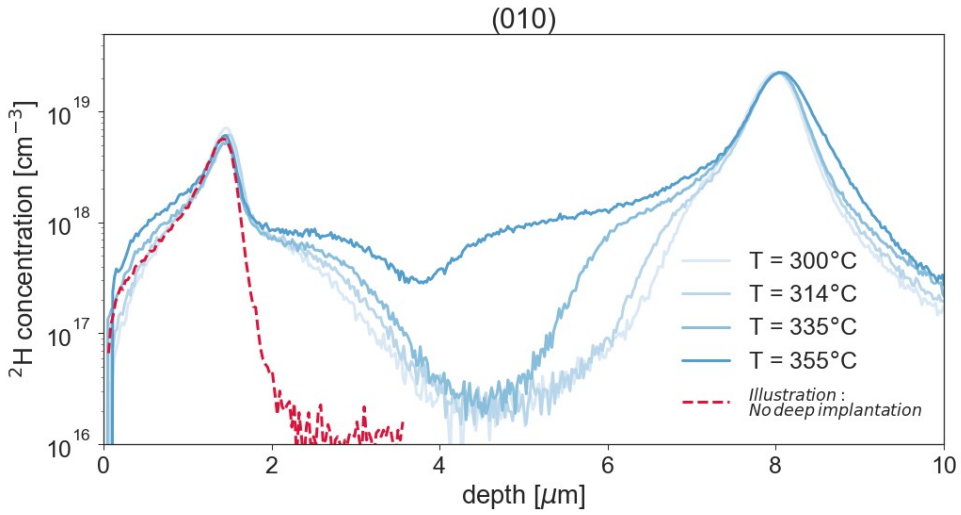

Figure 4.2.2: Experimental data from SIMS measurements of sample C2_2 after annealing in 30 minutes at 300 °C to repair the structure after ion implantation and for 20 min at 314 °C, 335°C and 355°C. The sample have been implanted twice, first a shallow implant, then a deep implant. These profiles have been shifted on the x-axis and the y-axis, so that the peak is in the same position and the same high, with respect to the 300°C-profile.

Figure 4.2.3 shows more clearly how the deuterium is acting as a probe for intrinsic defects. The sample in Figure 4.2.3 was annealed at 300 °C in 30 min, at 314 °C in 20 min and in series from 325

°C to 355 °C with steps of 10 degrees in 20 min. The deep implantation peak shows clear diffusion towards the surface, but neglishable diffusion into the bulk. The first implantation is seen only as a small peak near the surface. The temperature is low and the temperature steps are small, but a substantial deuterium migration is still observed, accordingly the diffusion is fast.

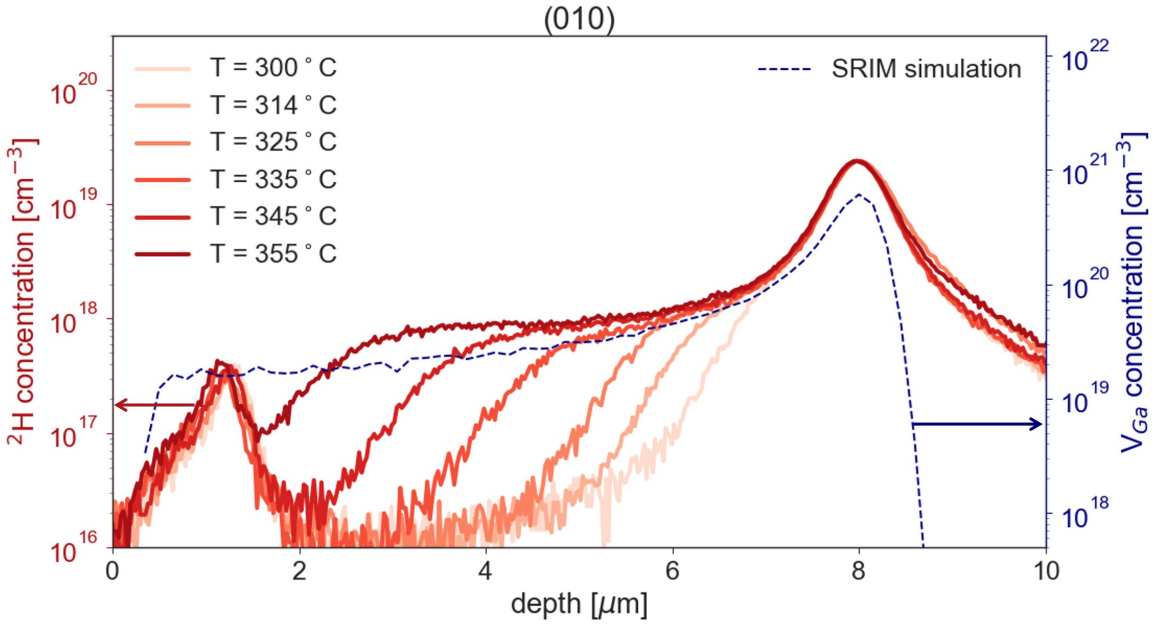

Figure 4.2.3: Experimental data from SIMS measurements after annealing in 30 minutes at 300 °C and for 20 min at 314 °C and from 325 °C to 355 °C in temperature steps of 10 degrees in 20 min. The sample have been implanted twice, first a shallow implant, then a deep implant. The sample was annealed at maximum 600 °C before it was implanted again. These profiles have been shifted on the x-axis and the y-axis, so that the peak is in the same position and the same high, with respect to the 300°C-profile. The result from the SRIM simulation of collsions generating vacancies is added, and if a fraction of 2 % surviving vacancies is assumed, the left y-axis is the concentration of surviving V_{Ga}.

In Figure 4.2.3, the result from the SRIM simulation of collsions generating vacancies during ion implantation is added. The right y-axis is showing the concentration of all vacancies generated during implantation. Only a fraction of these vacancies survive, and if this fraction is set to 2 % the concentration on the left y-axis is the concentration of surviving V_{Ga} as well as [^{2}H]. With this assumption, it can be observed that [V_{Ga}] is approximately half of [^{2}H], which would imply that there are two ^{2}H in each complex between V_{Ga} and ^{2}H. Hence, if 2 % surviving V_{Ga} is reasonable and the dominating gallium vacancy is $V_{Ga}^{O(III)}$, this would be an argument for the presence of the complex observed in FT-IR measurements [31].

4.2.2 Deuterium diffusion in (-201) β-Ga_2O_3

As shown earlier in this thesis, the crystal structure into (-201) oriented β-Ga_2O_3 is not open as in (010) oriented β-Ga_2O_3. This implies that the path of deuterium is likely more complex in the (-201) orientation and the diffusivity is expected to be lower compared to (010) oriented β-Ga_2O_3.

Diffusion in undoped (-201) β-Ga_2O_3

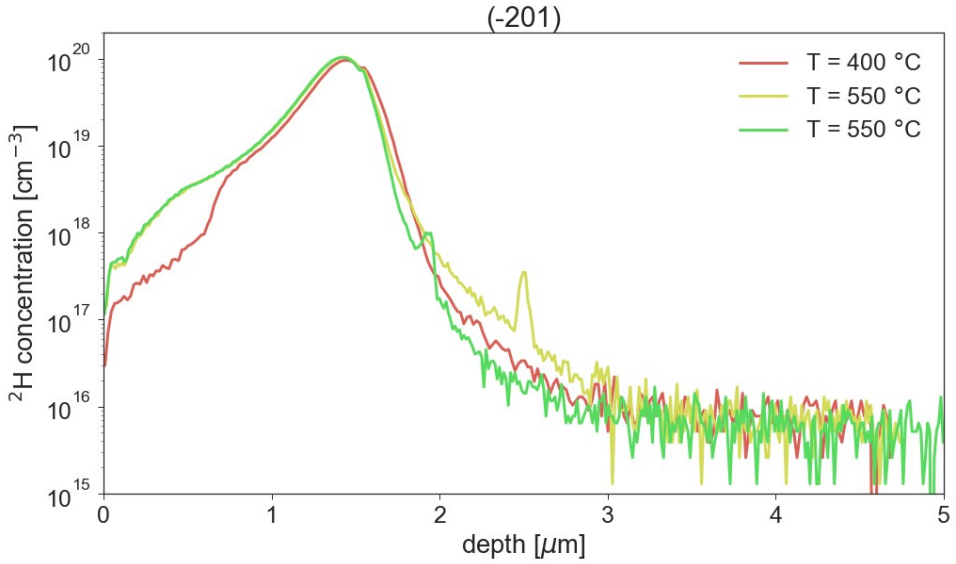

Figure 4.2.4: The experimental data from SIMS measurements after annealing in 30 min at 280 °C and at temperature steps of 50 degrees from 350 °C to 700 °C. The profiles at 400, 500 and 550 °C were the only ones possible to measure. The rest could not be measured because of too much resistivity in the samples due to charge build-up.

Undoped (-201) oriented samples were implanted with deuterium and the depth profiles from SIMS measurements are shown in Figure 4.2.4. These profiles represent the temperatures when the sample was conductive enough so that charge build-up did not occur in the SIMS measurements. The sample was annealed at 280 °C for 30 min and from 350 °C to 700 °C for 30 min with a temperature step of 50 degrees. Two measurements were done at 550 °C because of the appearance of an extra smaller peak. This small peak is present in both measurements, but at different depths. It may be an accumulation of deuterium in a higher dimensional defect. The two profiles at 550 °C is slightly different in shape toward the bulk as well. In both the 400 °C profile and the two 550 °C profiles a diffusion shoulder, similar to the ones in Figure 4.2.2 and Figure 4.2.3, is visible at the left side of the implantation peak. The occurrence of charge build-up in the undoped (-201) samples lead to a switch to doped samples in this orientation as well.

Diffusion into bulk in doped (-201) β-Ga_2O_3

Figure 4.2.5 reveals how deuterium is diffusing into the bulk, on the right side of the implantation peak, in contrast to all the (010) oriented samples. The (-201) sample was annealed from 350 °C to 700 °C for 30 min with a temperature step of 50 degrees. These diffusion profiles resemble the diffusion profiles of deuterium in ZnO [19]. In that case the deuterium was diffusing interstitially into the sample, but being trapped by either the V_{Zn} or a substitutional lithium atom, Li_{Zn}. The model used for ZnO was the trap limited diffusion model, where deuterium is assumed to diffuse interstitially until it is trapped by a point defect in the material. In this model, the height of the shoulder-like part of the diffusion profile is indicating the trap level. In Figure 4.2.5, the trap level is increasing

from the 550 °C to the 600 °C and this will be discussed further later. In addition to the different trap levels, there is also small peaks similar to the ones in Figure 4.2.4 in the profiles above 600 °C.

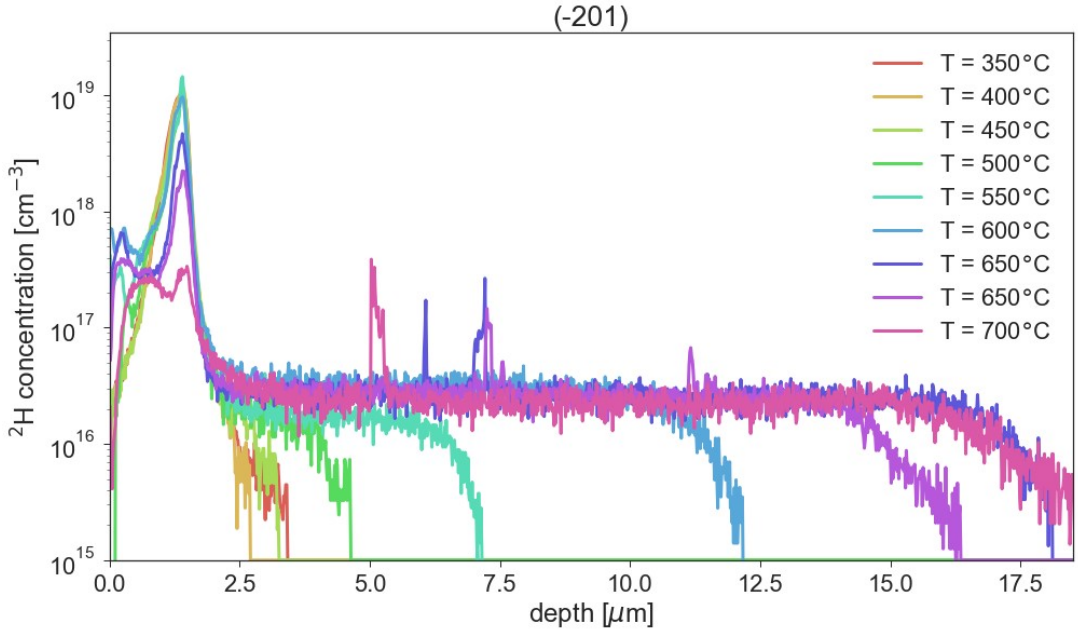

Figure 4.2.5: ^{2}H concentration versus depth profile measured with SIMS. The B1 sample is (-201)-oriented and implanted with ^{2}H. The B1 sample was annealed in 30 min in temperature steps of 50 degrees from 350 to 700.

The diffusion depth is increasing with temperature, but after the anneal at 650 °C, there are two different depths at the same temperature, and the anneal at 700 °C did not move the deuterium substantially from where it was after the 650 °C anneal. The difference between the 700 °C profile and the 650 °C profile, at the same depth, is in their slope at the end of their shoulders. The slope is gentler in the 700 °C profile. It seems that the deuterium that was trapped in the shoulder after the 650 °C anneal is dissociating, and that hardly any new deuterium is arriving from the source in the implantation peak. This can be explained by looking closer at the peak area.

Figure 4.2.6 reveals that the peak height is decreasing during the 650 °C anneal. The peak is not functioning as a stable source after the anneal at 650 °C and hence not supplying new deuterium to fill new traps further into the sample. This explains why the diffusion length is the same after the 700 °C anneal. This could also explain why one of the profiles at 650 °C is shorter than the other one. The shortest profile at 650 °C has a similar shape as the 700 °C profile and that may indicate that the peak, i.e. the source for deuterium, is supplying fewer deuterium where this measurement was performed than the other 650 °C profile. That would imply that the peak has been emptied faster at one point laterally on the sample than another.

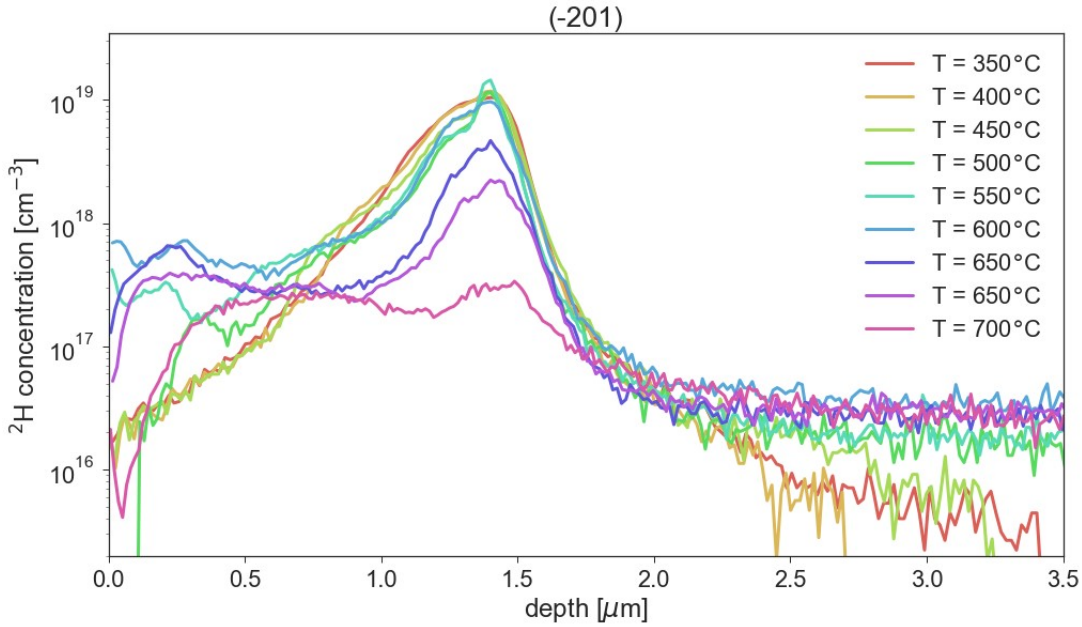

Figure 4.2.6: ^{2}H concentration versus depth diffusion profiles measured with SIMS of β-Ga_2O_3. The B1 sample is (-201)-oriented and implanted with ^{2}H. The figure shows the result after annealing in 30 min in temperature steps of 50 degrees from 350 to 700. This figure shows the peak area of the profile more closely.

The profiles are difficult to assess towards the surface, on the left side of the peak, but deuterium diffusing towards the surface can be observed at 500 °C. It looks like the diffusion in both directions start at the same temperature, but the height of the shoulder is higher in the direction towards the surface. Interestingly, the diffusion is only observed after the 500 °C, indicating that the diffusion is slower in the (-201) orientation as compared to the (010) orientation.

Diffusion in implanted area and not implanted area simultaneously

A deeper implantation was done in Sn-doped (-201) β-Ga_2O_3, similar to that in the (010) oriented samples, in order to generate intrinsic defects at the surface side of the peak and observe the difference in trap level towards the surface and into the bulk. In Figure 4.2.7 the deuterium is diffusing in both directions, towards the surface and into the sample. The sample was annealed for 30 minutes at 300 °C and afterwards heat treated at temperatures from 500 °C to 600 °C in temperature steps of 25 °C in 20 min each time.

Figure 4.2.7 shows the SIMS measurements from the lower temperature anneals. In this plot dotted lines are added to point out the diffusion shoulders which are observed to show a higher trap level on the left side, than on the right side. The SRIM simulation of the concentration of vacancies is added in the same way as for Figure 4.2.3. The SRIM simualtion of the [V_{Ga}] shows the same shape as the diffusion shoulder on the shallow side of the implantation peak, in the area where the deuterium has diffused.

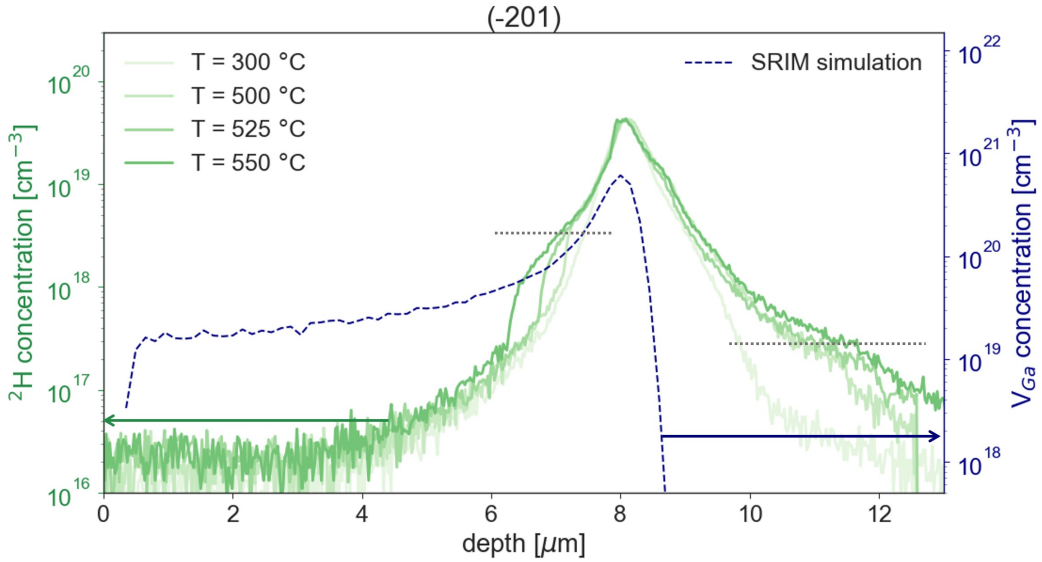

Figure 4.2.7: The experimental data from SIMS measurements of sample D1 after annealing in 30 min at 300°C to repair the structure after ion implantation. The sample was annealed at temperatures from 500°C to 600°C in temperature steps of 25°C in 20 min each time. This sample was implanted deeper than before. These profiles have been moved on the x-axis and the y-axis, so that the peak is in the same position and the same high, with respect to the 300°C-profile. The vacancy concentration after the implantation is illustrated by a profile from the SRIM simulation in Figure 4.1.1, and if a fraction of 2 % surviving vacancies is assumed, the left y-axis is the concentration of surviving V_{Ga}. The dotted horizontal lines call attention to that the diffusion shoulders and show the different trap level at each side of the implantation peak.

Different trap levels laterally on (-201) oriented samples of β-Ga_2O_3

Another Sn-doped (-201) oriented sample of β-Ga_2O_3 was annealed in order to ideally get at least five diffusion profiles, giving four simulations of diffusion before the peak height starts to decrease. The sample was annealed at 300 °C, as a representation of the as-implanted, and from 500 °C to 575 °C at 20 min with temperature steps of 25 degrees.

This measurement series resulted in diffusion profiles with shoulders showing varying trap levels. Figure 4.2.8 shows the profiles separated into relatively short profiles and relatively long profiles. There was a difference in the profiles' depth laterally on the sample after annealing at 550 °C. As a consequence of this, two measurements were performed at 575 °C. The result was another relatively short profile and another relatively long profile. To emphasize the difference of the concentration profiles in the same sample after the same annealing step Figure 4.2.9 shows the different measurements at the same temperature together. These results show that the trap level is different laterally in these EPG grown samples and the trap level has big consequences to how the deuterium behaves.

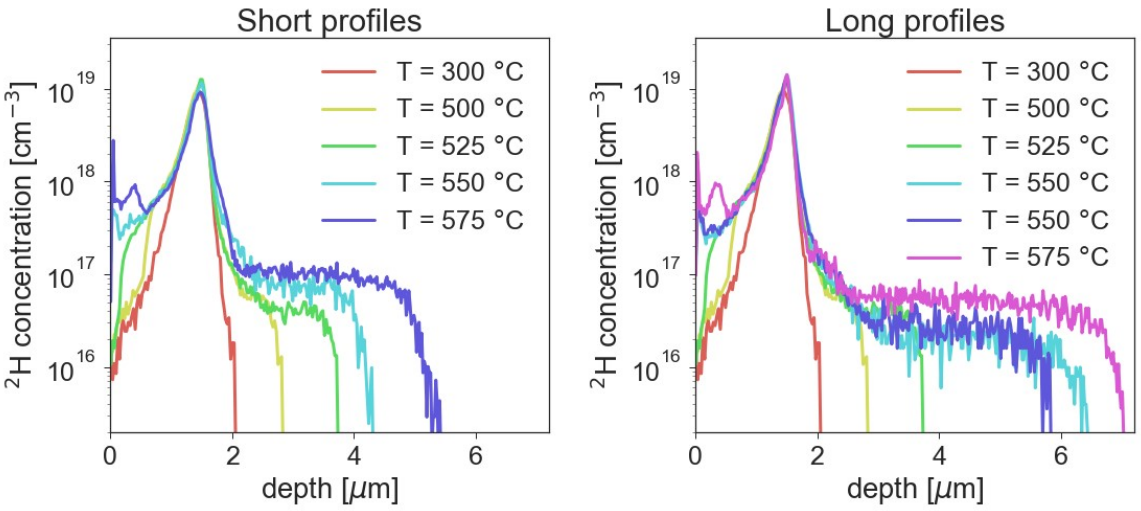

Figure 4.2.8: This is the experimental data from SIMS measurements of sample C1 after annealing in 20 min in temperature steps of 25 degrees from 500 °C to 575 °C. There is also a profile annealed at 300 °C representing the as implanted profile.

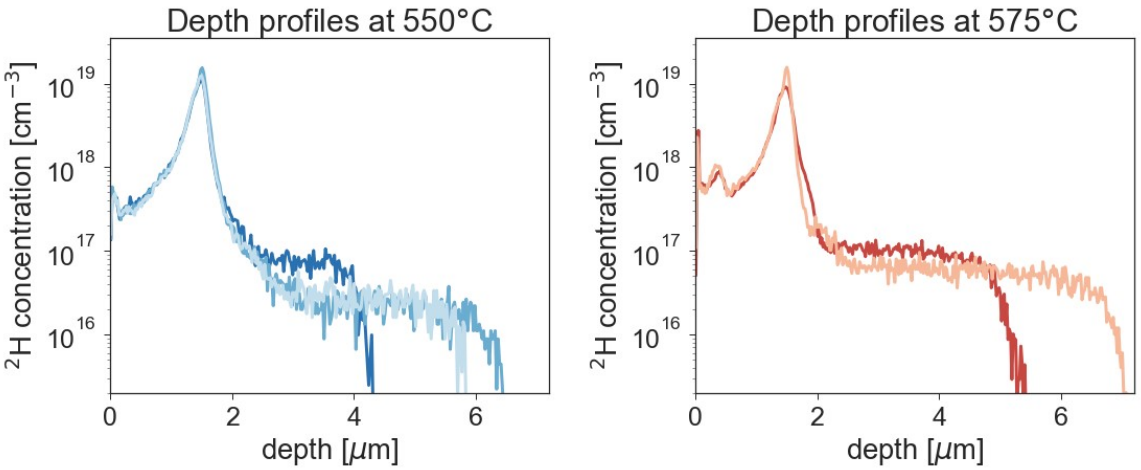

Figure 4.2.9: This is the experimental data from SIMS measurements showing the diffusion depth difference after annealing at the same temperature in the same sample. The only difference is the lateral position of the SIMS measurement. The left plot shows the difference after the anneal at 550°C and the right plot the difference after the anneal at 575°C.

From Figure 4.2.8 a difference in trap level with temperature can also be observed. Figure 4.2.10 shows the different trap level plotted against the temperature and how they were extracted from the experimental profiles. In sample B1 (Figure 4.2.5) an increase in the trap level is observed at 600 °C and then a lowering again after that. It is difficult to explain this as a temperature trend, but with the knowledge from the latter profiles one may argue that the trap level was higher laterally on the sample where the SIMS measurement was made.

Sample C1 (Figure 4.2.8) shows many different trap levels without any clear temperature trends. During the heat treatment series, the lateral difference in trap levels and diffusion depths were checked, but some measurements made close to each other resulted in different trap levels and other measurements performed a couple of millimetres apart gave similar trap levels. Hence, there was no clear trend laterally on the sample either.

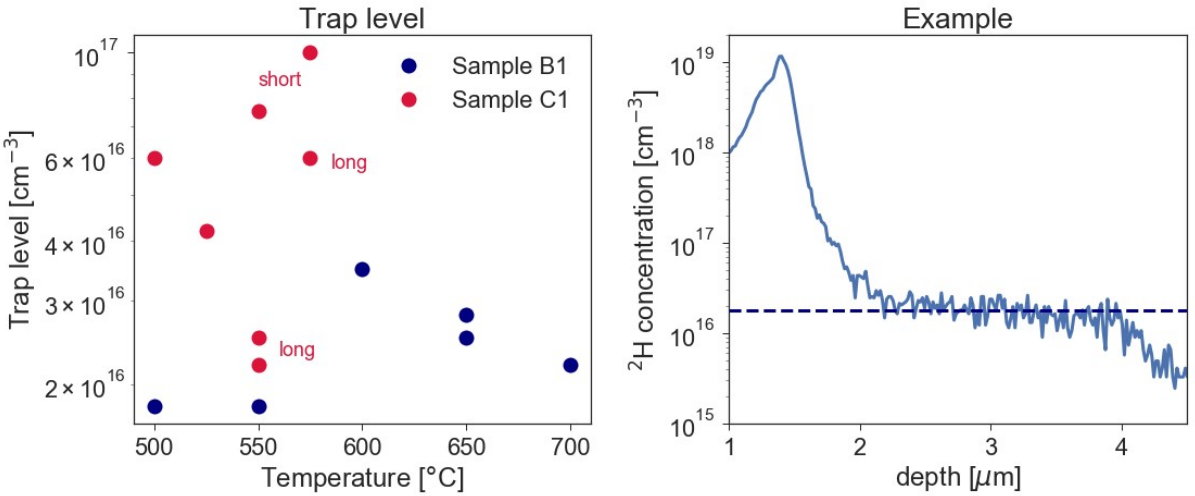

Figure 4.2.10: The trap level of both B1 and C1 (left) was extracted from the experimental data as shown in the right plot. The relative length of the C1-profiles at 550 °C and 575 °C are marked in the plot as "short" or "long".

4.3 Simulating diffusion

Out of all the samples measured and presented above, there were three series that were particularly interesting for diffusion simulation. This is sample B1, sample C1 and sample B2_2. They show clear and systematized diffusion shoulders. In the present section, different models for diffusion, with a main emphasis on trap limited diffusion, ae compared with the experimental diffusion profiles. The different models are illustrated with sample B1, and the rest are in Appendix B.

4.3.1 Simulation diffusion in the (-201)-orientation

In this section, the (-201) orientation is considered first because investigation of it rendered diffusion profiles with a shoulder going into the bulk. This makes the (-201) profiles a good starting point for comparison with diffusion models.

Diffusion length test

A preliminary test was performed using only the diffusion length for every annealing step. The equation describing the relationship between the length and the diffusivity is:

$$l = \sqrt{Dt} \tag{4.1}$$

where l is the difference in depth of the profile after the previous anneal to the depth of the profile

after the current anneal and t is the annealing time. Figure 4.3.1 shows, to the right, how the depth was extracted from the diffusion profiles. And to the left is the diffusivities plotted in an Arrhenius plot to get an activation energy and a prefactor for the diffusion. The activation energy from the Arrhenius plot is $E_a = 1.51$ eV, which is reasonable for diffusion at 500-600 °C and the prefactor, $D_0 = 6.69 \cdot 10^{-2}$cm^2/s, is as expected on the order of 10^{-2}, if there is no change in entropy (see Section 3.3.1). These numbers will be discussed further when the different models are compared with each other.

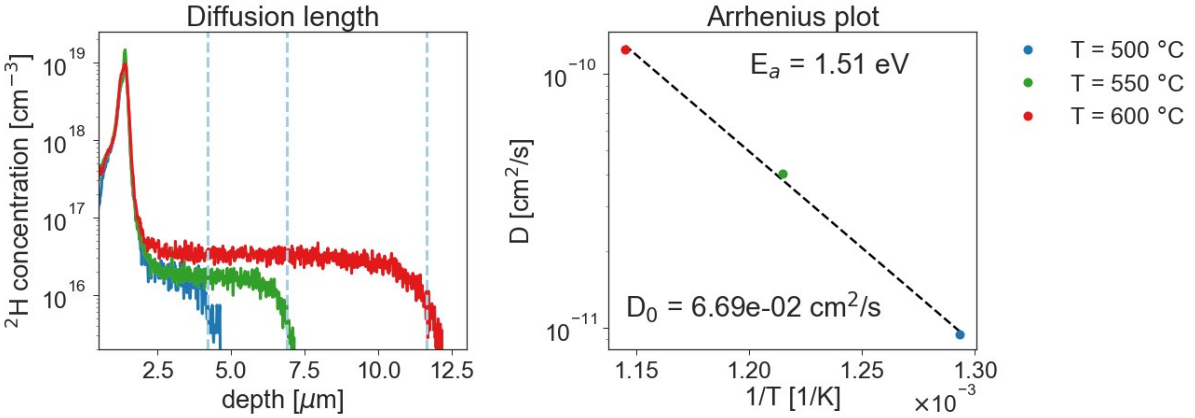

Figure 4.3.1: The diffusion length's relation to the diffusivity shown in Equation 4.1 was used to extract the diffusivity and hence get E_a and D_0. The depth of the diffusion shoulder was extracted from the profile, as the left plot shows, and the change in depth l was calculated from that. An Arrhenius plot was made (the right plot) with the diffusivities and activation energy was found to be 1.51 eV and the prefactor was 6.69 $\cdot 10^{-2}$ cm^2/s.

Semi-infinite source model

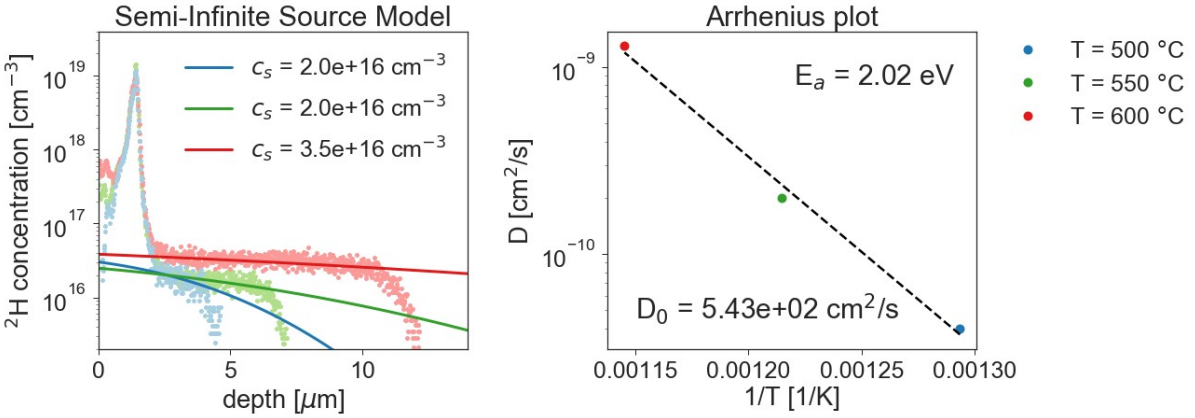

Figure 4.3.2: The left plot: Experimental diffusion profiles compared with the analytical solution of the diffusion equation called the complementary error function. The solid solubility, c_s, is listed in the plot. The right plot: The Arrhenius plot of the diffusivities extracted in the comparison, which resulted in an activation energy of 2.02 eV and a prefactor of $5.43 \cdot 10^2$ cm^2/s.

Next, the semi-infinite source model was used to fit the data. The comparison resulted in an activation energy at 2.02 eV and a prefactor at $5.43 \cdot 10^2$ cm^2/s, which is four orders of magnitude larger than

expected from a single jump (see Section 3.3.1). The plot to the left in Figure 4.3.2 shows how the model can be used to fit the top of the diffusion shoulder, but do not fit the slope at the end. In addition, the model does not fit the implantation peak at all. In the model, the height of the shoulder is determined by, c_s, which represents the solid solubility. The solid solubility is expected to increase as a function of temperature. c_s is listed in the left plot in Figure 4.3.2 and increase from 550 °C to 600 °C, but not from 500 °C to 550 °C. Furthermore, the initial conditions in this model is zero concentration in the sample, which imply that it does not take into account the diffusion profile from the previous heat treatment. The right plot in the figure shows the Arrhenius plot of the diffusivity, that gave the result above.

Trap Limited Diffusion

Finally, the trap limited diffusion model was compared to the experimental profiles. Figure 4.3.3 shows how the TLD model fit the data well. This model include a fit to both the peak and the diffusion shoulder's slope. Figure 4.3.3 shows how the SS model's inclusion into the simulation is keeping most of the deuterium in the peak, hence making the simulated profiles fit the peak. It is evident from this example, that the SS model alone cannot be used to describe the diffusion.

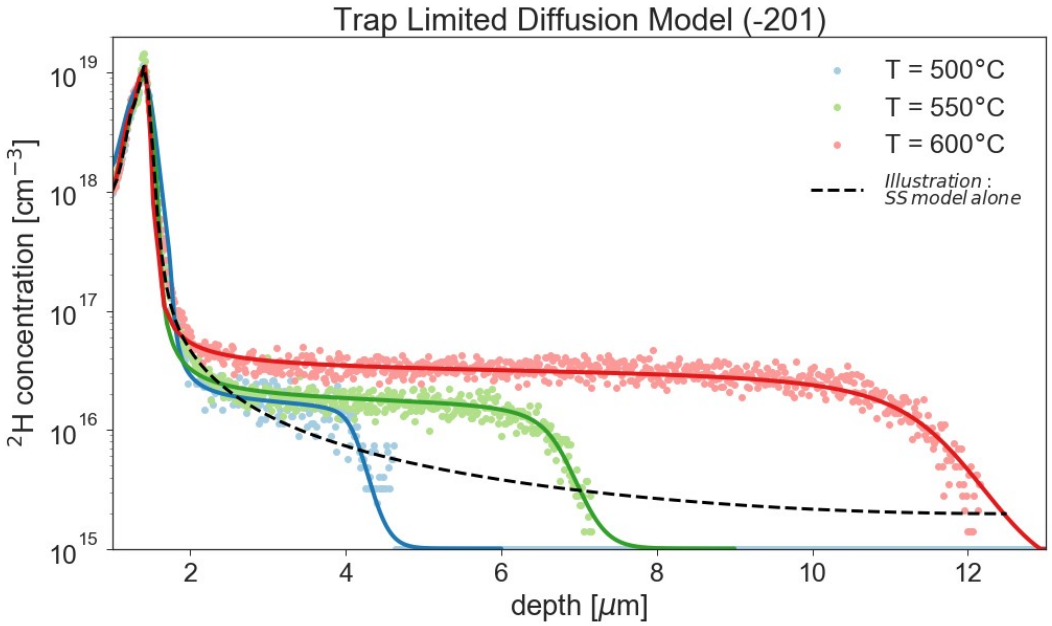

Figure 4.3.3: SIMS data from sample B1 (Figure 4.2.5) compared with the trap limited diffusion model. The SS model is included to show how it keeps the deuterium in the peak, but cannot describe the diffusion behaviour.

The TLD model separate the diffusivity from the dissociation rate, which in turn give both a migration energy and a dissociation energy from the simulations. The result of this for sample B1, is shown in Figure 4.3.4. The migration energy is 2.09 eV, but the prefactor, $D_0 = 4.19 \cdot 10^3$ cm^2/s, of the diffusion is five orders of magnitude higher than the calculated one from Section 3.3.1. It can be observed that the diffusivity at 600 °C is higher than the trend at the two lower temperatures. From Figure 4.3.3 an increase in the trap level is observed, but this do not lead to a shorter depth, as was

observed in the left plot in Figure 4.2.8. The diffusivity seems to be enhanced during the 600 °C anneal. This could also be the case for the long profile at 575 °C (right plot in Figure 4.2.8), since it is showing a high trap level and a relatively long profile. An explanation of this enhancement could be that the implantation peak is releasing more deuterium than at lower temperatures. This again, can be explained by that the dissociation of deuterium from another trap, situated in the implantation peak, is getting significant at around 575-600 °C.

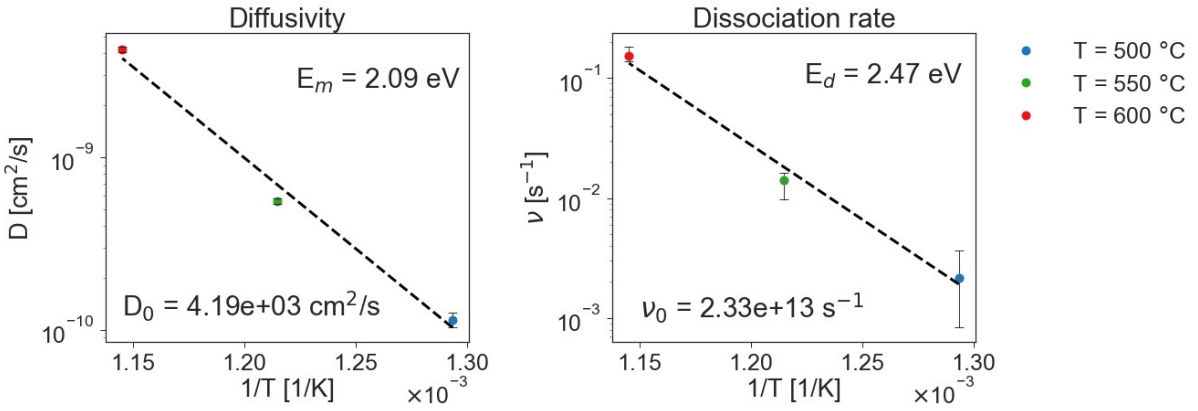

Figure 4.3.4: The resulting Arrhenius plots used to extract the prefactor and activation energy from the trap limited diffusion comparison of diffusion profiles in sample B1 in Figure 4.3.3.

Furthermore, the prefactor of the dissociation is $2.33 \cdot 10^{13}$ cm^2/s. It is around 10^{13}, which is what is expected from the oscillation frequency of the lattice [12]. The dissociation energy is dependent on the binding energy of the deuterium and the trap, and the resulting dissociation energy at 2.47 eV will give a limited amount of dissociated deuterium at 500-600 °C. The deuterium, however, is moving interstitially and, with its small size, the fraction of free deuterium can travel fast before it is trapped again. The dissociation energy will be considered in even more detail after the stability of the $V_{Ga}^{O(III)_2}H_2$ is investigated with FT-IR and the binding energies from density functional theory is presented.

At each point in Figure 4.3.4 there is an error bar showing the error from the simulations of diffusion. Hence this error bar do not cover the uncertainty from SIMS measurements and crater depth measurements, e.g. that the SIMS concentration calibration has an uncentainty of 10 - 20 %. The error bars for the diffusivity at T = 550 °C and T = 600 °C (in the left part of Figure 4.3.4) and the error bar for the dissociation rate at T = 550 °C (in the right) do not reach the line from the linear regression, but by taking into account the uncertainties from the experimental instruments the error bars can be increased. For more information and data about uncertainties see Appendix A.

Figure 4.3.5 shows an Arrhenius plot of all the diffusivities from all the different models and the two (-201) oriented samples with a shallow implantation, i. e. B1 and C1. The diffusion length test (red) is not a good model when the trap level is affecting the depth of the profile. This can be observed by the large diversity of the diffusivity at the same temperature. Despite that, $E_a = 1.60$ eV and $D_0 = 8.85$ cm^2/s. This prefactor is the one closest to the one calculated with the assumption of a neglishable change in vibration entropy (Section 3.3.1). One can observe that both values have increased from the result with sample B1 alone. Next, the result with the comparison with the semi-infinite source model for both samples resulted in $E_a = 2.31$ eV and $D_0 = 1.91 \cdot 10^4$ cm^2/s.

The values have both increased after the inclusion of the results from sample C1. The high prefactor could be explained by the mismatch between the actual diffusion profile and the simulated diffusion profile, and hence that a model with more parameters is necessary to explain the diffusion.

Finally, $E_m = 1.91$ eV and $D_0 = 3.24 \cdot 10^2$ cm^2/s results from comparison with the TLD model for both sample B1 and sample C1. The values have decreased from the result in Figure 4.3.4 now that the result from sample C1 is included. Figure 4.3.6 reveal that $E_m = 1.51$ eV and $D_0 = 1.05$ cm^2/s when plotting the diffusivities obtained from sample C1 with the TLD model. These values are lower than when the 600 °C is included. This could enhance the impression from Figure 4.3.4 of sample B1 alone, that an enhancement of the diffusion is occuring above 550 °C. This enhancement could for example occur by the activation of an additional diffusion mechansim, the activation of an additional migration path or a change in the boundary condition (i.e. source) as mentioned before. On the other hand, it must be kept in mind that the diffusivities from sample C1 is only for a temperature range of 50 degrees. This is a very small temperature range in diffusion studies, and one should not make any firm conclusions based on such a small temperature range. However, the change in both trap levels and depth made the study of the diffusion beyond 550 °C complicated. The initial condition in the simulations is the previously measured profile. Hence, given the observed variation in trap concentration laterally, one could not know if any of the previous profiles measured represented the correct initial condition, and the temperature range of this study ended up being self-limiting.

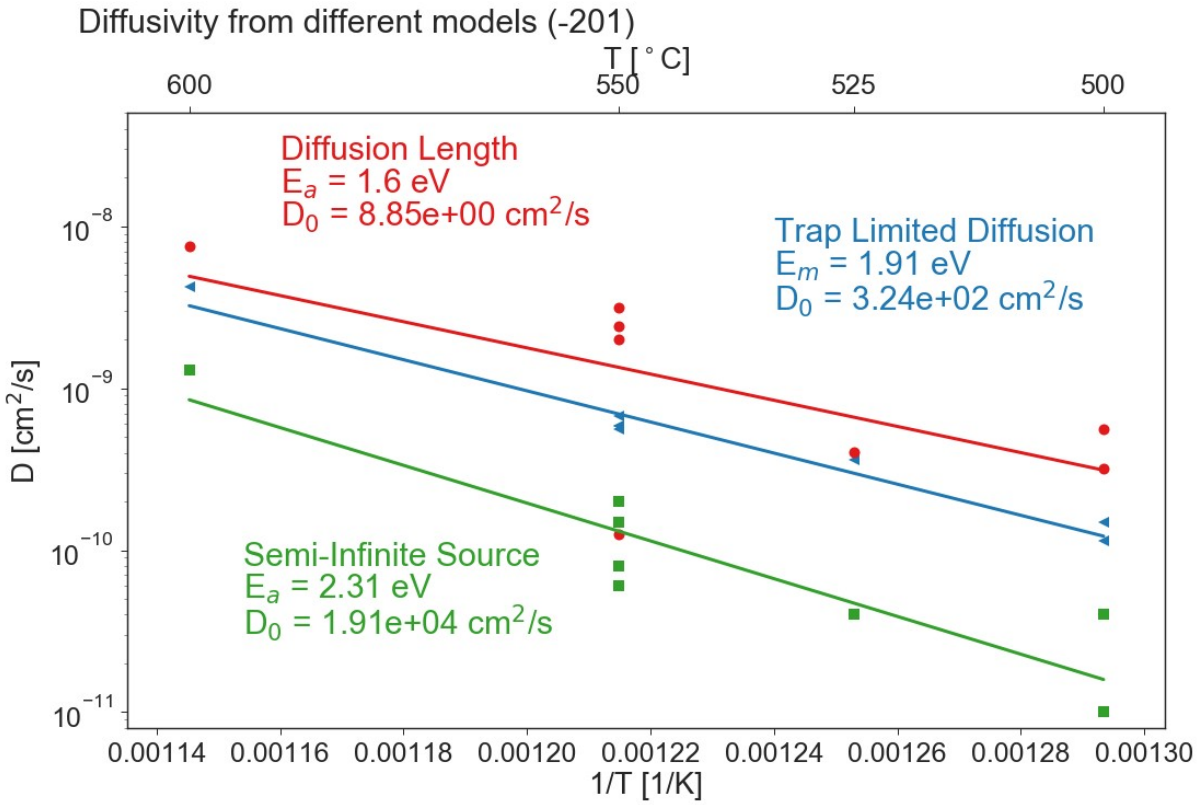

Figure 4.3.5: The resulting Arrhenius plot which compare the diffusivities from the different diffusion models and the results from both sample B1 (see Figure 4.3.1, 4.3.2 and 4.3.3) and C1 (see Figure B.0.1, B.0.2 and B.0.3 in Appendix B). The E_as and D_0s from the diffusion length test (red) and the semi-infinite source model (green), and also the E_m and D_0 from the TLD model (blue) are given in the plot.

By observing the plot in Figure 4.3.6, despite its short temperature range, TLD seems like a reasonable fit, taking into consideration Figure 3.3.3, which shows that the prefactor easily increase with a small change in entropy. A non-neglishable change in entropy could be explained by that the path of deuterium in the (-201) orientation is complicated because of the structure of β-Ga_2O_3.

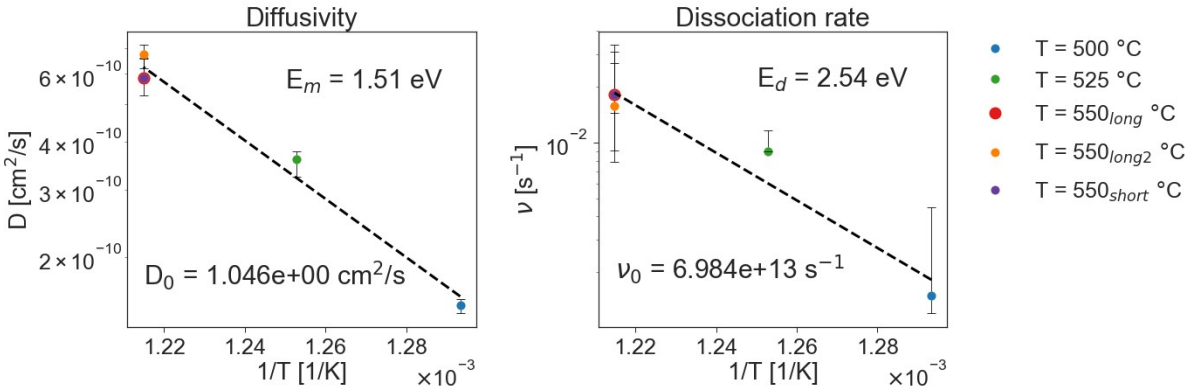

Figure 4.3.6: The resulting Arrhenius plot to extract the prefactor of the diffusion and the dissociation and also find the migration energy and the dissociation energy from the slopes. This was done using the trap limited diffusion model (See Figure B.0.3 in Appendix B).

4.3.2 Simulating diffusion in the (010)-orientation

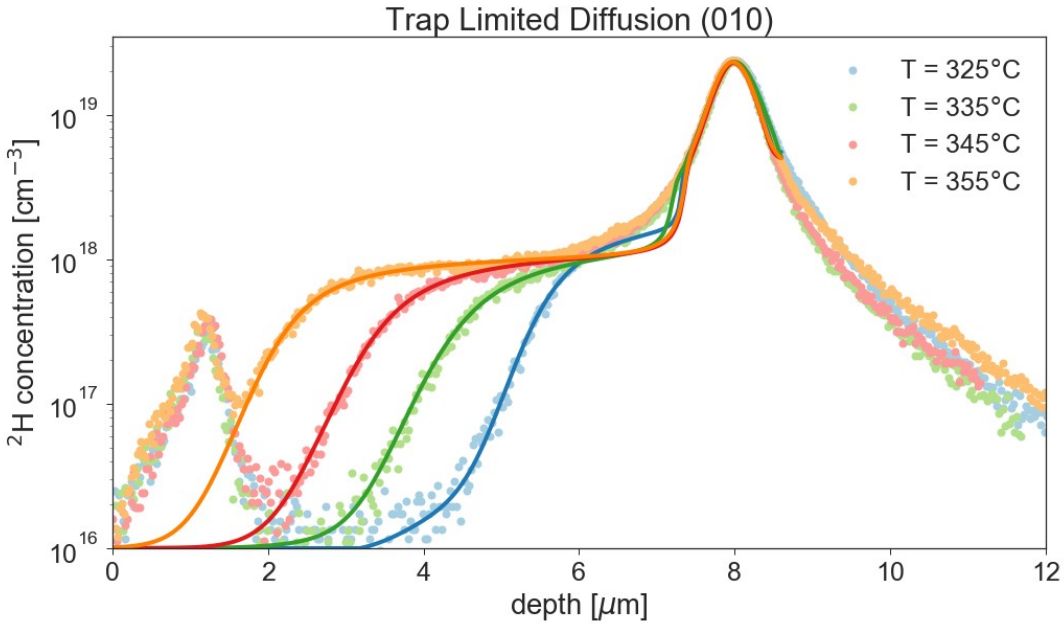

Figure 4.3.7: Experimental diffusion profiles of sample B2_2 which is (010) oriented compared with the trap limited diffusion model.

The same models were used to simulate the diffusion in the (010)-orientation, through sample B2_2. This orientation only showed diffusion shoulders in the ion implanted area where intrinsic defects have

been generated. In this region there are many intrinsic defects, e.g. self-interstitials and vacancies. Still, Figure 4.3.7 reveals that the trap limited diffusion model fit the experimental data adequately, indicating that the TLD model is appropriate for modelling diffusion of deuterium in β-Ga_2O_3.

Figure 4.3.8 reveals that the diffusivities extracted from the comparison with the TLD model result in $E_m = 1.95$ eV, this is a higher activation energy then one would expect for interstitial diffusion in the open channels of the structure of β-Ga_2O_3 in the (010) orientation. Additionally, $D_0 = 7.32 \cdot 10^6$ cm^2/s is much higher than expected for any diffusion prefactor, since it is eight orders of magnitude higher than the one calculated for a single jump in Section 3.3.1. The result of the dissociation shown in the right part of Figure 4.3.8 shows a non-linear behaviour and hence the values extracted can be disgarded. To conclude, the TLD model describe the diffusion profile very well, but the model to not capture the complete meachanism behind the diffusion because the E_m extracted is too high to be the migration energy of deuterium diffusing interstitially. The temperature range could be to small to capture the dissociation's temperature dependence since it is only 30 degrees. This could explain the non-linearity of the dissociation rate with temperature.

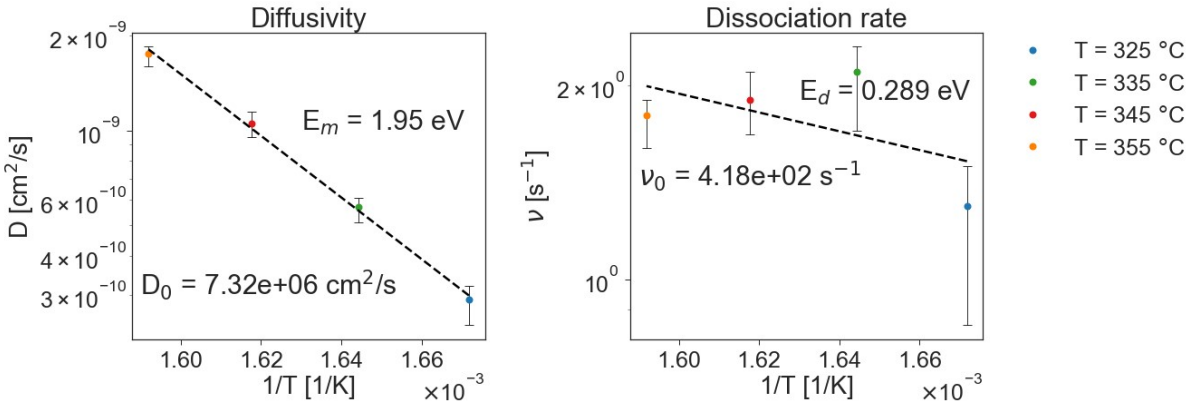

Figure 4.3.8: The resulting Arrhenius plot to extract the prefactor of the diffusion and the dissociation and also find the migration energy and the dissociation energy from the slopes. This was done using the trap limited diffusion model (See Figure 4.3.7).

There are other reasons to why the TLD model would not give expected values for the activation energies and the prefactors in this specific case. One of them being that, in the model, the trap level is assumed to be constant in depth in the simulations, but as Figure 4.1.1 shows, the vacancy concentration, and consequently the concentration of the other intrinsic defects, are increasing towards the peak in the experimental case. Figure 4.2.3 showed how the diffusion shoulder height is decreasing towards the surface due to a decrease in the trap level towards the surface. This also affect the comparison with the semi-infinite source model. When the profiles (in Figure 4.2.3) are compared with the semi-infinite source model, this results in a decrease in c_s, which should represent the solid solubility, but it clearly do not. The decrease in solid solubility with an increasing temperature, do not make sense physically. Coming back to the TLD model, another point is that the constant SS in the SS model part of the simulations had to be increased one order of magnitude because the software was not able to calculate the derivative of the curve for the not trapped deuterium. The most peculiar point about these results are that the profiles can be fit that well with the TLD simulated profiles, and that the experimental data are rather ordered in an area with a high density of defects.

Figure 4.3.9 present the Arrhenius plot of the diffusivities from the TLD model together with the other diffusion models used in this work. The prefactor closest to the calculated assumption for a single jump (see Section 3.3.1) is given by the simplest model, the diffusion length test which result in $E_a = 1.52$ eV and $D_0 = 2.41 \cdot 10^1$ cm^2/s. The values are still high if deuterium, being a small atom, move interstitially in the open channels in the (010) orientation. A higher activation energy can be explained by a trapping of the deuterium in the implantation peak as well as after it leaves the peak. In the TLD model, a continuous flow of deuterium from the implantation peak is assumed. However, if the deuterium is trapped in the peak at these low temperatures and an additional activation energy is required to dissociate it from the peak, this may increase the evaluated activation energy from the models. Furthermore, using the semi-infinite source model results in an even higher activation energy at 3.05 eV, which is higher than all the activation energies from the (-201) orientation, (which is less open than the (010) orientation), and a prefactor of $1.91 \cdot 10^{14}$ cm^2/s which is unphysical since it is 16 orders of magnitude higher than the one calculated for a single jump (see Section 3.3.1).

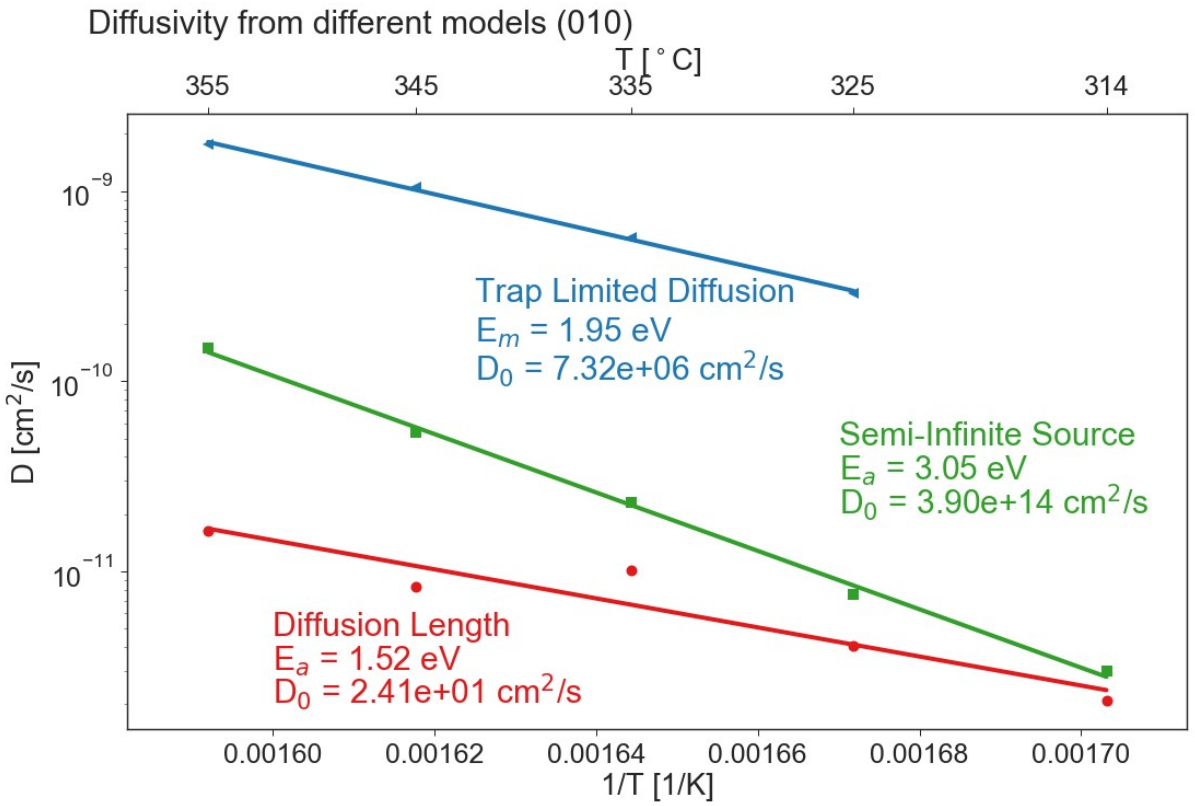

Figure 4.3.9: The resulting Arrhenius plot which compare the diffusivities from the different diffusion models from sample B2_2 (see Figure B.0.4 and B.0.5 in Appendix B and Figure 4.3.7)). The E_as and D_0s from the diffusion length test (red) and the semi-infinite source model (green), and also the E_m and D_0 from the TLD model (blue) is given in the plot.

4.4 ^{2}H/H migration and interplay with $V_{Ga}^{O(III)}$

The experimental diffusion profiles above show deuterium interacting with intrinsic defects in the ion implanted area between the implantation peak and the surface. Interestingly, previously reported FT-IR experiments have identified a complex between $V_{Ga}^{O(III)}$ and two deuterium or hydrogen, and is

thus a prime suspect for the trap capturing deuterium is the $V_{Ga}^{O(III)}$ [31]. New FT-IR measurements were performed on deuterium implanted samples of β-Ga_2O_3 in both orientations to explore this trap option. All the different gallium vacancies and the complexes $V_{Ga}^{O(III)}$ with both one and two hydrogen and $V_{Ga(II)}$ with one hydrogen was investigated with DFT. In addition to that, DFT was used to investigate the migration of the interstitial hydrogen in different directions in the structure.

4.4.1 FT-IR results

In this section, the FT-IR results of deuterium implanted into β-Ga_2O_3 is presented. These measurements were performed on undoped samples of β-Ga_2O_3. Doped samples were investigated, but too high charge carrier absorption had the consequence that the O-^{2}H-line could not be observed in the doped samples. While doped samples were necessary to perform SIMS measurements, undoped samples were necessary to perform FT-IR measurements and a direct comparison using the same set of samples was not possible. Hence, an inherent assumption in a comparison is therefore that the doping do not affect the results, i.e. that any Fermi level effect is neglishable. With the undoped samples, an annealing experiment was executed by annealing the samples from 300 °C to 700 °C for 30 min at temperature steps of 100 degrees.

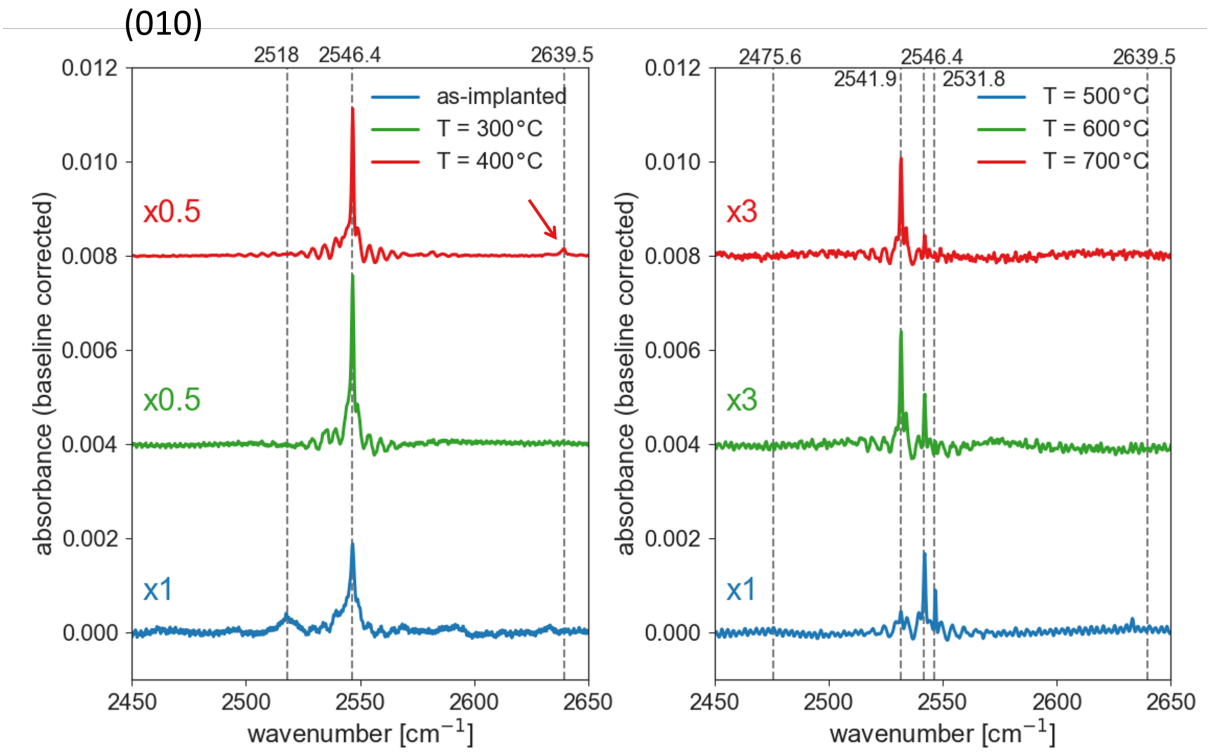

Figure 4.4.1: The absorbtion from the O-^{2}H bond pointing into $V_{Ga}^{O(III)}$ in the (010) oriented sample D2 at as-implanted to 700 °C. The baseline was moved on the y-axis to observe the line is the spectra more easily. The absorbance was also multiplied with by the factors marked on the plot.

All of the FT-IR measurements were performed using a Bruker IFS 125HR Fourier Transform Spectrometer using a globar light source, a KBr beam splitter, and either a liguid-nitrogen-cooled MCT (mid-range) detector or a liquid-nitrogen-cooled InSb detector. The samples were measured at nor-

mal incidence at T = 5 K inside a closed cycle Janis PTSHI-950-5 FT-IR cryostat operating the He exchange gas. The spectral region within ± 100 cm^{-1} of the O-^{2}H defect LVMs were baseline corrected to investigate only the changes in the amplitude of the LVM.

Figure 4.4.1 shows the absorbance spectrum from (010) β-Ga_2O_3 at wavenumbers matching with the O-^{2}H-line. From the spectrum, a peak in the absorbance is observed at $\sigma = 2546.4$ cm^{-1}, confirming the presence of $V_{Ga}^{O(III)2}H_2$ in the as-implanted sample [31]. Several different O-^{2}H lines is observed after the implantation. This is before any annealing, however, the sample has been kept in room temperature for over a year. In addition, an increase of approximately 350 % in the concentration of the $V_{Ga}^{O(III)2}H_2$ from as-implanted to 300 °C is observed. After the 400 °C anneal, the concentration of $V_{Ga}^{O(III)2}H_2$ has decreased to approximately 87 % of the concentration at 300 °C, and another line is appearing at $\sigma = 2639.5$ cm^{-1} (marked in the plot by a red arrow). Furthermore, after the 500 °C anneal, this new line is gone and $[V_{Ga}^{O(III)2}H_2]$ is then lower than the concentration after implantation. It is down to 13 % of the concentration at 300 °C. Two new lines appear at either side of the $V_{Ga}^{O(III)2}H_2$-line at 500 °C. In the 600 °C anneal and in the 700 °C anneal, the $V_{Ga}^{O(III)2}H_2$-line is decreasing even further and the line at $\sigma = 2541.9$ cm^{-1} has increased, the line at $\sigma = 2531.8$ cm^{-1} is gone.

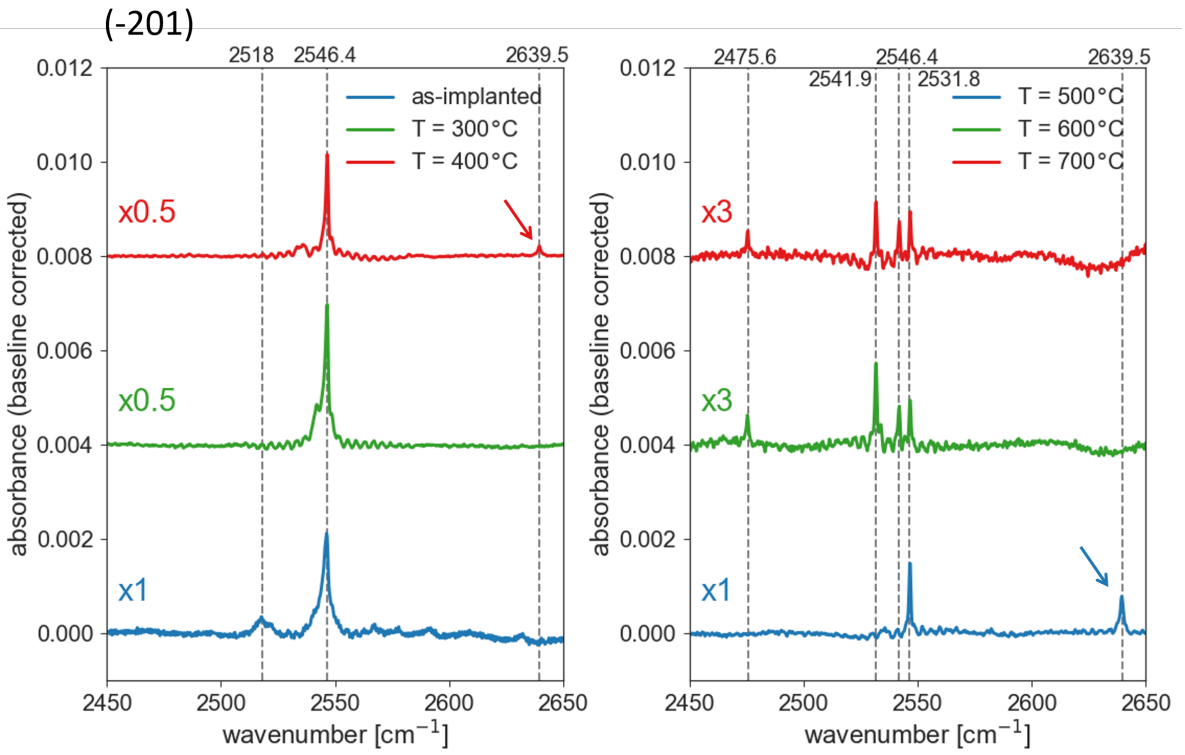

Figure 4.4.2: The absorbtion from the O-^{2}H bond pointing into $V_{Ga}^{O(III)}$ in the (-201) oriented sample D1 at as-implanted to 700 °C. Notice that a different y-axis was used in the left and right plot, to show the peaks more easily.

Figure 4.4.2 displays that the measurements of (-201) oriented samples show a similar behaviour from as-implanted to the 400 °C anneal, as the (010) oriented sample, apart from the lower intensity of the $V_{Ga}^{O(III)2}H_2$-line after the 300 °C anneal and the 400 °C anneal. Another difference is that the

peak at 400 °C has decreased with approximately 72 %. However, in the measurement after the 500 °C anneal, the line at $\sigma = 2639.5$ cm^{-1} is observed to be increasing (marked by a blue arrow) while the [$V_{Ga}^{O(III)2}H_2$] is decreasing even further, going below the as-implanted concentration to 25 % of the 300 °C. The measurements after 600 °C and 700 °C reveal the same two lines on either side of the $V_{Ga}^{O(III)2}H_2$-line as the (010) oriented samples. In contrast to the (010) measurements, all three lines are present at both 600 °C and 700 °C, but the line at $\sigma = 2541.9$ cm^{-1} is the strongest in both orientations. Another difference between the two orientations is the line appearing at $\sigma = 2475.6$ cm^{-1} in the (-201) oriented sample. The line at $\sigma = 2546.4$ cm^{-1} representing the [$V_{Ga}^{O(III)2}H_2$] is at approximately 5 % (at 600 °C and 700 °C) of the concentration at 300 °C. The change in the area under the peak, the integrated absorbance, at increasing temperature is shown in Figure 4.4.3 and showes the same tendencies as described above.

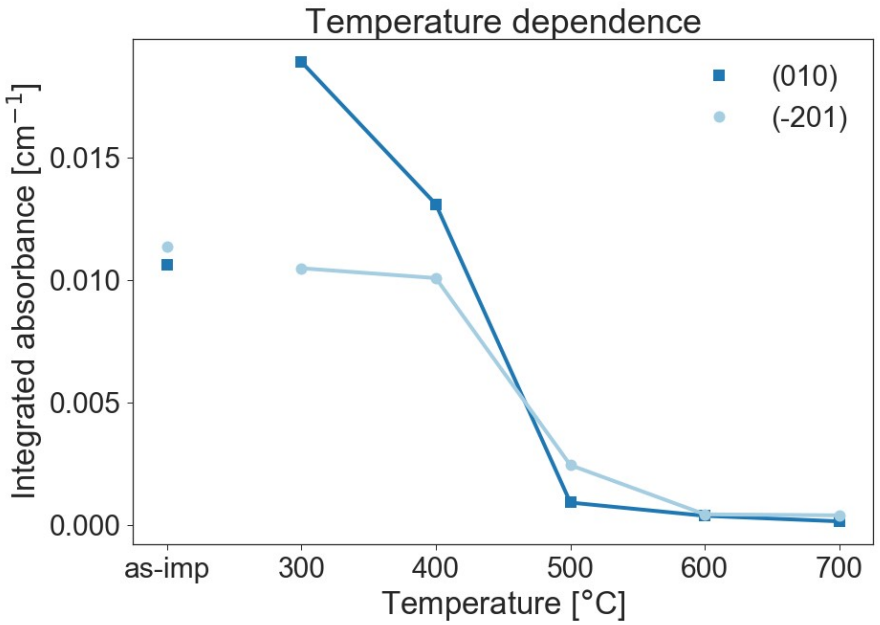

Figure 4.4.3: The change with temperature of the (baseline corrected) integrated absorption is plotted togehter. The intensity from the two different orientations should not be directly compared since the plot is of the absorbance and do not take into account the difference in sample thickness.

These results are different from the result of Sn-doped hydrogenated or deuterated samples of β-Ga_2O_3, where the $V_{Ga}^{O(III)2}H_2$-line was stable until 900 °C [31]. However, the implantation of deuterium will, as Figure 4.1.1 shows, introduce a lot of defects. The $V_{Ga}^{O(III)2}H_2$ complex' decrease in concentration can be a result of different processes. Some options are for instance that one of the deuterium dissociate from the complex, a third deuterium is added to the complex or another defect, e.g. a Ga interstitial, react with the complex in a defect reaction. The first option is more likely in the deuterated samples because there are less defects present near to the $V_{Ga}^{O(III)2}H_2$ and the concentration of deuterium is lower than in the implanted case. The difference can hence be explained by that in the deuterated samples, the decrease is due to dissociation, but in the implanted samples the decrease is due to other defect reactions occurring because of the presence of more defects. For defect reaction to occur the point defects have to be sufficiently mobile to get close

enough to react. The gallium vacancy is mobile already at 500 K according to density functional theory calculations [26]. In addition to this, the Ga interstitial can be expected to be mobile at even lower temperatures. At least, this is the case for Zn interstitials in ZnO which are mobile already at 200 K as reported from density functional theory calculations [58].

Table 4.2: A list of the new O-^{2}H-lines that are observed in Figure 4.4.1 and Figure 4.4.2 showing which temperatures they are present at. The temperatures are in °C.

	(-201)						(010)					
σ[cm^{-1}]	as-imp	300	400	500	600	700	as-imp	300	400	500	600	700
2475.6					X	X						
2518.0	X						X					
2531.8					X	X					X	X
2534.8			X									
2541.9					X	X				X	X	X
2632.5	X						X					
2632.9												
2639.5			X	X					X	X		

The new lines observed in the measurements in Figure 4.4.1 and Figure 4.4.2 are listed in Table 4.2. These new lines could give some answers to what is happening with $V_{Ga}^{O(III)2}H_2$, but no identification has been made for these lines yet. An isotopic test with implantation of hydrogen is also necessary to confirm that the lines are O-^{2}H-lines.

4.4.2 The formation energies of V_{Ga} and H_i

DFT calculations were performed to obtain an atomistic view on the diffusion of hydrogen in β-Ga_2O_3. The main goal of the calculations were to extract the dissociation energy and the migration energy, and compare these with the energies from the diffusion modelling. The dissociation energy is found from the binding energy and the migration energy. Subsequently, the binding energy is the difference between formation energies, which consequently is the first topic of this section.

Considering the FT-IR results, some investigation of gallium vacancies and their combination with hydrogen was pursued. Figure 4.4.4 shows the formation energy for the different gallium vacancies in both gallium-rich and oxygen-rich conditions. Our experimental set-up is between these two limits, but more towards the oxygen-rich limit, since the annealing was done in air. Only the formation energies for a high Fermi level, which is representative for n-type β-Ga_2O_3, were calculated. Our samples were either unintentionally doped n-type or intentionally doped n-type, and they are both believed to be within the range of the plots in Figure 4.4.4. Figure 4.4.4 reveals that the shifted vacancies, explained in Figure 2.4.4, are the vacancies with lowest formation energy.

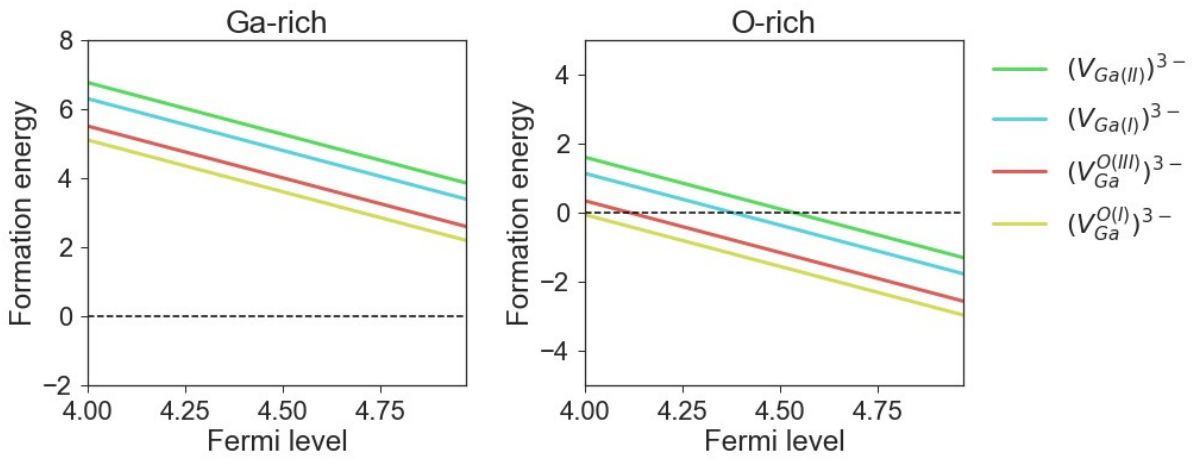

Figure 4.4.4: The formation energies of the different gallium vacancies. The formation energy dependence on the Fermi level and the atmospheric pressure are shown by plotting it against the Fermi level and showing the two extreme atmospheres, oxygen rich and gallium rich. The plot is only of the Fermi level near the conduction band, hence this figure show only the relevant charge states for an n-type β-Ga_2O_3.

As previously mentioned, two deuterium in a complex with the shifted vacancy $V_{Ga}^{O(III)}$ is in accordance with the results from FT-IR [31]. This complex is depicted in Figure 4.4.5. The two deuterium are partly filling the open volume marked with blue arrows on either side of the shifted gallium atom, which are marked by the red arrow.

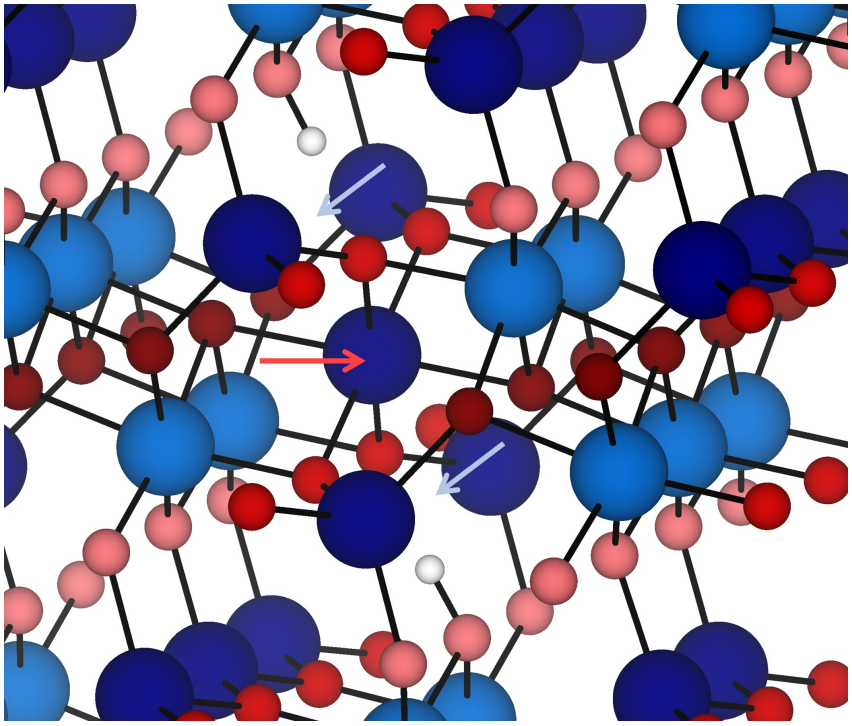

Figure 4.4.5: The $V_{Ga}^{O(III)}H_2$ complex, where the blue arrows show the open volume left on either side of the shifted gallium atom, which are pointed out by the red arrow. The two white balls are hydrogen.

The formation energy of the complex discussed above was calculated. Figure 4.4.6 compare this

formation energy with the formation energy of the same vacancy with only one hydrogen and the complex between $V_{Ga(II)}$ and one hydrogen. For comparison, the hydrogen interstitial's formation energy was calculated as well.

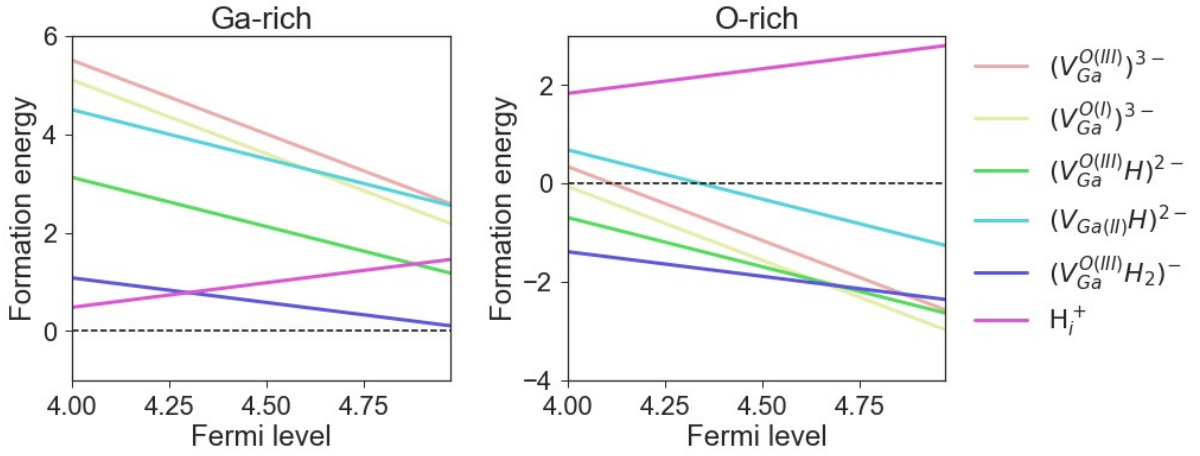

Figure 4.4.6: The formation energies of the different gallium vacancies, the complexes between the gallium vacancy and the hydrogen and the interstitial hydrogen. The plot is only of the Fermi level near the conduction band, hence this figure show only the relevant charge states for n-type β-Ga_2O_3.

Figure 4.4.6 reveal that $(V_{Ga}^{O(III)}H_2)^-$ has the lowest formation energy in Ga-rich conditions, if the Fermi level is assumed to be higher than 4.30 eV. The hydrogen is therefore more likely to be in this complex under those conditions. At the O-rich limit, however, $(V_{Ga}^{O(III)}H_2)^-$ does not have the lowest formation energy at high Fermi levels. Both $(V_{Ga}^{O(III)}H)^{2-}$ and $V_{Ga}^{O(III)}$ have a smaller formation energy than $(V_{Ga}^{O(III)}H_2)^-$.

The defect equation for the formation/dissociation of a gallium atom in a complex with two hydrogen is

$$(V_{Ga}H_2)^- \leftrightharpoons (V_{Ga}H)^{2-} + H_i^+. \tag{4.2}$$

This equation show that the alternative option for the hydrogen, to be in the complex $(V_{Ga}^{O(III)}H)^{2-}$ include the formation of an interstitial hydrogen. However, the interstitial hydrogen have a much higher formation energy as compared to the complexes, making it less likely to form. $(V_{Ga}^{O(III)}H_2)^-$ is thus the more likely option for the hydrogen. Given that the formation energy of $(V_{Ga}^{O(III)}H)^{2-}$ is just slightly smaller than $(V_{Ga}^{O(III)}H_2)^-$ and also including an assumption that there are an abundance of $V_{Ga}^{O(III)}$. The same argument can be made for the defect reaction

$$(V_{Ga}H)^{2-} \leftrightharpoons V_{Ga}^{3-} + H_i^+. \tag{4.3}$$

The formation energies above can be used to calculate the binding energies, E_b, of the various complexes by calculating the difference in energy between the isolated species (A and B) and the complex (AB):

$$E_b[AB] = E^f[A] + E^f[B] - E^f[AB] \tag{4.4}$$

A positive binding energy means that the formation energy of the isolated defects are higher than the formation energy of the complex, hence the formation of the complex is thermodynamically favorable.

The binding energies are listed in Table 4.3 and their positive value show that there is an attrative interaction between the interstitial hydrogen and the two vacancies, $V_{Ga}^{O(III)}$ and $V_{Ga(II)}$.

Table 4.3: The binding energies of the gallium vacancy and hydrogen. The most relevant binding energy is the difference between the most stable complex, $(V_{Ga}^{O(III)}H_2)^-$ and $(V_{Ga}^{O(III)}H)^{2-} + H_i^+$.

Complex:	E_b [eV]:
$\left(V_{Ga}^{O(III)}H_2\right)^-$	2.52
$\left(V_{Ga}^{O(III)}H\right)^{2-}$	2.86
$\left(V_{Ga(II)}H\right)^{2-}$	2.75

The values are within a reasonable range from Varley et.al.'s published results that gave $E_b[V_{Ga}^{O(III)}H] =$ 3.02 eV and $E_b[V_{Ga(II)}H] = 2.82$ eV [29]. The difference that is observed between this work and [29] can probably be attributed to differences in the corretions used. The correction energies can be large when the the defects have multiple charges [59], hence the difference is also larger.

4.4.3 Migration energies of H_i

The following migration energies were found using NEB with PBEsol functionals. The migration energies can be used in combination with the binding energy to calculate the dissociation energy. They can also be directly compared with the migration energies extracted from the experimental diffusion profiles.

Migration energy in the (010)-orientation

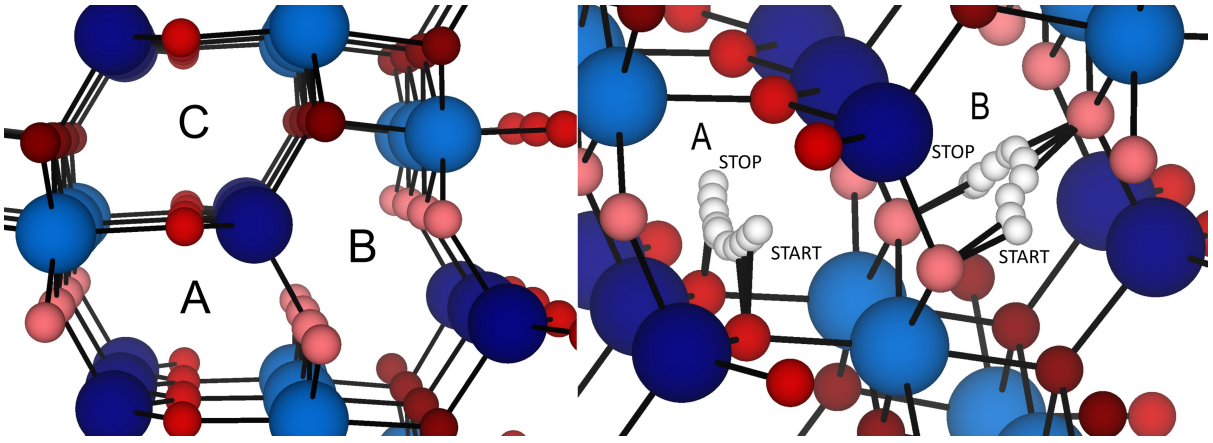

Figure 4.4.7: The three different channels for H diffusion in the (010) orientation (left). The migration paths calcualted with NEB for channel A and channel B (right).

It is assumed that hydrogen will diffuse interstitially along the open channels in the (010)-orientation of β-Ga_2O_3. Two different channels in the structure was tested and the two are marked by the letters A and B in Figure 4.4.7. The third one, channel C, was not investigated in this work. At first, channel C looks like a mirroring of channel A, but the O(III) in channel C is tetrahedrally

coordinated, compared to the planar coordination of O(I) in channel A. Therefore, a difference in migration behaviour is anticipated of a hydrogen in this third channel. The white balls in the right part of Figure 4.4.7 are the hydrogen moving in the structure. Each hydrogen is a separate image in the NEB calculation. The hydrogen has moved from START to STOP in both channels.

Figure 4.4.8 reveal that the migration path in channel B is the most interesting one, because it has a substantially lower migration energy, only 0.18-0.40 eV, compared to channel A which has E_m =3.09 eV. However, the NEB calcualtion of channel A did not converge below 0.04 eV/Å in the transition state image, only below 0.08 eV/Å.

The path in channel B (Figure 4.4.7) show the hydrogen starting bonded to an oxygen on one side of the channel, moving down into the channel and getting attached to an oxygen on the other side of the channel and eventually coming back to the same side of the channel in an equivalent position as to where it started. As a reference, the energy of an interstitial hydrogen in channel C is included in the plots in Figure 4.4.8. The difference in energy between the interstitial hydrogen in channel A compared to channel C is very small and not visible in the plot.

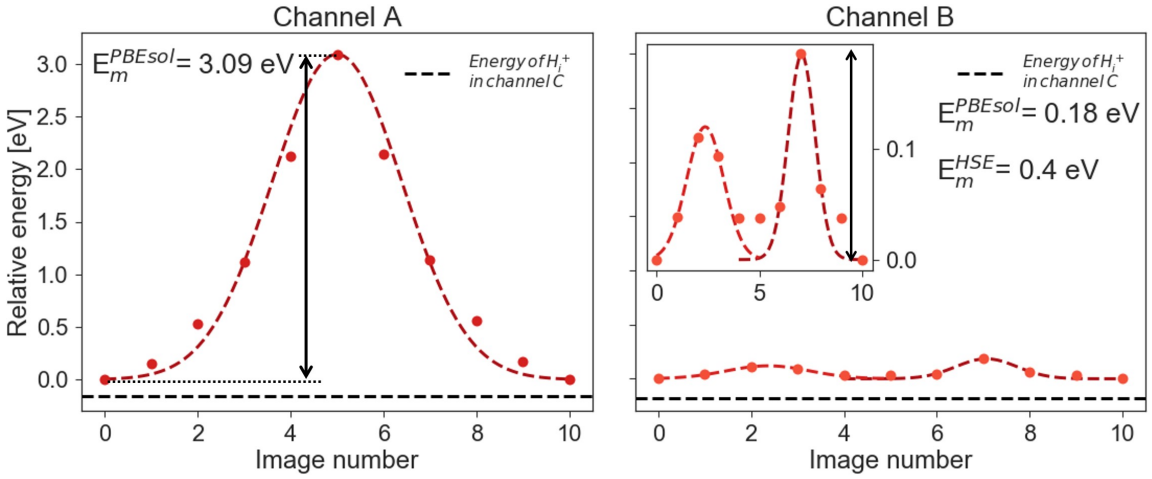

Figure 4.4.8: Plot of the potential energy of the interstitial hydrogen migrating from one interstitial site to another in the (010) orientation. The potential energy of the path in both channel A and channel B is shown together with a gaussian curve, to show an approximation of the potential energy from one site to another. A smaller plot of the potential energy is included for the path in channel B, to get a better look at the energy of the different images along the path. The migration energies, the highest relative energy on the path, are printed on the plot and marked by the black arrows.

The plot to the right in Figure 4.4.8 show that there are two thermally activated steps involved in the motion, where the last one, the motion from the other side of the channel back to the side again, is the higher one. The image with the highest energy is image 7. The energy at the transition state was calculated with HSE functionals as well, resulting in a higher migration energy. With a migration energy of 0.40 eV, one would expect hydrogen to move very easily, in this direction, already at room temperature, if it is not hindered in any way.

Migration in the (-201)-orientation

The left part of Figure 4.4.9 shows the different jumps that have been calculated with NEB for the diffusion in the (-201) orientation and their respective migration energies. In the right part of the figure, the red line represents the diffusion direction, which is then normal to the (-201) plane. Furthermore, the arrows are showing proposed combinations of the calculated jumps, that could represent the migration of hydrogen in this direction. None of the proposed paths are strictly normal to (-201). There is therefore a difference in the distance the hydrogen has moved on the proposed path and the distance it has moved projected onto the diffusion direction (the direction probed when using (-201) oriented samples). The term distance here, is used as the change in position from the starting position to the end position, like the arrows depict in Figure 4.4.9.

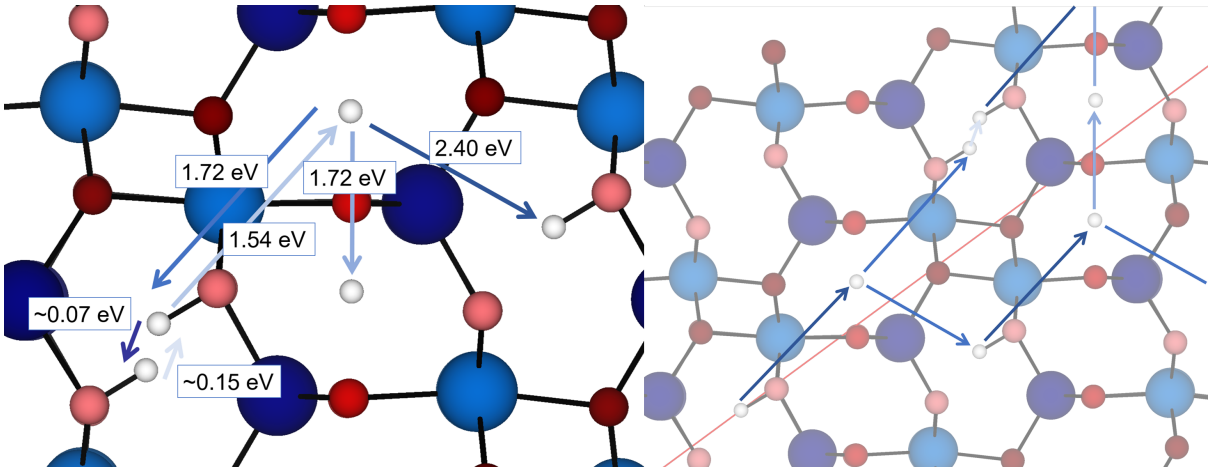

Figure 4.4.9: To the left: The migration energies from the NEB calculations of different jumps in the dircetion similar to diffusion in the (-201) orientation. The migration energies for the shortest jumps are the ones from the migration in the (010) orientation (see channel B in Figure 4.4.8) . The migration energies here are all calculated with PBEsol functionals. To the right: Proposed combinations of the different calculated jumps.

The path marked with the darkest blue arrows in Figure 4.4.9, is the path combined of migration energies with the smallest maximum at 1.72 eV. The limiting jump in the lowest energy path is then the jump shown in Figure 4.4.10, however, in the opposite direction. The illustration to the right in Figure 4.4.10 shows the hydrogen moving from one interstitial site to another. The different hydrogen in the illustration is the different images from the NEB calculations. The images show how the O-H-bond is rotated around the first oxygen, then the hydrogen jumps from one oxygen to the next and eventually the bond is rotated again. The energy of the different images are shown to the left in Figure 4.4.10. The highest energy is found for image 7. The migration energy in the two different directions are shown with a red and a blue arrow. Interestingly, the migration energy, shown with the blue arrow, $E_m^{\rightarrow}$, where calculated at the HSE level as well as PBEsol, and the two functionals give a similar number. This could be an indication that PBEsol is sufficiently accurate in describing the migration barrier. However, the difference was bigger in the (010) orientation.

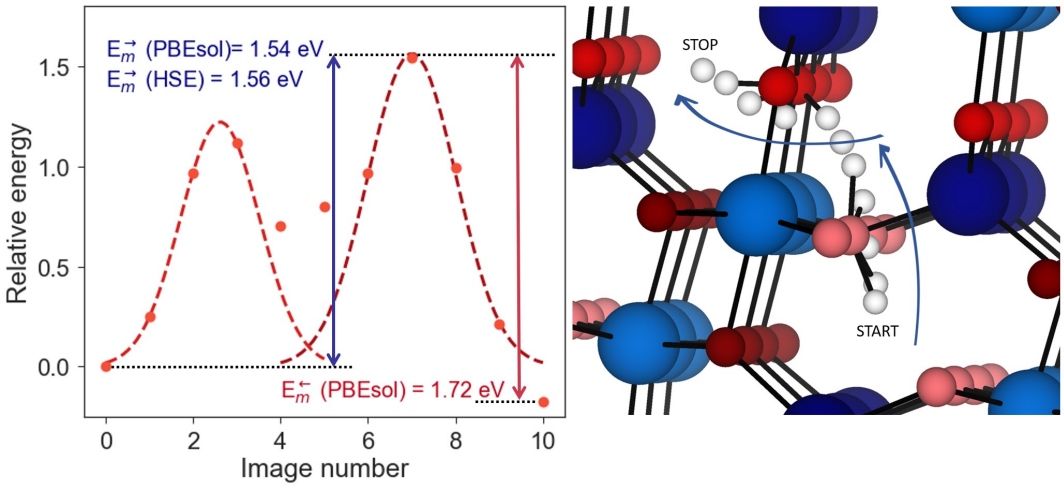

Figure 4.4.10: To the left: Plot of the potential energy of the interstitial hydrogen migrating from one interstitial site to another in the proposed limiting jump in the (-201) orientation. The migration energies, the highest relative energy on the path, are printed on the plot and marked by a blue and a red arrow based on which direction the migration energy represents. To the right: The minimum energy path from NEB calcualtions.

It should be emphasized that this is only a proposal. Since the (-201) orientation is complicated and it is difficult to know the minimum energy path the hydrogen can take. In this work only a few jumps were explored, and there may exist a combination of jumps with lower energy. In addtion, several convergence test should be performed on the migration energies, both related to supercell size, $E_{cut-off}$ and k-point density to make sure that the migration energies extracted here are converged. The difficulties of converging the transition state in channel A (see Figure 4.4.8), indicate the necessity of these convergence tests.

4.4.4 Dissociation energies of complexes with V_{Ga} and H

The components of the dissociation energy, E_m and E_b are presented above and E_d can be extracted from it. The smallest migration energy (0.18-0.40 eV, PBEsol-HSE) was used together with the binding energies in Table 4.3 to calculate the dissociation energy. From that, dissociation temperatures were calculated with the jump frequency in Equation 2.23. The attempt frequency, Γ_0, was set to 10^{13} s^{-1}, as before, and substantial dissociation was assumed to occur with a jump frequency at $\Gamma = 1$ min^{-1}. All the dissociation energies and temperatures are listed in Table 4.4.

Table 4.4: The dissociation energy and dissociation temperatures for the various complexes of a gallium vacancy and hydrogen. $E_d = E_b + E_m$, and hence the migration energy calculated with both PBEsol functionals and HSE functionals are included, to show the resulting range in E_d.

Complex	Dissociation energy (PBEsol−HSE)	Dissociation temperature (PBEsol−HSE)
$(V_{Ga}^{O(III)}H_2)^-$	2.70 eV − 2.92 eV	940 °C − 1038 °C
$(V_{Ga}^{O(III)}H)^{2-}$	3.04 eV − 3.26 eV	1092 °C − 1191 °C
$(V_{Ga(II)}H)^{2-}$	2.93 eV − 3.15 eV	1043 °C − 1141 °C

4.5 Combining theoretical and experimental approach

In this section, the migration energies from diffusion modelling with the TLD model will be compared with the migration energies from ab initio calculations. In addtion, the dissociation energies extracted for diffusion in the (-201) orientation with the TLD model, will be compared with the dissociation energy of $V_{Ga}^{O(III)}{}^2H_2$ from the DFT calculations. Finally, the hypothesis of $V_{Ga}^{O(III)}$ as the trap for ^{2}H is evaluated.

4.5.1 Comparing E_m and E_d

For (010) oriented β-Ga_2O_3, the experimental migration energy from using the TLD model to model the diffusion was 1.95 eV. This is substantially higher than the values found with DFT which was 0.18 eV with PBEsol functionals and 0.40 eV with HSE functionals. The reasons for the large value from diffusion modelling have already been discussed; One would expect a lower migration energy than 1.95 eV when the deuterium is observed to be diffusing already at 300 °C (Figure 4.2.2). Hence, the activation energy extracted is probably not the migration energy of ^{2}H diffusing interstitially. Addisionally, the dissociation rate extracted with the TLD model, did not show Arrhenius behaviour. Thus, the E_d could not be extracted and compared with the dissociatoin energy from DFT calcualtions.

The experimental result for E_m in (-201) oriented β-Ga_2O_3 extracted by the TLD model is compared with the result from DFT in Figure 4.5.1. From the figure, one can observe that the result from the two approaches are somewhat compatible. $E_m^{\text{TLD}} = 1.89$ eV and $E_m^{\text{DFT}} = 1.72$ eV (with PBEsol functionals) and the difference is 0.17 eV. To emphasis the influence of the proposed enhanced diffusion at 600 °C, a linear fit was done with and without the data point at 600 °C. Without the 600 °C data point, E_m^{TLD} is lowered to 1.62 eV and the difference is only 0.10 eV. There are some uncertainties in both approaches, which has already been elaborated on, but the combined result is a migration energy at 1.6-1.9 eV for diffusion of ^{2}H in the (-201) orientation.

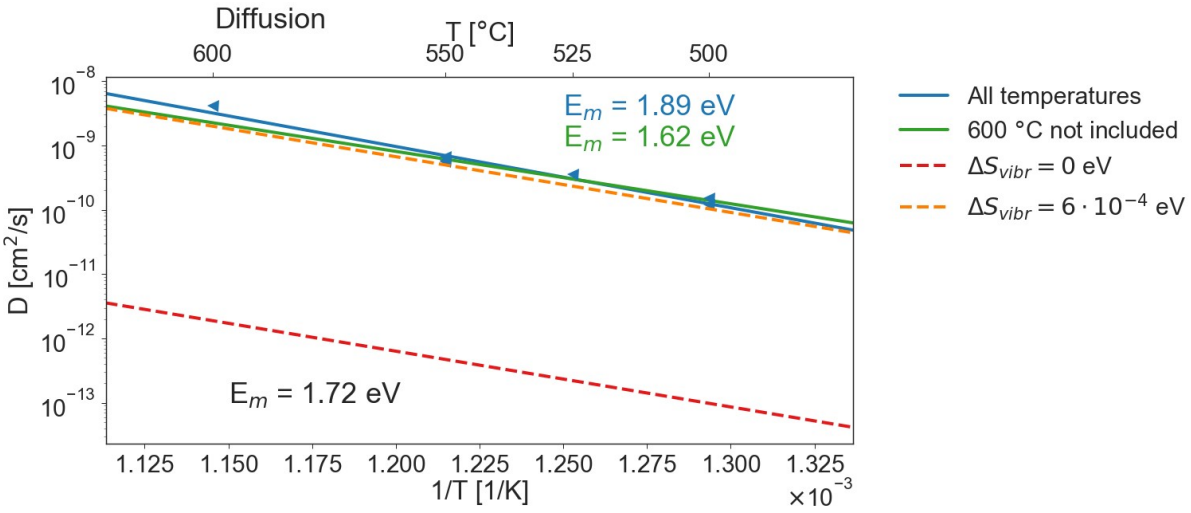

Figure 4.5.1: The migration energy extracted by the TLD model from (-201) β-Ga_2O_3 is compared with the migration energy from DFT calculations (stippled lines). For the lines representing the DFT result, two different prefactors were used with and without a vibrational entropy change. To emphasis the influence of the enhanced diffusion at 600 °C, a linear fit was done with and without that data point.

In Figure 4.5.1, the migration energy from DFT calculations was plotted with the calculated value for D_0 with the assumption that there is no change in vibrational entropy and that the jump distance, λ, is 4 Å in the (-201) orientation (see Section 3.3.1). It was also plotted with $\Delta S_{vibr} = 6 \cdot 10^{-4}$ eV, to illustrate that only a small change in the vibration entropy can increase D_0 a lot and maybe explain why the D_0 extracted with the TLD model is higher than the estimated one.

Figure 4.5.2 reveals that $E_d^{\text{TLD}} = 2.58$ eV, and only slightly smaller when excluding the data point at T = 600 °C, and $E_d^{\text{DFT}} = 2.92$ eV. The difference between the two values is thus 0.34 eV. If the value for E_d with a E_m from PBEsol functinoals is used (see Table 4.4), the difference is only 0.22 eV. If the migration energy from the TLD model is close to the real migration energy, E_d^{TLD} should also correspond to E_d^{DFT}, assuming that the correct trap is used.

In the ab initio calculations in this work, the focus has been on $V_{Ga}^{O(III)}$ as the trap, with two deuterium in it, and it is the dissociation energy of this complex, that is compared with the E_d extracted with the TLD model in Figure 4.5.2. Also, the other traps investigated, $V_{Ga}^{O(III)}$ with one ^{2}H and $V_{Ga(II)}$ with one ^{2}H, had even higher dissociation energies than $V_{Ga}^{O(III)}$ (see Table 4.4) and would have given a bigger difference, thus they were not included in this comparison.

The red dotted line in Figure 4.5.2 are several orders of magnute lower that the experimental data points from the TLD model when $\Delta S_{vibr} = 0$ eV is assumed, but the inclusion of the same amount of change in vibrational entropy as in Figure 4.5.1 show that an inclusion of only $\Delta S_{vibr} = 6 \cdot 10^{-4}$ eV (yellow dotted line) increase the prefactor considerably.

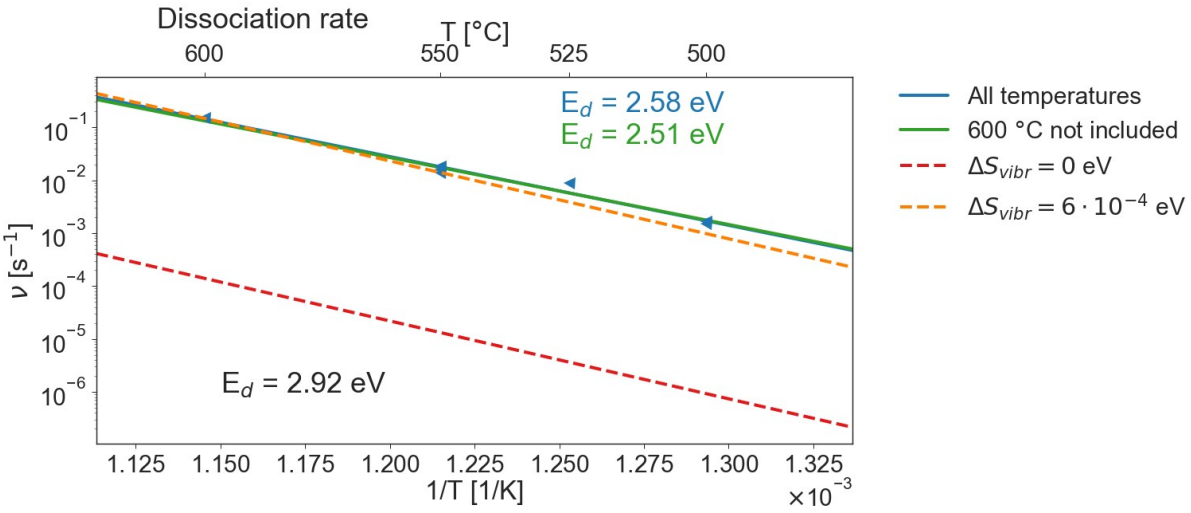

Figure 4.5.2: The dissociation energy extracted by the TLD model from (-201) β-Ga_2O_3 is compared with the dissociation energy from DFT calculations (stippled lines), assuming that the trap is $V_{Ga}^{O}(III)$ with two ^{2}H. For the lines representing the DFT result, two different prefactors were used with and without a vibrational entropy change. The exclusion of the 600 °C data point was done here too, in accordance with Figure 4.5.1.

4.5.2 Evaluation of $V_{Ga}^{O(III)}$'s involvement in ^{2}H diffusion

A remaining question is whether $V_{Ga}^{O(III)}$ is the main trap for the deuterium, especially if it is the trap that one can observe capturing deuterium in the bulk in the diffusion profiles in (-201) β-Ga_2O_3. The TLD model was showed to simulate the experimental diffusion profiles, but the model assumes that the traps do not move. Contrary to this, ab initio calculations have showed that the gallium vacancies are mobile at 500 K which is approximately 225 °C [26]. Thus the gallium vacancy is mobile in all our measurements, and it do not fulfill the assumption of the model. The results from the simulations, however, showed that some other thermally activated process is involved in the diffusion. Hence, the vacancy and the hydrogen might be migrating together as a complex in addition to the hydrogen migrating interstitially.

The ab initio calculations from this work, showed $V_{Ga}^{O(III)}{}^2H_2$ to be the complex with the lowest formation energy, especially considering the alternatives tested. There could, however, be another complex which was not calculated in this work, but neither a mass spectrum obtained with SIMS of the samples nor FT-IR measurements have any more likely candidates for the trap. There is a case for the trap being an intrinsic defect because the experimental diffusion profiles show an evident interaction between the deuterium and intrinsic defects in the implanted area, but deuterium is small and reactive and it is known to make complexes with both extrinsic and intrinsic defects. Since the hydrogen is a donor, it will most likely make a complex with a negatively charged acceptor, this could be any of the gallium vacancies and also extrinsic acceptors, e.g. Fe and Mg.

The FT-IR measurements showed an evident decrease of the $[V_{Ga}^{O(III)}{}^2H_2]$ at annealing temperatures above 400 °C. This decrease is probably only a decrease in concentration in the implantation peak because the implantation peak have several degrees of order higher concentration, of both ^{2}H and $V_{Ga}^{O(III)}{}^2H_2$, than the diffusion shoulder. Hence, $V_{Ga}^{O(III)}{}^2H_2$ could still be present in the shoulder, acting as the trap, because the contribution from the shoulder to the signal in FT-IR is below its

detection limit. The decrease of $[V_{Ga}^{O(III)2}H_2]$ could be due to defect reaction between $V_{Ga}^{O(III)2}H_2$ and all the other defects in the implantation peak. These reactions can be annihilation of $V_{Ga}^{O(III)}$ by a Ga interstitial which free the ^{2}H, or the addition of more ^{2}H in $V_{Ga}^{O(III)2}H_2$, since the peak region have an abuncance of ^{2}H, even though these complexes are less stable than $V_{Ga}^{O(III)2}H_2$ [60].

Chapter 5

Conclusion

In this chapter, the findings of this work will be summarized and further work to get an even deeper understanding of deuterium diffusion in β-Ga_2O_3 is suggested.

5.1 Summary

We have found that deuterium is diffusing at a lower temperature in the (010) orientation, i.e. below 300 °C, than in the (-201) orientation where no diffusion is observed until heat treatment at 500 °C. Furthermore, the trap limited diffusion model has been found to describe the experimental diffusion profiles well. However, the activation energies, extracted with Arrhenius plots of the diffusivities and dissociation rates from the simulations, indicate that another thermally activated process, in addition to the interstitial migration of deuterium and the dissociation from the traps, is involved, especially in the (010) orientation. This additional thermally activated process is proposed to be connected to that the implantation peak is not acting as a semi-infinite source for deuterium as assumed in the model.

The density functional theory calculations with the nudge elastic band method to find the migration energies were performed and the result was in accordance with the experimental diffusion profiles. The calculations showed anisotropic diffusion, where the migration energy in the (010) orientation, i.e. E_m = 0.18-0.40 eV for PBEsol and HSE functionals respectively, was substantially lower than in the (-201) orientation where E_m = 1.72 eV, with PBE functionals, in the proposed migration path and around 1.72-2.30 eV in the other calculated jumps.

In addition, the experimental diffusion profiles obtained by SIMS showed that the trap level was different in the bulk for the (010) oriented samples and the (-201) oriented samples. The (010) oriented samples had trap levels below the detection limit of SIMS, i.e. $1 \cdot 10^{15}$cm^{-3}, while the trap levels in the (-201) oriented samples varied from $2 \cdot 10^{16}$ cm^{-3} to $2 \cdot 10^{17}$ cm^{-3}, also laterally on the same sample. This was discovered due to complex formation between the deuterium and the trap, where deuterium is acting as a probe for the traps. Subsequently, interaction between the deuterium and intrinsic defects was observed (after a deep ion implantation which created additional intrinsic defects in the region between the implanted peak and the surface) by the re-distribution of the deuterium after heat treatment.

FT-IR measurements were performed to investigate possible traps for deuterium, and the results showed that $V_{Ga}^{O(III)2}H_2$ was present in the samples. Additionally, the results showed that $[V_{Ga}^{O(III)2}H_2]$ decreased substantially at heat treatments above 400 °C for samples of both orientations, i.e. (010) and (-201). This result was different from deuteriated samples of β-Ga_2O_3 which showed a stable $[V_{Ga}^{O(III)2}H_2]$ up to heat treatments at 900 °C [31]. The difference can be explained with the additional defects generated during ion implantation and the abundance of deuterium in the peak. This increase the probability of other defect reactions occurring, that decrease $[V_{Ga}^{O(III)2}H_2]$, than the dissociation of the complex as one would expect in the deuteriated case. From the FT-IR results, we also found new unidentified peaks in the O-^{2}H/O-H region which could explain what is occurring in the peak during heat treatments and shed light on the proposed additional limitation on deuterium diffusion from deuterium trapping in the implantation peak.

5.2 Further work

The work presented in this thesis has reveal new insight into the behavior of H in β-Ga_2O_3. Although several questions have been answered, additional investigations and improvements would enhance our under understanding further. In particular for the NEB calculations, extra convergence tests of the migration energies extracted in this work should be performed with respect to supercell size, cut-off energy and k-point density in order to verify the results from this work. The additional channel in the (010) orientation could also be tested, in case it can enlighten the diffusion of hydrogen in the (010) orientation. In addition, the NEB calculations can be performed in a HSE relaxed supercell since the HSE relaxation gives lattice parameters closer to the experimental lattice parameters. The additional HSE calculation of the migration energy will also be more accurate in a HSE relaxed supercell. Furthermore, NEB calculations can also be used to gain in formation about how the hydrogen dissociate from traps by finding a migration path out the complex. This could be especially interesting for complex which, unlike $V_{Ga}^{O(III)2}H_2$, to not have the deuterium already in channel B (see Figure 4.4.7), but in one of the other channels.

The results above indicated that the implantation peak is affecting the diffusion of deuterium. An investigation of the new lines observed in the IR absorbance spectra is therefore interesting to perform. A new batch of samples can be implanted with deuterium's isotopic partner, hydrogen, which should shift the center wavenumbers of the new ^{2}H-related lines to the 3000-3600 cm^{-1} spectral region. If the ratio of the wavenumber of the H-related line to the wavenumber of the ^{2}H-related line is $\sim$1.35 (close to the classical effect), the defect involves hydrogen/deuterium bonded to oxygen atoms. Co-implantations with hydrogen and deuterium can reveal the number of hydrogen atoms contained in each defect. A combination of these measurements, with control over the polarization of the incident light, and DFT calculations may be used to identify the new lines, as has been done for the $V_{Ga}^{O(III)2}H_2$ line.

A solution to get a wider temperature range in the Arrhenius plot of the (-201) orientation and thus lower the uncertainties is (in an ideal world where there are an abundance of samples) to use one sample for each heat treatment. In this manner the problem of the previous profile being unknown would be solved because it would be the as-implanted profile. It could also be of interest to create more vacancies in the bulk of the samples in both orientations by heating the samples at a high temperature and cooling them fast. This way, one could get a higher trap level in the (010)

oriented samples and investigate diffusion in a region with less defects than in the implanted region. The disadvantage of this method is the additional tampering with the samples which can introduce impurities and unwanted defects as well at gallium vacancies.

A remaining question is if $V_{Ga}^{O(III)}$ with two hydrogen is the trap observed from the experimental diffusion profiles. A combination of positron annihilation spectroscopy (PAS) and SIMS can be used to investigate the gallium vacancies, hopefully, with and without deuterium. This can be done by probing the region between the surface and the implantation peak in the deep implanted samples with PAS before and after deuterium has filled the traps in this region. SIMS in hence used to see how far the deuterium has diffused towards the surface. A change in the data of the gallium vacancies would indicate the presence of deuterium in the gallium vacancy. The PAS data can also be combined with DFT calculations to investigate the influence of deuterium of the data from the gallium vacancy.

Bibliography

[1] S. Chu and A. Majumdar. Opportunities and challenges for a sustainable energy future. *nature*, 488(7411):294, 2012.

[2] Akito Kuramata, Kimiyoshi Koshi, Shinya Watanabe, Yu Yamaoka, Takekazu Masui, and Shigenobu Yamakoshi. High-quality β-Ga_2O_3 single crystals grown by edge-defined film-fed growth. *Japanese Journal of Applied Physics*, 55(12):1202A2, nov 2016.

[3] G. Jessen, Ke. Chabak, A. Green, J. McCandless, S. Tetlak, K. Leedy, R. Fitch, S. Mou, E. Heller, S. Badescu, et al. Toward realization of Ga_2O_3 for power electronics applications. In *Device Research Conference (DRC), 2017 75th Annual*, pages 1–2. IEEE, 2017.

[4] B. E. Kananen, N. C. Giles, L. E. Halliburton, G. K. Foundos, K. B. Chang, and K. T. Stevens. Self-trapped holes in β-Ga_2O_3 crystals. *Journal of Applied Physics*, 122(21):215703, 2017.

[5] S. J. Pearton, J. Yang, P. H. Cary IV, F. Ren, J. Kim, M. J. Tadjer, and M. A. Mastro. A review of Ga_2O_3 materials, processing, and devices. *Applied Physics Reviews*, 5(1):011301, 2018.

[6] J. B. Varley, J. R. Weber, A. Janotti, and C. G. Van de Walle. Oxygen vacancies and donor impurities in β-Ga_2O_3. *Applied Physics Letters*, 97(14):142106, 2010.

[7] C. G. Van de Walle. Hydrogen as a Cause of Doping in Zinc Oxide. *Phys. Rev. Lett.*, 85:1012–1015, Jul 2000.

[8] C. Freysoldt, Bl. Grabowski, T. Hickel, J. Neugebauer, A. Kresse, G.and Janotti, and C. G. Van de Walle. First-principles calculations for point defects in solids. *Reviews of modern physics*, 86(1):253, 2014.

[9] B. G. Streetman and S. K. Banerjee. *Solid state electronic devices*. Prentice-Hall, 2016.

[10] F. A. Kröger. *The chemistry of imperfect crystals*. North-Holland Publ., 6 edition, 1964.

[11] F. A. Kröger and H. J. Vink. Relations between the concentrations of imperfections in crystalline solids. *Solid State Physics*, 3:435307, 1956.

[12] M. S. Janson, A. Hallén, M. K. Linnarsson, and B. G. Svensson. Hydrogen diffusion, complex formation, and dissociation in acceptor-doped silicon carbide. *Physical Review B*, 64(19):195202, 2001.

[13] D. V. Schroeder. *An introduction to thermal physics*. Addison-Wesley, 2000.

[14] J. M. Philibert. *Atom movements: diffusion and mass transport in solids*. Ed. Physique, 1991.

[15] P. M. Fahey, P. B. Griffin, and J. D. Plummer. Point defects and dopant diffusion in silicon. *Reviews of modern physics*, 61(2):289, 1989.

[16] T. Norby. *Defects and Transport in Crystalline Solids*. Compendium in KJM5120 at UiO, 2015.

[17] H. Bracht. Self-and foreign-atom diffusion in semiconductor isotope heterostructures. I. continuum theoretical calculations. *Physical Review B*, 75(3):035210, 2007.

[18] R. B. Fair and J. C. C. Tsai. A quantitative model for the diffusion of phosphorus in silicon and the emitter dip effect. *Journal of the Electrochemical Society*, 124(7):1107–1118, 1977.

[19] K. M. Johansen, J. S. Christensen, E. V. Monakhov, A. Yu Kuznetsov, and B. G. Svensson. Deuterium diffusion and trapping in hydrothermally grown single crystalline ZnO. *Applied Physics Letters*, 93(15):152109, 2008.

[20] H. Bracht, H. H. Silvestri, I. D. Sharp, and E. E. Haller. Self-and foreign-atom diffusion in semiconductor isotope heterostructures. II. experimental results for silicon. *Physical Review B*, 75(3):035211, 2007.

[21] K. M. Johansen, L. Vines, T. S. Bjørheim, R. Schifano, and B. G. Svensson. A]luminum Migration and Intrinsic Defect Interaction in Single-Crystal Zinc Oxide. *Phys. Rev. Applied*, 3:024003, Feb 2015.

[22] Z. Guo, A. Verma, X. Wu, F. Sun, A. Hickman, T. Masui, A. Kuramata, M. Higashiwaki, D. Jena, and T. Luo. Anisotropic thermal conductivity in single crystal β-gallium oxide. *Applied Physics Letters*, 106(11):111909, 2015.

[23] C. Sturm, R. Schmidt-Grund, C. Kranert, J. Furthmüller, F. Bechstedt, and M. Grundmann. Dipole analysis of the dielectric function of color dispersive materials: Application to monoclinic Ga_2O_3. *Physical Review B*, 94(3):035148, 2016.

[24] S. Geller. Crystal structure of β-Ga_2O_3. *The Journal of Chemical Physics*, 33(3):676–684, 1960.

[25] T. Zacherle, P. C. Schmidt, and M. Martin. Ab initio calculations on the defect structure of β-Ga_2O_3. *Physical Review B*, 87(23):235206, 2013.

[26] A. Kyrtsos, M. Matsubara, and E. Bellotti. Migration mechanisms and diffusion barriers of vacancies in Ga_2O_3. *Physical Review B*, 95(24):245202, 2017.

[27] K. Irmscher, Z. Galazka, M. Pietsch, R. Uecker, and R. Fornari. Electrical properties of β-Ga_2O_3 single crystals grown by the Czochralski method. *Journal of Applied Physics*, 110(6):063720, 2011.

[28] E. G. Víllora, K. Shimamura, Y. Yoshikawa, K. Aoki, and N. Ichinose. Large-size β-Ga_2O_3 single crystals and wafers. *Journal of Crystal Growth*, 270(3-4):420–426, 2004.

[29] J. B. Varley, H. Peelaers, A. Janotti, and C. G. Van de Walle. Hydrogenated cation vacancies in semiconducting oxides. *Journal of Physics: Condensed Matter*, 23(33):334212, 2011.

[30] S. Ahn, F. R., E. Patrick, M. E. Law, S. J. Pearton, and A. Kuramata. Deuterium incorporation and diffusivity in plasma-exposed bulk Ga_2O_3. *Applied Physics Letters*, 109(24):242108, 2016.

[31] P. Weiser, M. Stavola, W. B. Fowler, Y. Qin, and S. Pearton. Structure and vibrational properties of the dominant oh center in β-Ga_2O_3. *Applied Physics Letters*, 112(23):232104, 2018.

[32] S.A. Campbell. *Fabrication Engineering at the Micro- and Nanoscale*. Oxford Series in Electrical an. Oxford University Press, 2013.

[33] G.J. Phelps. Dopant ion implantation simulations in 4H-Silicon Carbide. *Modelling and Simulation in Materials Science and Engineering*, 12(6):1139, 2004.

[34] J. F. Ziegler and J. P. Biersack. SRIM-2013 software package. *see http://www.srim.org*, 2013.

[35] T. N. Sky. Nickel Diffusion and Configuration in Crystalline Zinc Oxide. Master's thesis, University of Oslo, 2014.

[36] P. Van der Heide. *Secondary ion mass spectrometry: an introduction to principles and practices*. John Wiley & Sons, 2014.

[37] P. Sigmund. Theory of sputtering. I. sputtering yield of amorphous and polycrystalline targets. *Physical review*, 184(2):383, 1969.

[38] P. M. Weiser. *Studies of Hydrogen Defects and Free-Carrier Absorption in Transparent Conducting Oxides using Fourier Transform Infrared Spectroscopy*. PhD thesis, Lehigh University, 2017.

[39] C. Persson. Brief introduction to the density functional theory. *Lecture notes*, 2013.

[40] D. S. Sholl and J. A. Steckel. Density Functional Theory: A Practical Introduction. A John Wiley & Sons. *Inc., Publication*, 2009.

[41] P. Hohenberg and W. Kohn. Inhomogeneous electron gas. *Physical review*, 136(3B):B864, 1964.

[42] W. Kohn and Lu Jeu Sham. Self-consistent equations including exchange and correlation effects. *Physical review*, 140(4A):A1133, 1965.

[43] P. E. Blöchl. Projector augmented-wave method. *Physical review B*, 50(24):17953, 1994.

[44] G. Kresse and D. Joubert. From ultrasoft pseudopotentials to the projector augmented-wave method. *Physical Review B*, 59(3):1758, 1999.

[45] M. Born and R. Oppenheimer. Zur quantentheorie der molekeln. *Annalen der physik*, 389(20):457–484, 1927.

[46] J. P. Perdew, K. Burke, and M. Ernzerhof. Generalized gradient approximation made simple. *Physical review letters*, 77(18):3865, 1996.

[47] J. P. Perdew, A. Ruzsinszky, G. I. Csonka, O. A. Vydrov, G. E. Scuseria, L. A. Constantin, X. Zhou, and K. Burke. Restoring the density-gradient expansion for exchange in solids and surfaces. *Physical review letters*, 100(13):136406, 2008.

[48] J. Heyd and G. E. Scuseria. Efficient hybrid density functional calculations in solids: Assessment of the heyd–scuseria–ernzerhof screened coulomb hybrid functional. *The Journal of chemical physics*, 121(3):1187–1192, 2004.

[49] C. G. Van de Walle and J. Neugebauer. First-principles calculations for defects and impurities: Applications to iii-nitrides. *Journal of applied physics*, 95(8):3851–3879, 2004.

[50] C. Freysoldt, J. Neugebauer, and C. G. Van de Walle. Fully ab initio finite-size corrections for charged-defect supercell calculations. *Physical review letters*, 102(1):016402, 2009.

[51] C. Freysoldt, J. Neugebauer, and C. G. Van de Walle. Electrostatic interactions between charged defects in supercells. *physica status solidi (b)*, 248(5):1067–1076, 2011.

[52] G. Mills and H. Jónsson. Quantum and thermal effects in H_2 dissociative adsorption: Evaluation of free energy barriers in multidimensional quantum systems. *Physical review letters*, 72(7):1124, 1994.

[53] G. Mills, H. Jónsson, and G. K. Schenter. Reversible work transition state theory: application to dissociative adsorption of hydrogen. *Surface Science*, 324(2-3):305–337, 1995.

[54] G. Henkelman, B. P. Uberuaga, and H. Jónsson. A climbing image nudged elastic band method for finding saddle points and minimum energy paths. *The Journal of chemical physics*, 113(22):9901–9904, 2000.

[55] H. J. Monkhorst and J. D. Pack. Special points for brillouin-zone integrations. *Physical review B*, 13(12):5188, 1976.

[56] FlexPDE. Solutions inc. *see http://www.pdesolutions.com*, 2015.

[57] T. R. Waite. Bimolecular reaction rates in solids and liquids. *The Journal of Chemical Physics*, 32(1):21–23, 1960.

[58] P. Erhart and K. Albe. Diffusion of zinc vacancies and interstitials in zinc oxide. *Applied physics letters*, 88(20):201918, 2006.

[59] H.-P. Komsa, T. T. Rantala, and A. Pasquarello. Finite-size supercell correction schemes for charged defect calculations. *Physical Review B*, 86(4):045112, 2012.

[60] Y. K. Frodason. *Unpublished*, 2019.

Appendices

Appendix A

Uncertainties

Table A.1: The minimum and maxium of the diffusivity and dissociation rate giving error bars. The error bar for the dissociation rate was extracted by first fixing the diffusivity and then finding the minimum and maximum dissociation rate with flexPDE simulations which still gave a reasonable fit for the experimental diffusion profiles. Afterwards the opposite was done to find the error bar of the diffusivity.

Sample	Temperature	Diffusivity [cm^2s^{-1}]		Dissociation rate [s^{-1}]	
		Minimum	Maximum	Minimum	Maximum
B2_2	325	2.4e-10	3.2e-10	0.85e0	1.5e0
	335	5.1e-10	6.1e-10	1.7e0	2.3e0
	345	0.95e9	1.15e9	1.68e0	2.1e0
	355	1.6e-9	1.85e-9	1.6e0	1.9e0
B1	500	1.03e-10	1.26e-10	8.32e-4	3.66e-3
	550	5.35e-10	5.80e-10	9.84e-3	1.62e-2
	600	4.07e-9	4.37e-9	1.38e-1	1.83e-1
C1	500	1.43e-10	1.56e-10	1.20e-3	4.50e-3
	525	3.24e-10	3.78e-10	6.30e-3	1.16e-2
(short)	550	5.27e-10	6.62e-10	9.05e-3	3.08e-2
(long)	550	5.83e-10	6.57e-10	7.90e-3	2.69e-2
(long 2)	550	6.21e-10	7.15e-10	1.44e-2	2.37e-2

Table A.2: The maximum and minimum activation energy within the error bars of the values. These values were found from the error bar values listed in Table A.1. A line was drawn within the error bars in the respective plots to find the maximum and minimum activation energies within the error bars. The accompanying prefactor are also listed. Some values could not be found due to small error bars or non-linear plots.

	B2_2				B1				C1			
	E_m	D_0	E_d	ν_0	E_m	D_0	E_d	ν_0	E_m	D_0	E_d	ν_0
max	2.12	1.81e8	-	-	-	-	3.14	2.36e17	1.77	4.60e1	3.66	8.4e20
min	1.74	1.38e5	-	-	-	-	2.65	2.59e14	1.52	1.18e0	0.74	3.1e2

Appendix B

Experimental plots compared with diffusion models

Diffusion length

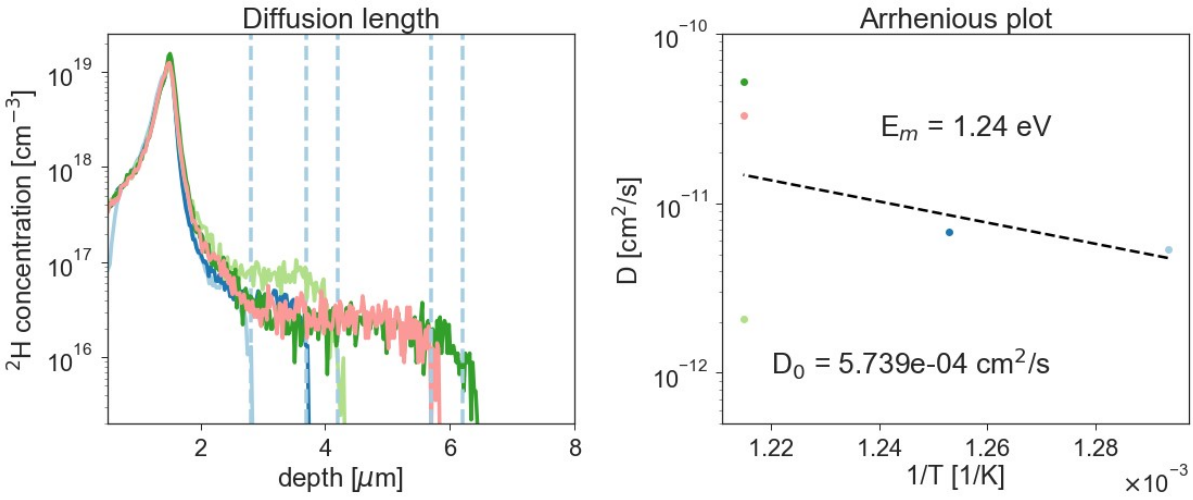

Figure B.0.1: The diffusion length (Equation 4.1) was used to get a preliminary number for the diffusion.

Complementary error function

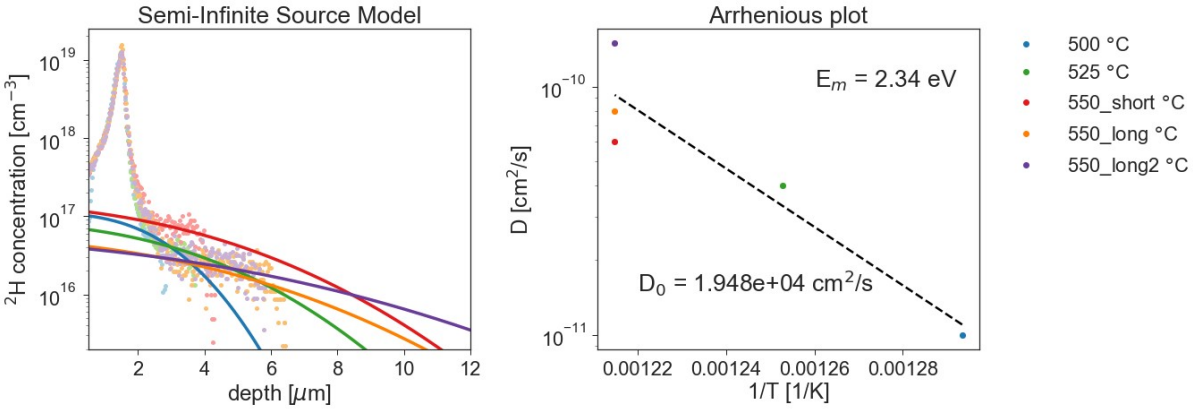

Figure B.0.2: Here is the SIMS data compared with the analytical solution of the diffusion equation called the complementary error function.

Trap Limited Diffusion

C1 Figure B.0.3 shows the experimental data simulated using the trap limited diffusion model.

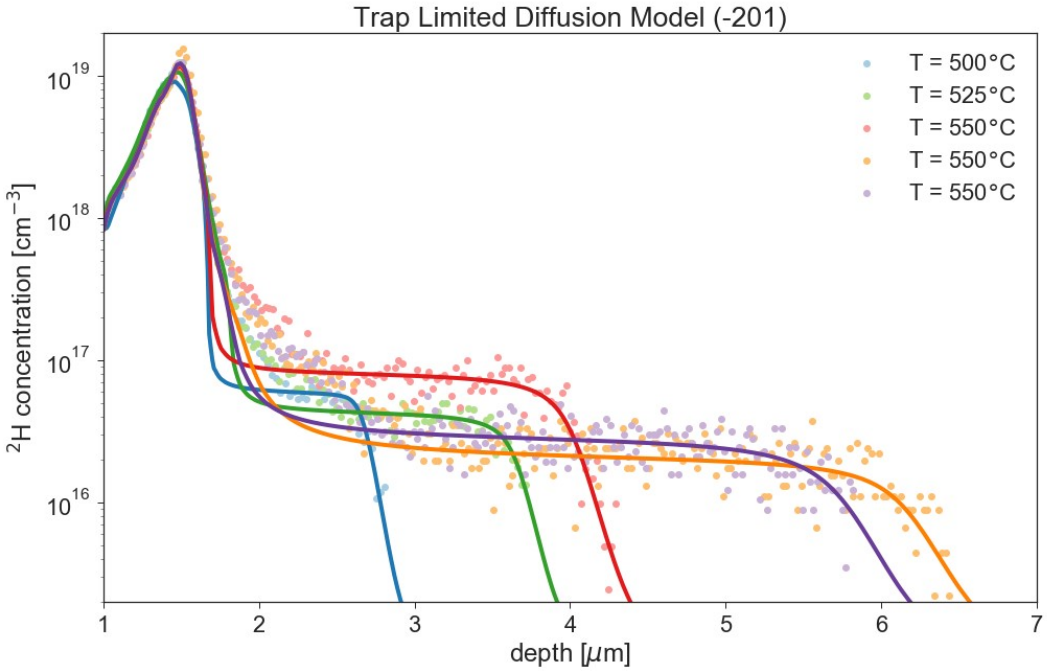

Figure B.0.3: The SIMS data from the second doped (-201) sample compared with the trap limited diffusion model.

B.0.1 (010) oriented sample

Diffusion length

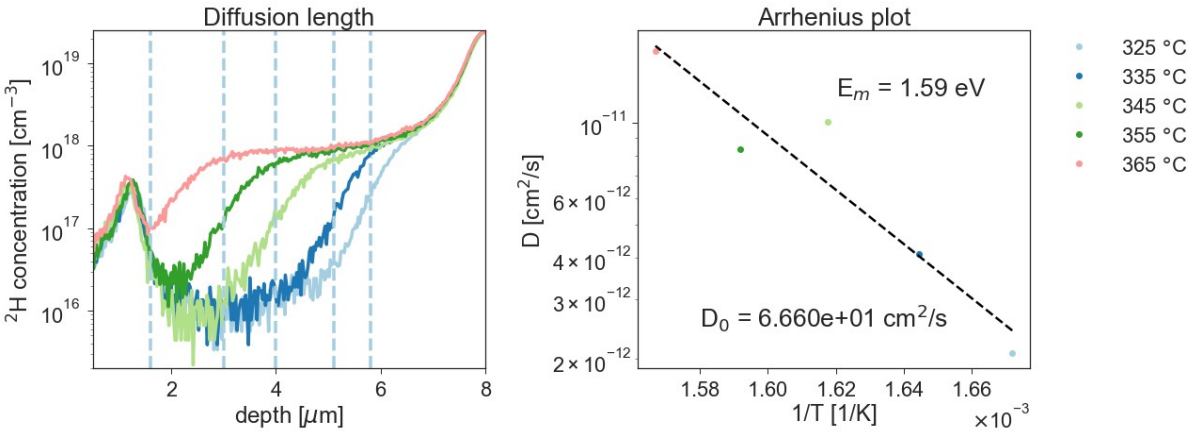

Figure B.0.4: The diffusion length (Equation 4.1) was used to get a preliminary number for the diffusion.

Complementary error function

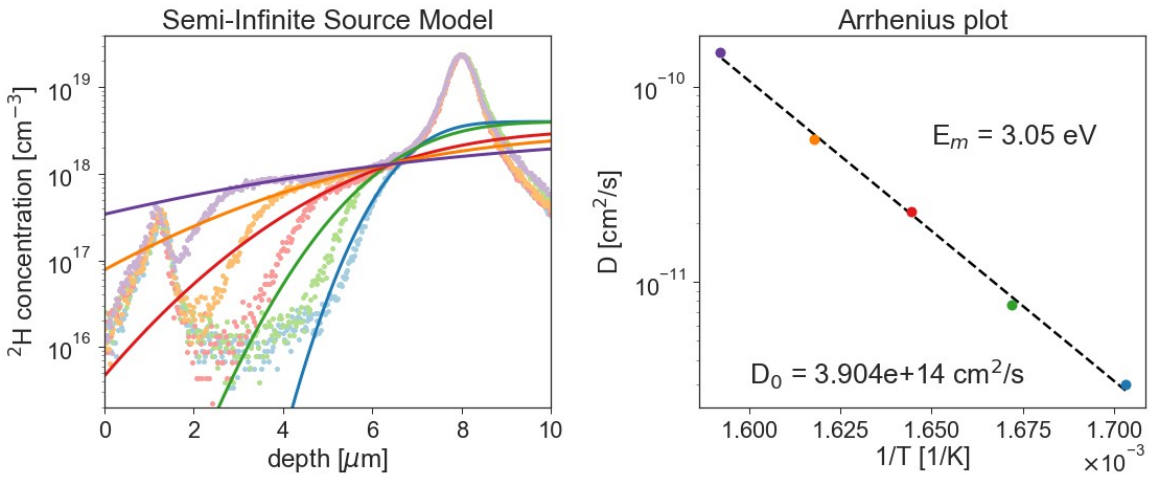

Figure B.0.5: Here is the SIMS data compared with the analytical solution of the diffusion equation called the complementary error function.

Appendix C

Results from other measurements

C.1 Sample orientation

Figure C.1.1: The XRD specrum of some samples performed to confirm their orientation.

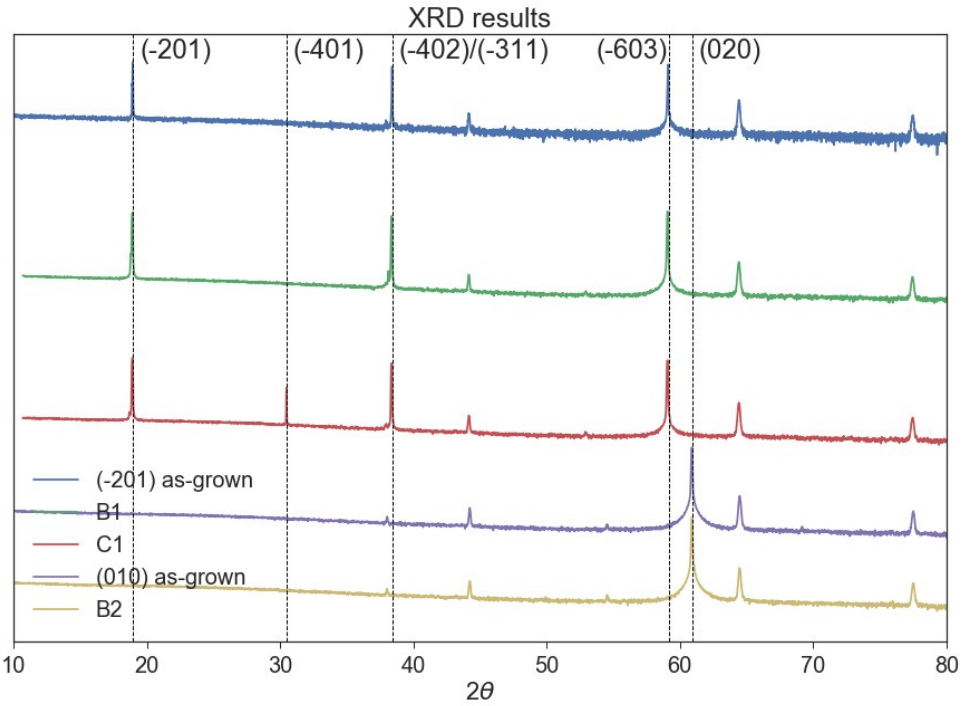

C.2 Mass spectrum

Since there are a lateral difference in the profiles' depth, a reasonable solution is that there is difference in the trap concentration laterally on the sample. Therefore a mass spectre was done in the area of the shorter profiles and in the area of the longer profiles. These mass spectra were measured with SIMS using both the cesium source and the oxygen source. The oxygen source give a higher signal for the common impurities in semiconductors. The result is in Figure C.2.1. There are some differences

in the peak heights, but none very obvious.

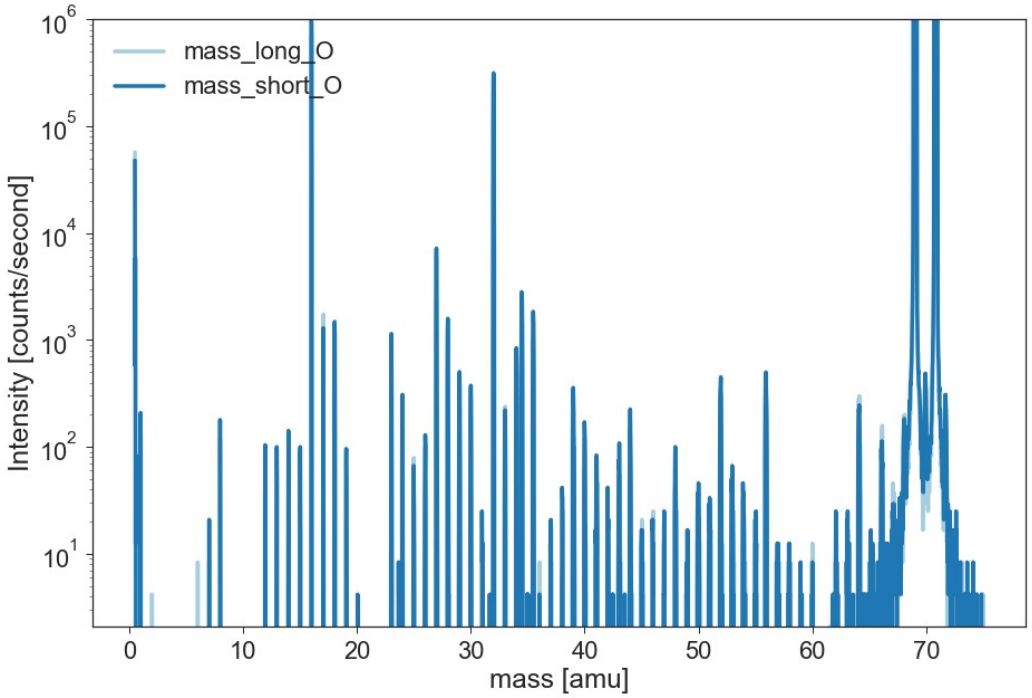

Figure C.2.1: This is the mass spectra of the doped (-201) sample (C1) showing lateral differences in diffusion depth at both 550 °Cand 575 °C. The figure compares the result from the area with the longer profiles and the area of the shorter profiles.

Appendix D

Issues related to depth profiling

The quality of the SIMS measurements are greatly affected by the quality of the primary beam. A non-ideal primary beam will affect the rastered crater and consequently the depth profiles made form the measurements. In this section issues that arose during the investigation and are important for depth profiling is addressed.

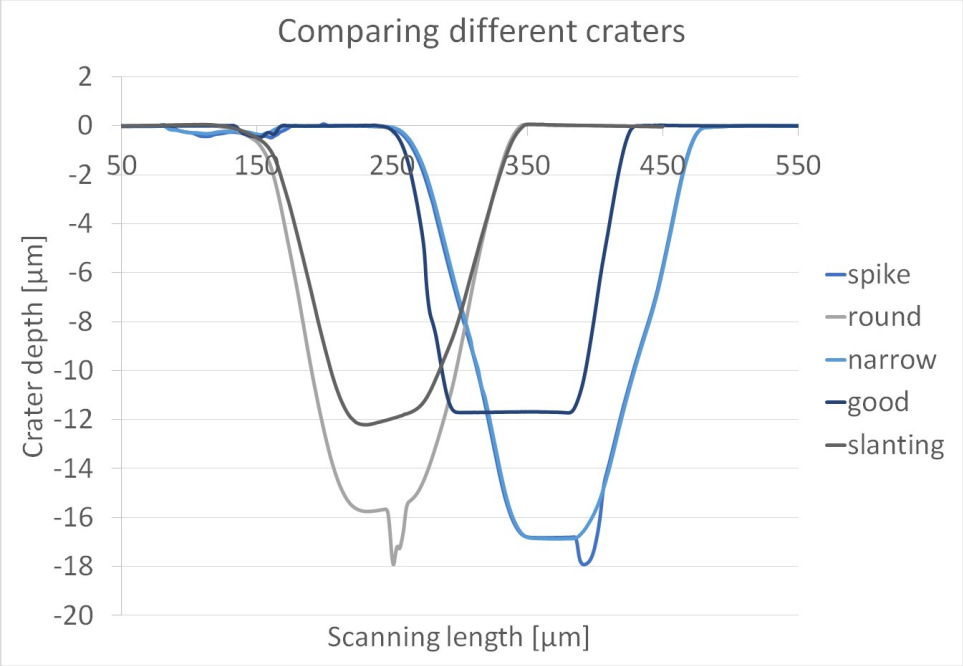

Figure D.0.1: Examples of crater profiles from SIMS measurements.

The ideal crater is a crater with a flat crater surface and steep walls where the secondary ions are only coming from the bottom of the crater. In reality there will be a fraction of the signal that come from the crater edge. This will decrease the depth resolution. The fraction is decreased by only analysing the ions from a part of the rastered area, the analysed area. This analysed area is determined by the field aperture and is typically not be bigger than 33 % of the crater. When one is measuring consentrations close to the detection limit, one would want the highest intensity possible, and then also the largest analysed area possible without getting a too large crater edge affect. The analysed area in SIMS measurements with the specifications used in the measurements in this work

is 63 μm^2. All of the craters from the measurements in this work had the curved walls as shown in Figure D.0.1, but they all had a flat area in the bottom with an area of 1000-2000 μm^2 indicating that the analysed ions are mostly unaffected by this.

A beam that is not aligned well, will easily show on the crater made by the sputtering. Figure D.0.1 compares several crater depth measurements made by the stylus profiler. Some of the craters have a spike at the bottom and others are not strait. The crater depths of this work varied with around 0.03 μm = 30 nm. This do not affect the diffusion simulations in a considerable way.

It is important to have a well aligned beam because a big or unsymmetrical beam spot will influence the crater shape. A good crater shape assures that the secondary ions counted at time t comes from the bottom of the crater, and it makes the conversion to concentration versus depth possible. Figure D.0.2 compares the result with a worse quality beam and a better quality beam. In the upper profile, the diffusion shoulder is greatly affected by the beam difference. This illustrates the importance of a well aligned beam. The unfocused beam results in a broader and more symmetrical peak. It also shows that the depth profile, in combination with the crater measurements shown in Figure D.0.1, easily expose a primary beam of too bad quality, because of the broadening of the peak and the irregularity of the crater.

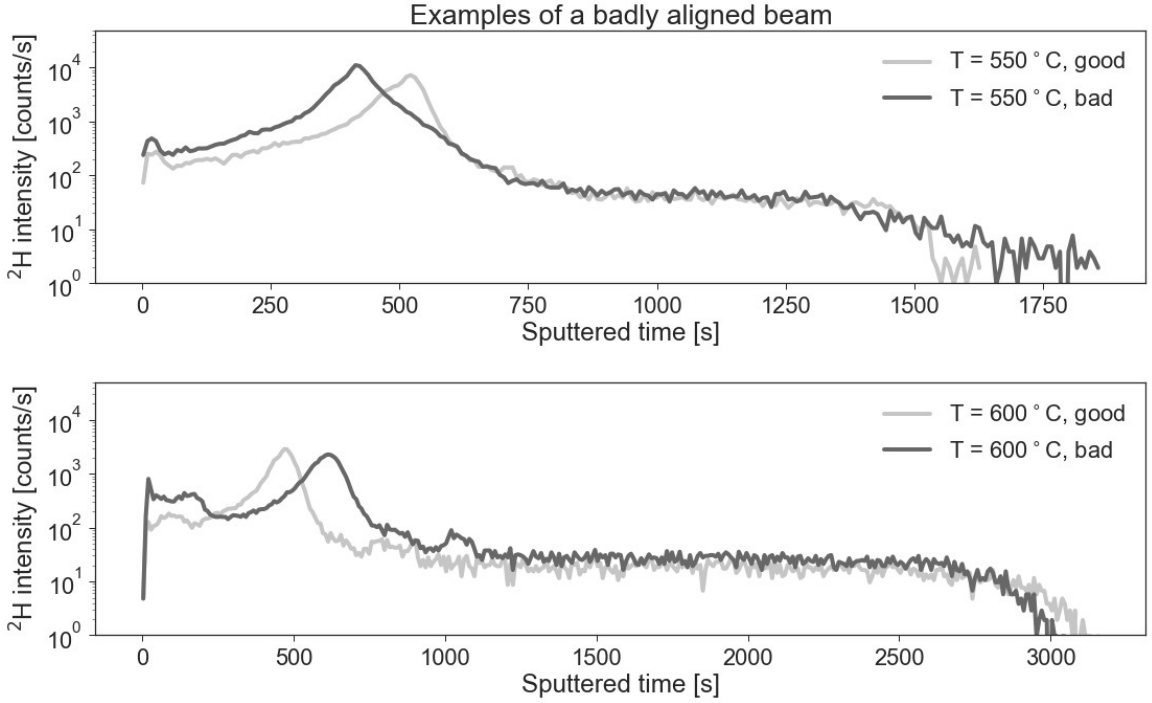

Figure D.0.2: Two examples of a badly aligned beam. A comparison of depth profiles measured in the same sample after an anneal at the same temperature. The unfocused beam make the peak broader and in the upper example the diffusion shoulder is also affected. The slope of the shoulder is steeper in the well aligned beam.

As mentioned earlier, ion implantation creates defects, both extrinsic and intrinsic, and the sputter rate of the implantation peak area might therefore be different than the rest of the substrate. A

comparison of the sputter rate of the peak alone and the sputter rate of the whole profile is listed in Table D.1. There is no big difference between the two, consequently the conversion from time to depth can be trusted.

Table D.1: Comparing the sputtering rate of the peak and the rest of the profile. Checking if the implantation is affecting the sputter rate in the implanted region.

Temp [°C]	Sputtering rate [nm/min]	
	Only peak:	Whole profile:
300	206.3	207.5
500	205.4	204.0
525	205.2	206.0
550 (short)	-	173.2
550 (long)	-	167.2
550 (long)	-	168.5
575 (short)	152.0/153.8	149.3
575 (long)	-	151.1

Appendix E

Convergence tests of lattice parameters for DFT calculations

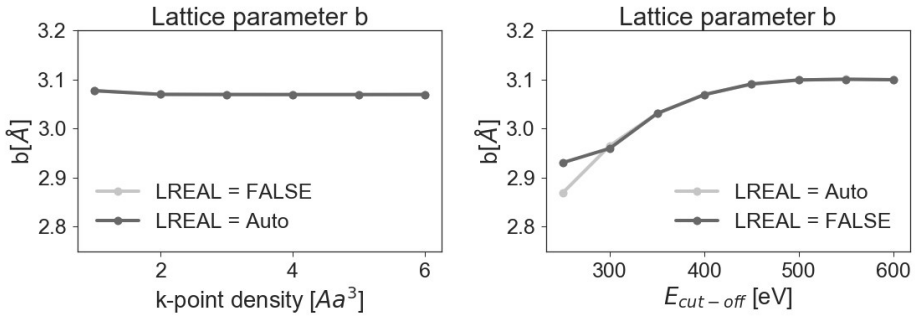

Figure E.0.1: Convergence tests for the lattice parameter c. All calculations were done with both LREAL=Auto and LREAL=FALSE.

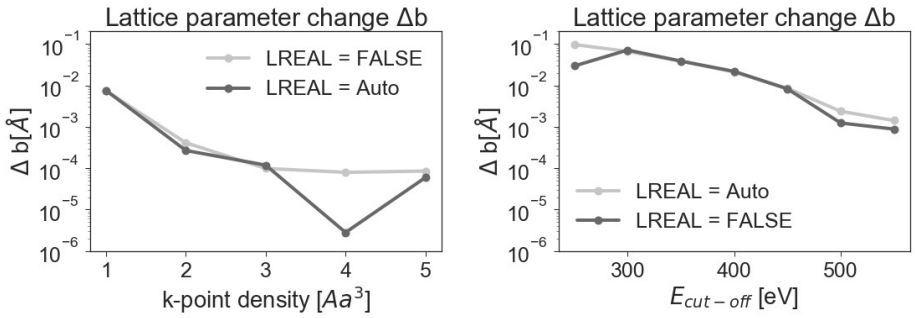

Figure E.0.2: Chance in a with either k-point density or $E_{cut-off}$. All calculations were done with both LREAL=Auto and LREAL=FALSE.

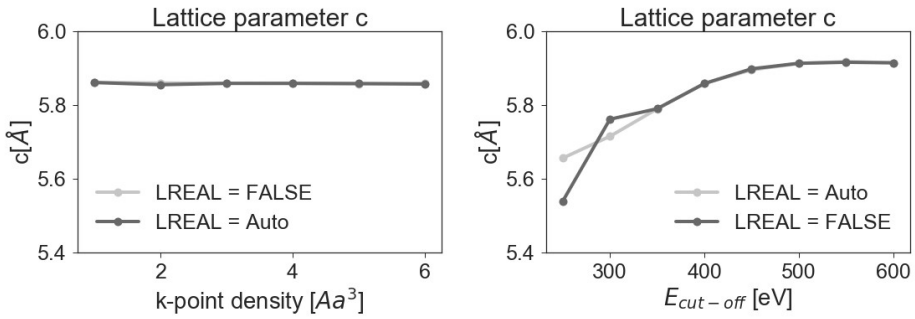

Figure E.0.3: Convergence tests for the lattice parameter c. All calculations were done with both LREAL=Auto and LREAL=FALSE.

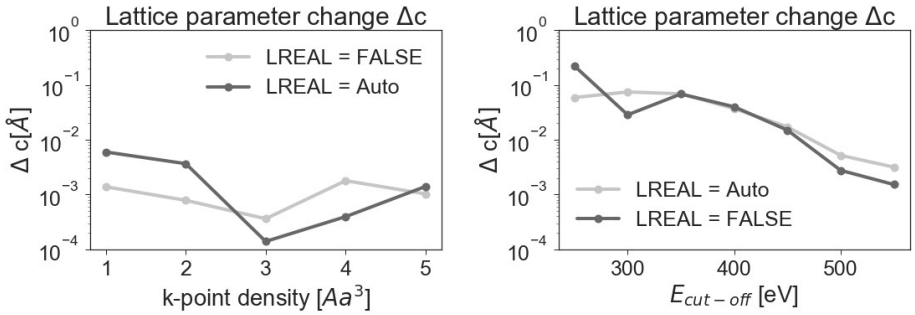

Figure E.0.4: Chance in a with either k-point density or $E_{cut-off}$. All calculations were done with both LREAL=Auto and LREAL=FALSE.

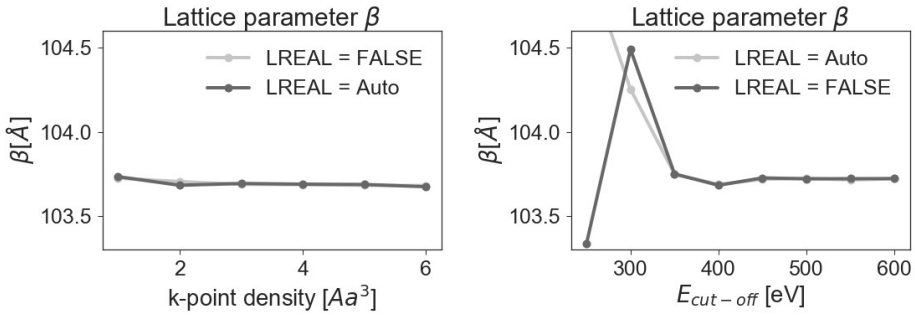

Figure E.0.5: Convergence tests for the lattice parameter c. All calculations were done with both LREAL=Auto and LREAL=FALSE.

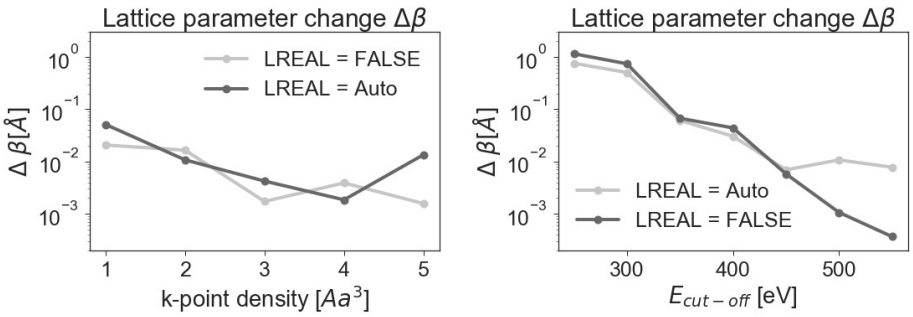

Figure E.0.6: Chance in a with either k-point density or $E_{cut-off}$. All calculations were done with both LREAL=Auto and LREAL=FALSE.

Appendix F

flexPDE scripts

```
TITLE
    '2H TLDiffusion 500-525'        { the problem identification }
COORDINATES
    cartesian1                      { coordinate system, 1D,2D,3D, etc }

VARIABLES                           { system variables }
    C (THRESHOLD = 1e10)            { 2H not in trap }
    trap (THRESHOLD = 1e10)         { empty traps }
    C_t (THRESHOLD = 1e10)          { 2H in trap }
    C_tot (THRESHOLD = 1e10)

SELECT                              { method controls }

DEFINITIONS                         { parameter definitions }

    kT = 8.6173303e-5*(550+273.15)

    Ed = 2.61
    v0 = 1.727e14

    Em = 1.47
    D0 = 5.856e-1

    v = v0*exp(-Ed/kT)
    Di  = D0*exp(-Em/kT)        { diffusivity, cm^2 }


    L   = 6.5e-4                    { Depth, cm }
    tmax    = 60*20                 { Time in furnace, s }
    tstep   =   0.1                 { Size of timesteps }
    C_surf  = 8e17                  { Surface Concentration, cm^-3 }

    R = 5e-8                        { capture radius, cm}
    K = pi*4*R*Di
    tot =    8.3e16
    SS = 1.5e15
    C_SS = C*SS/(C+SS)
```

```
    experimental = TABLE ("../2H_D2_C1/FlexPDE_550_short_no_left.txt"  )
    prev= SMOOTH(2e-6) TABLE("../2H_D2_C1/FlexPDE_525_no_left.txt")

INITIAL VALUES

    C_t=        1e13
    C=      prev


EQUATIONS                       { PDE's, one for each variable }

    C:      dt(C) = Di*dxx(C_SS) -dt(C_t)

    trap:   trap=tot-C_t

    C_t:    dt(C_t)=K*(C_SS)*trap-v*C_t

    C_tot:  C_tot = C + C_t

BOUNDARIES                  { The domain definition }
    REGION 1 'Low'              { For each material region }
        start(1e-4)
        point value(C)= C_surf
        line to (L)
        point value(C_tot) = 1e15



TIME 0 to (tmax) by (tstep)

MONITORS        { show progress }
    for t = 0 by tstep to tmax

    elevation((C_t+C),asimp,experimental) log from (1e-4) to (L)
    as "Trap concentration" fixed range (1e15, 3e19)

END
```